

Partial-Contact Head Disk Interface for Ultrahigh Density Magnetic Recording

By

Du Chen

B. S. (University of Science and Technology of China) 2002

M. S. (University of California, Berkeley) 2007

A dissertation submitted in partial satisfaction of the

requirements for the degree of

Doctor of Philosophy

in

Engineering - Mechanical Engineering

in the

Graduate Division

of the

University of California, Berkeley

Committee in charge:

Professor David B. Bogy, Chair

Professor Tarek I. Zohdi

Professor David Brillinger

Fall 2008

The dissertation of Du Chen is approved:

Chair

Date

Date

Date

University of California, Berkeley

Summer 2008

Partial-Contact Head Disk Interface for Ultrahigh Density Magnetic Recording

© 2008

By

Du Chen

Abstract

Partial-Contact Head Disk Interface for Ultrahigh Density Magnetic Recording

by

Du Chen

Doctor of Philosophy in Engineering- Mechanical Engineering

University of California, Berkeley

Professor David B. Bogy, Chair

One of the major technological challenges for achieving an ultrahigh areal recording density of 1~10Tbit/in² is to obtain a reliable and robust head disk interface with a flying height less than 2.5 nm. This results in a transducer clearance of less than 1 nm even on a smooth disk surface with a glide height of only 1.5 nm. It is also required that the amplitude of the flying height variation should be less than 10% of the clearance in order to maintain a stable read/write process. With such a low clearance, the impact and contact between the slider and disk become unavoidable, resulting in a large likelihood of the slider's bouncing and the head's wearing. The bouncing and wearing may cause instability of the head disk interface and the dysfunction of the read/write transducer. All of these challenge the design of the next generation air bearing sliders.

This dissertation proposes and analyzes a partial-contact recording system with an air bearing to obtain the ultra-low but stable head disk spacing for 1~10 Tbit/in². The

research reported here focuses on the numerical simulation of the slider's performance in a partial-contact head disk interface and the feasibility of maintaining both a low bouncing amplitude and a low contact force. The effects of different factors important to the performance of the interface are numerically analyzed.

First, existing models of slider-disk contact and adhesion are analyzed and improved for the numerical simulation of the partial-contact slider. Two types of quasi-static contact models- the asperity-based contact model and the elastic contact model based on the influence coefficient- are compared and implemented for different slider-disk interaction situations. The intermolecular adhesion models are improved for the slider-disk adhesion in the near-contact or contact regime. Second, a nonlinear dynamics model of the partial-contact slider with air bearing is proposed. Numerical simulations with this model are carried out to investigate the performance of a partial-contact slider and to study the effects of different factors. Based on this dynamics model, a six-degree-of-freedom slider model is employed to analyze the in-plane vibrations of the slider as well as the bouncing in the near-contact and contact regimes. Third, a different explanation of the slider's bouncing vibration is presented based on numerical simulations using three slider dynamics models. Forth, a novel partial-contact head disk interface with thermal protrusion is proposed, which is stimulated by the widely used thermal flying control or dynamic flying height technology. The heat transfer at the air bearing surface is numerically studied. Different head disk interface heat transfer models are examined and compared. The performance of the partial-contact slider with thermal protrusion is

simulated and compared with a micro-trailing pad slider. It is found that the bouncing vibration amplitude can be reduced to become comparable to the flying height modulation, when the disk track is burnished or the air bearing pressure peak is enforced at the trailing edge center.

The key contributions of this dissertation are the identification of the causes and influential factors of some mechanical challenges inherent in ultrahigh density magnetic recording required for the next generation of hard disk drives, as well as simulation-based solutions to address these challenges.

Professor David B. Bogy

Dissertation Chair

Dedication

To my wife

TABLE OF CONTENTS

Dedication.....	i
Table of Contents	ii
List of Figures.....	viii
List of Tables.....	xv
Acknowledgements.....	xvii
Chapter 1 Introduction	1
1.1 Hard Disk Drive, Head Disk Interface, Head Media Spacing, Flying height and Air Bearing Surface	1
1.2 Research Motivation and Objectives.....	3
1.3 Dissertation Organization.....	4
References	5
Chapter 2 Contact Models for the Slider-Disk Contact and Impact	8
2.1 Introduction.....	8
2.2 Slider-Disk Quasi-Static Impact	10
2.3 Decoupled Normal Pressure and Tangential Friction	11
2.4 Asperity-based Contact Models.....	11
2.4.1 Single Asperity Contact and Contact Models	13

2.4.2	Surface Roughness Parameters	15
2.4.3	A Proper Model for Slider-Disk Asperity Contact.....	16
2.4.4	Numerical Implementation of the GW Model and the KE Model.....	20
2.4.5	Asperity Contact Models with Assumptions 4 and 5 Relaxed.....	23
2.5	Contact Model Based on Influence Coefficients	24
2.5.1	Influence Coefficient and Corresponding Contact Model	24
2.5.2	Application to Slider-Disk Contact.....	25
2.5.3	Numerical Schemes for Solving the Obtained Linear System.....	28
2.5.4	Computation Time for the CG Method and the GPCG Method	35
2.5.5	Comparison of the Contact Model Based on Influence Coefficients and the Multi-asperity Contact Model by Cha	35
2.6	Conclusions.....	36
	References	37
 Chapter 3 Intermolecular Adhesion between an Air Bearing Slider in Contact or Near Contact Regime and a Disk.....		
3.1	Introduction.....	50
3.2	Intermolecular Adhesion Force Model	51
3.3	Improved DMT Model for Asperity Adhesion	54
3.4	Net Adhesion Stress	56
3.5	Static Simulation of an Air Bearing Slider	58
3.6	Conclusions.....	60

References	61
Chapter 4 Dynamics of a Partial-Contact Head Disk Interface	68
4.1 Introduction.....	68
4.2 Dynamics, Adhesion and Contact Models	70
4.3 Simulation Results and Discussion.....	72
4.3.1 Disk Roughness and Surface Energy Change.....	73
4.3.2 Friction Coefficient.....	74
4.3.3 Micro-Trailing Pad Width.....	74
4.3.4 Preload	75
4.4 Conclusions.....	75
References	76
Chapter 5 Six-Degree-of-Freedom Vibrations of Partial-Contact Sliders in Hard Disk Drives.....	82
5.1 Introduction.....	82
5.2 Air bearing, Adhesion, Contact and Friction Models for Partial-Contact Sliders 84	
5.3 Six-DOF Slider Dynamic Model	84
5.4 Dynamic Simulations of a Micro Trailing Pad Slider.....	86
5.4.1 Dynamic response to an Initial Excitation	86
5.4.2 Effect of Disk Micro-Waviness and Roughness	88
5.4.3 Effect of Skew Angle	89

5.4.4 Effect of Friction.....	90
5.4.5 Effect of the Micro Trailing Pad Width	90
5.5 Conclusions.....	91
References	92
Chapter 6 Numerical Investigation of Bouncing Vibrations of an Air Bearing Slider in Near or Partial Contact.....	102
6.1 Introduction.....	103
6.2 Dynamics, Adhesion and Contact Models	103
6.3 Three Slider Dynamics Models	105
6.4 Slider Dynamics Simulation and Results.....	106
6.4.1 Dynamic Simulations Using the CML Air Bearing Model, the Elastic Contact Model and the Modified Intermolecular Force Model	106
6.4.2 Dynamic Simulations Using the CML Air Bearing Model and the Multi-Asperity Contact and Meniscus Adhesion Model of Ono and Yamane.....	107
6.4.3 Dynamic Simulations Using Ono and Yamane's 2-DOF Dynamics Model ...	110
6.5 Conclusions.....	114
References	115
Chapter 7 Simulation of Static Flying Attitude with Different Heat Transfer Models for a Flying Height Control Slider with Thermal Protrusion	127
7.1 Introduction.....	127
7.2 Heat transfer models for the head-disk interface	129

7.3	Simulation of air bearing sliders with thermal protrusion	132
7.4	Simulation results for static flying attitudes	133
7.4.1	Pico slider.....	133
7.4.2	Femto slider	136
7.5	Conclusions.....	136
	Reference.....	137
Chapter 8 Partial-Contact Head-Disk Interface with Thermal Protrusion.....		151
8.1	Introduction.....	151
8.2	Partial-contact HDI with thermal protrusion	152
8.3	Dynamic Simulation of a partial-contact slider with thermal protrusion	153
8.4	Simulation results and discussion of partial-contact sliders with thermal protrusion.....	155
8.4.1	FHM and bouncing vibration.....	155
8.4.2	A partial-contact slider with thermal protrusion and a partial-contact micro-trailing-pad slider	156
8.4.3	Friction between the slider and the disk	157
8.4.4	Adhesion between the slider and the disk.....	157
8.4.5	Disk surface	158
8.4.6	ABS designs for a Partial-Contact HDI with Thermal Protrusion	160
8.5	Conclusions.....	162
	References	163

Chapter 9 Summary and Conclusion 178

LIST OF FIGURES

Chapter 1

Fig.1.1. HDD without cover and Sketch of the HDD structure (www.westerndigital.com)

Fig.1.2. Increase of areal recording density in the HDDs (www.hgst.com)

Fig.1.3. Reduction of the physical spacing (flying height) (www.hgst.com)

Fig.1.4. Evolution of the slider and air bearing surface (www.hgst.com)

Chapter 2

Fig.2.1. Density function of Gaussian distributed asperity height u .

Fig.2.2. Contact force versus separation and real contact area ratio versus separation for three cases with GW, CEB (i.e., EP) and KE model with plasticity index ψ equal to 0.836, 0.587 and 0.386, respectively.

Fig.2.3. Contact force and real contact area versus pitch angles for GW and KE model.

Fig.2.4. Two different contact cases that can not be related through Saint-Venant's Principle.

Fig.2.5. Demonstration of two nodes on meshed slider air bearing surface.

Fig.2.6. Time consumption of CG method and GPCG method on a computer with a Intel Pentium Mobile 1.3GHz processor.

Fig.2.7. Two slider-disk contact cases.

Fig.2.8. Algorithms of two numerical schemes for contact analysis with the influent coefficient model.

Chapter 3

Fig.3.1. An infinite half space and a unit surface area of a parallel infinite half space.

Fig.3.2. Adhesion stress obtained through intermolecular force model with and without considering the contact distance ε .

Fig.3.3. Adhesion stresses obtained through the IDMT, CEB-IDMT and KE-IDMT model.

Fig.3.4. Contact pressure obtained through the GW, CEB and KE model.

Fig.3.5. Net adhesion pressure obtained through the GW, CEB and KE contact and adhesion models.

Fig.3.6. Air bearing surface of CML femto slider.

Fig.3.7. Minimum flying height versus disk RPM for the rougher slider/disk surfaces (case 2 in Table 3.1), smoother slider/disk surfaces (case 3 in Table 3.2), flat slider/disk interfaces and the case without considering the slider/disk adhesion or contact (the solid lines represent stable equilibria and the dotted lines represent unstable equilibria).

Chapter 4

Fig.4.1. Air bearing surface design (unit: mm).

Fig.4.2. History of the FH, pitch, roll and contact force and their frequency analyses on the disk surface with RMS 0.6 nm.

Fig.4.3. Slider bouncing 3σ and contact force on disk surfaces with various RMS and $\Delta\gamma$ values.

Fig.4.4. Slider bouncing 3σ and contact force on disk surfaces with various friction coefficients and $\Delta\gamma$ values.

Fig.4.5. Slider bouncing 3σ and contact force of micro trailing pad sliders with various pad widths.

Fig.4.6. Slider bouncing 3σ and contact force of micro trailing pad sliders with various values of preload.

Chapter 5

Fig.5.1. Suspension and slider coordinate systems.

Fig.5.2. Air bearing surface design of femto slider (unit: mm).

Fig.5.3. Dynamic response to an initial excitation of loading the slider from 2 nm onto a flat disk surface.

Fig.5.4. Dynamic response to an initial excitation of loading the slider from 2 nm onto a flat disk surface with zero suspension damping in the simulation.

Fig.5.5. Measured track profile and its power spectrum at the disk velocity 24 m/s

Fig.5.6. Time history of the slider on a smooth disk with RMS 0.2 nm and the corresponding power spectrum.

Fig.5.7. Time history of the slider with a skew angle of 6.65° .

Fig.5.8. Time history of the slider on a smooth disk on a smooth disk with different friction coefficients.

Fig.5.9 Time history of the slider with trailing pad width of 100 μm , 80 μm and 60 μm .

Chapter 6

Table 6.1 Parameter values used in the multi-asperity contact and adhesion model for the slider-disk contact (upper asterisks denote the default values used in the simulations)

Table 6.2 Parameter values used for 2-DOF slider dynamic simulations

Table 6.3 Simulation results of a 4 nm slider and a 3 nm slider with $\zeta_f = \zeta_r = 0.002$ and $d_l = d_s$

Fig.6.1. Air bearing surface design of a micro-trailing pad slider

Fig.6.2. Time histories of the minimum spacing, the pitch, the roll and the power spectra of the minimum spacing of case I (the micro trailing pad slider on the ideally flat disk surface), case II (the micro trailing pad slider on a rough disk surface with moving roughness within the HDI) and case III (the micro trailing pad slider on a rough disk surface with stationary roughness within the HDI)

Fig.6.3. Simplified characteristic model of real contact force, adhesion force and contact force as functions of separation [1]

Fig.6.4. Air bearing surface design of the CML slider used in the CML 2-DOF slider dynamic simulation

Fig.6.5. Time history of the slider dynamics with different maximum meniscus force f_m

Fig.6.6. Time history of the slider dynamics with different take-off FH d_e

Fig.6.7. Time history of the slider dynamics with the different friction coefficient μ

Fig.6.8. Time history of the slider dynamics with different initial FH

Fig.6.9. 2-DOF slider model by Ono and Yamane [1]

Fig.6.10. Time history of the 2-DOF slider model with the parameter values shown in Table 6.2

Fig.6.11. Time history of the 2-DOF slider model with the parameter values shown in Table 6.2 except that $\mu = 2.0$

Fig.6.12. Time history of the 2-DOF slider model with the parameter values shown in Table 6.2 except that $f_m = 50$ mN.

Fig.6.13. Time history of the 2-DOF slider model with the parameter values shown in Table 6.2 except that $d_e = 8$ nm

Fig.6.14. Time history of the 2-DOF slider model with the parameter values shown in Table 6.2 except that $\zeta_f = \zeta_r = 0.002$

Chapter 7

Fig.7.1. Air bearing surface of an INSIC pico slider (unit: mm).

Fig.7.2. Air Bearing Surface of a commercial femto slider (unit: mm).

Fig.7.3. Temperature and heat flux on the ABS at the static state flying attitude with and without considering the viscous heating for a heating power of 40 mW, 80 mW and 120 mW.

Fig.7.4. Static transducer flying height, pitch and roll angles of the slider obtained with Ju's model versus with Zhang's and Chen's models.

Fig.7.5. Temperature and heat conduction flux on the ABS at the static state flying attitude obtained with Zhang's and Chen's models (the viscous dissipation is neglected).

Fig.7.6. Static transducer flying height, pitch and roll angle of the slider obtained with Zhou's model versus Zhang's and Chen's models with the heating power of 40 mW.

Fig.7.7. Static transducer flying height, pitch and roll angle of the slider obtained with Zhou's model versus Zhang's and Chen's models with the heating power of 80 mW.

Fig.7.8. Temperature and heat conduction flux on the ABS at the static state obtained with Zhou's model versus Zhang's and Chen's models (the viscous dissipation is neglected) at the ambient temperature of 70°C.

Chapter 8

Fig.8.1. Air bearing surface of Slider 1 (unit: mm).

Fig.8.2. A smooth track profile and its power spectrum corresponding to a disk linear velocity of 17.34 m/s.

Fig.8.3. Time history of Slider 1 with heating powers of 0 mW, 15 mW, 20 mW to 25mW and the corresponding FH power spectrum.

Fig.8.4. Time histories of a partial-contact slider with thermal protrusion and a partial-contact micro-trailing-pad slider on the smooth track.

Fig.8.5. Time histories of Slider 1 with 25 mW heating power on the smooth disk track with the friction coefficient values of 0.3, 1.0 and 2.0.

Fig.8.6. Time histories of Slider 1 on the smooth track with the change of surface energy before and after slider-disk contact ($\Delta\gamma$) for values of 0.08 J/m², 0.008 J/m² and 0.001 J/m².

Fig.8.7. A rough disk track profile and its power spectrum corresponding to a disk linear velocity of 17.34 m/s.

Fig.8.8. Time histories of Slider 1 with 25 mW heating power on the smooth track and the rough track.

Fig.8.9. Burnished track profiles and their power spectra corresponding to a disk linear velocity of 17.34 m/s.

Fig.8.10. Time histories of Slider 1 on the smooth track (shown in Fig.8.2.) and burnished tracks (shown in Fig.8.9.) and the corresponding power spectra of FH.

Fig.8.11. Air bearing surfaces of Slider 2 and Slider 3 (unit: mm).

Fig.8.12. Air bearing pressure profiles of Slider 1, 2 and 3, respectively, at the static state with heating power off (unit: atm).

Fig.8.13. Air bearing pressure profiles of Slider 1, 2 and 3, respectively, at the static state with the touch-down heating power (unit: atm).

Fig.8.14. Time histories of the slider dynamics on the smooth track for Slider 1, 2 and 3.

LIST OF TABLES

Chapter 2

Table 2.1 Slider and disk roughness and material parameters

Table 2.2 Numerical results for two cases of slider-disk contact shown in Figure 2.7

Chapter 3

Table 3.1 Slider/disk equivalent roughness parameters

Chapter 4

Table 4.1 Slider, disk and suspension specifications

Chapter 5

Table 5.1 Suspension model used in the simulation

Chapter 6

Table 6.1 Parameter values used in the multi-asperity contact and adhesion model for the slider-disk contact (upper asterisks denote the default values used in the simulations)

Table 6.2 Parameter values used for 2-DOF slider dynamic simulations

Table 6.3 Simulation results of a 4 nm slider and a 3 nm slider with $\zeta_f = \zeta_r = 0.002$ and $d_l = d_s$

Chapter 7

Table 7.1 Specification of the suspension used in the numerical analysis and corresponding static flying attitude of the pico slider (shown in Figure 7.1) with heating power off

Table 7.2 Static flying attitudes of the pico slider (shown in Figure 7.1) obtained with and without the viscous heating contributed by the Couette flow

Table 7.3 Air parameters at different temperatures

Table 7.4 Static flying attitudes of the pico slider (shown in Figure 7.1) obtained with Zhou's model and with Zhang's and Chen's models

Table 7.5 Static flying attitudes of the femto slider (shown in Figure 7.8) obtained with different HDI heat transfer models

Chapter 8

Table 8.1 Suspension load and flying attitudes of Slider 1, 2 and 3 with heating power off

ACKNOWLEDGEMENTS

First of all, I would like to express my sincere gratitude to my research advisor, Prof. David B. Bogy, for his guidance and encouragement through my Ph.D. studies. I take this experience as the most unforgettable and invaluable period in my life. Prof. Bogy is a role model in my mind not only for his earnest attitude toward scientific research but also for his generosity and consideration toward people around him. I would also like to thank Prof. Zarek I. Zohdi and Prof. David Brillinger for reviewing this dissertation.

I am grateful to Dr. Jia-Yang Juang for his helpful suggestions and advice when I started this research project. His great Ph. D. research was a real help to me. I also want to thank Dr. C. Singh Bhatia, previously of Hitachi Global Storage Technologies and currently of National University of Singapore, for leading the Tribology group of the INSIC EHDR project and for his encouragement and advice at the CML weekly group meeting.

I would like to thank my colleagues in CML for their friendship and support. In particular, I am thankful to Branden Cox for his big help on the software programming. I also appreciate many useful discussions with Puneet Bhargava, Sean Moseley, Liang Pan, Nan Liu, Sripathi Canchi and etc.

Finally, I am deeply indebted to my parents and elder brother for their love and support. They tried their best to provide me with the best education. Any of my successes is impossible without their great love and encouragement. I also want to deeply thank my

wife, Wei Yu, for her love and support all along.

This research presented in this dissertation was supported by the Computer Mechanics Laboratory (CML) and the Extremely High Density Recordings (EHDR) project of the International Storage Industry Consortium (INSIC).

Chapter 1 Introduction

1.1 Hard Disk Drive, Head Disk Interface, Head Media Spacing, Flying height and Air Bearing Surface

A hard disk drive (HDD), also called a hard drive or hard disk, is a non-volatile data storage device which stores digitally encoded data on a rotating disk coated with magnetic layers. Since the first HDD was introduced in 1957 by IBM, new technologies have been applied in the evolution process of HDDs and a rapid increase in both the areal recording density and data transfer rate have been maintained all along. With the basic operation principles almost unchanged, however, today the HDD is still the main mass storage device for computers and networks due to its advantages in storage capacity, cost per unit storage amount, data access time and storage reliability.

The structure of a HDD is shown in Figure 1.1. Usually the components inside a HDD can be divided into four main parts. They are 1.magnetic read/write heads, magnetic disks and head disk interface (HDI); 2.a printed circuit board with data detection electronics and write circuit; 3.mechanical servo and control system, including spindles, actuators, suspensions and control chips; 4 interface to microprocessor and power supplier. The mechanical operation of the head-disk assembly relies on an air bearing film between the slider and the spinning disk for a stable self regulating head media spacing (HMS). Different data tracks are in the range of read and write of the read/write heads, as the sliders are positioned along the radial direction.

Figure 1.2 shows the rapid increase of areal recording density of HDDs. The

innovation of read/write transducers, the increase of the servo system's position accuracy and especially the reduction of the HMS directly lead to the increase of recording density while keeping the signal to noise ratio obtained from the read head within an acceptable range. The HMS includes the thickness of the protective layers- slider and disk diamond-like-carbon (DLC) overcoats and disk lubricant- and the physical spacing between the read/write transducer and the disk (flying height). The protective layers must have certain minimum thicknesses for their performance, so the reduction of the flying height (FH) is necessary. Figure 1.3 shows a continuous reduction of FH over the years. A reduced but still stable flying height of a slider mainly relies on a delicate design of the slider's patterned surface opposite to the disk surface. This patterned surface is called the air bearing surface (ABS). The relative motion between the slider with a well designed ABS and the disk creates an air pressure field that can stably sustain the slider's FH. The evolution of the slider and ABS is shown in Figure 1.4.

As the result of the rapid development of the hard disk drive, magnetic recording densities between 1~10 Tbit/in² have become the new targets of the Information Storage Industry Consortium (INSIC), a HDD organization in the US. The HMS and FH are required to be lower and lower for the higher and higher recording densities. The HMS for the 1 Tbit/in² is designed to 5 nm. At most this can include a FH of 2.5 nm. Even if all of the protective layers can be reduced to 2.5 nm, it is quite challenging that the roughness (glide height) can be less than 1.5 nm. Therefore we are talking about no more than 1.0 nm clearance in the HDI for 1 Tbit/in². The HMS for the 10 Tbit/in² is designed to be 2 nm and the corresponding FH is 1 nm when the total thickness of protective layers is reduced to 1 nm. Even if the roughness of the disk can be reduced to 0.75 nm, there will be no more than 0.25 nm transducer clearance within the HDI for the 10Tbit/in².

1.2 Research Motivation and Objectives

“Contact” is unavoidable for the final solution to reducing the transducer clearance below 1 nm. With the pitch and roll angles and disk morphology considered, the transducer clearance may not be the smallest gap between the slider and disk. The slider may still have some part of its geometry in contact with a smooth enough disk. It is well known that bouncing vibration and flying hysteresis tend to increase with a decrease in roughness height, due to the increased van der Waals forces and electrostatic force in the HDI, as well as the contact force between the slider and disk. The contact induced in-plane vibration of the slider may decrease the track following ability and increase the read/write bit error. All of these factors will challenge the requirement that the clearance variation should be no larger than 10% of the transducer clearance.

Conventionally there are several interface designs under consideration for high recording densities: “wear in”, “proximity”, “partial contact”, and “full contact”. It is expected that all of these technologies, except possibly the last one, will rely on an air bearing film to support most of the suspension load. Additionally, thermal flying height control or dynamic flying height control is widely used in current hard drives to locally lower the slider’s flying height. This advantageous technique makes use of a localized thermal protrusion at the read/write transducer, which is adjusted by the embedded micro-heater at the trailing edge center. Based on this technology, a contact HDI with thermal protrusion is proposed. This new partial-contact HDI has only a small protruded tip in contact with the disk surface, which has a small radius of curvature, while other parts of the air bearing surface (ABS) are almost unchanged and remain sufficiently far away from the disk to avoid contact.

The research addressed in this dissertation numerically analyzes the feasibility and influential factors of contact recording, especially partial-contact recording with air bearing, to achieve a stable transducer FH well below 3 nm for a recording density of 1 Tbit/in² or even greater. Models for slider disk contact, adhesion and friction are analyzed and adjusted to approximate the slider disk interaction. Factors within the HDI, which affect the slider's bouncing vibration and the slider's in-plane vibration due to the slider-disk contact, are numerically studied. For the new HDI with thermal protrusion, different HDI heat transfer models for the numerical calculation of FH reduction are analyzed and compared. Finally ABS designs for a partial-contact HDI with thermal protrusion are proposed and analyzed.

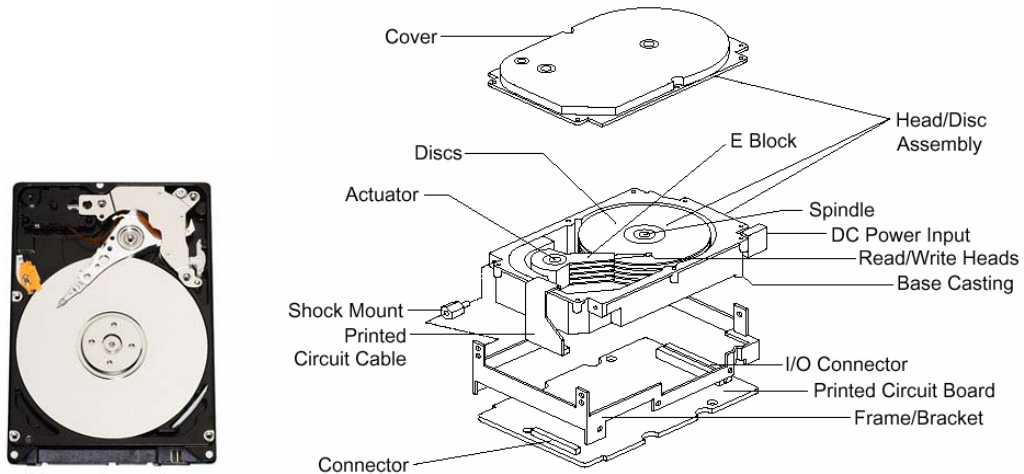
1.3 Dissertation Organization

This dissertation is organized into nine chapters. Chapter 1, i.e. the current chapter, is an introduction of the history and structure of HDD, the HDI, HMS, FH and ABS, the research objectives and dissertation organization. Chapter 2 is focused on the analysis of two types of contact models for the slider-disk impact, i.e. the asperity contact model and the elastic contact model based on influence coefficients. Chapter 3 develops a modified intermolecular adhesion force model for the slider-disk adhesion. The effect of adhesion and contact on an air bearing slider in the contact or near contact regime is analyzed. Chapter 4 presents the numerical analysis of a conventionally designed partial-contact HDI. Factors within the HDI that affect the bouncing and contact of the slider are studied. Chapter 5 analyzes the six-degree-of-freedom vibrations of the contact slider, including the in-plane vibration. Chapter 6 gives a new explanation of the cause of the slider's bouncing vibration and compares it with previously reported research. Chapter 7 focuses

on the difference of HDI heat transfer models for an air bearing slider with thermal protrusion. Chapter 8 applies the thermal protrusion to the design of a partial-contact HDI and examines ABS designs for a partial-contact slider with thermal protrusion. Chapter 9 presents the summary and conclusions of this dissertation.

References

- [1] S. X. Wang and A. M. Taratorin, *Magnetic Information Storage Technology*, Academic Press, 1999



(a) A HDD without cover

(b) A sketch of the HDD structure

Fig.1.1. HDD without cover and sketch of the HDD structure (www.westerndigital.com)

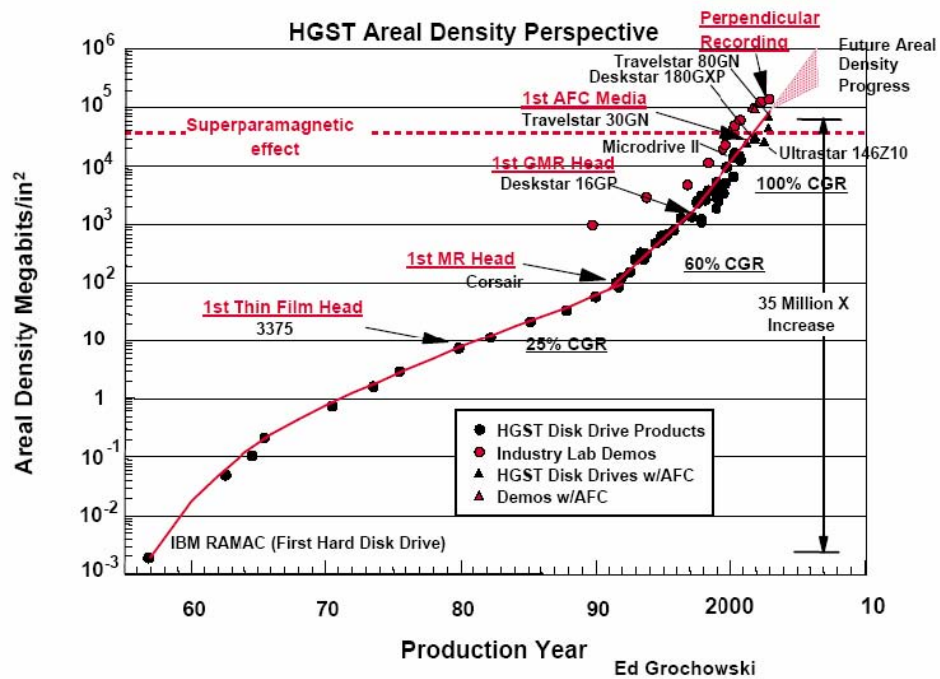


Fig.1.2. Increase of the areal recording density in the HDDs (www.hgst.com)

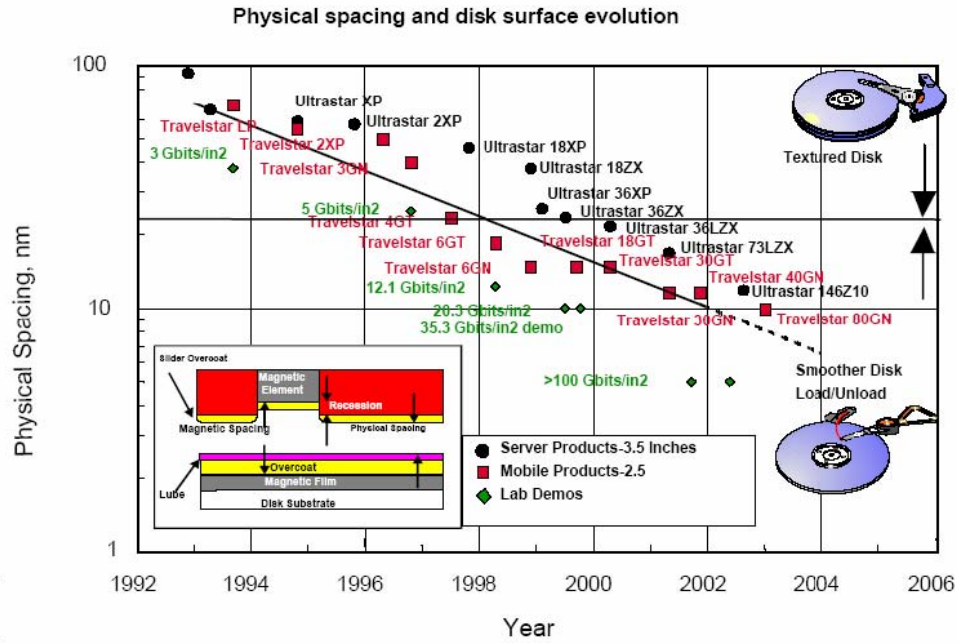


Fig.1.3. Reduction of the physical spacing (flying height) (www.hgst.com)

Evolution of Slider/Air Bearing Surface

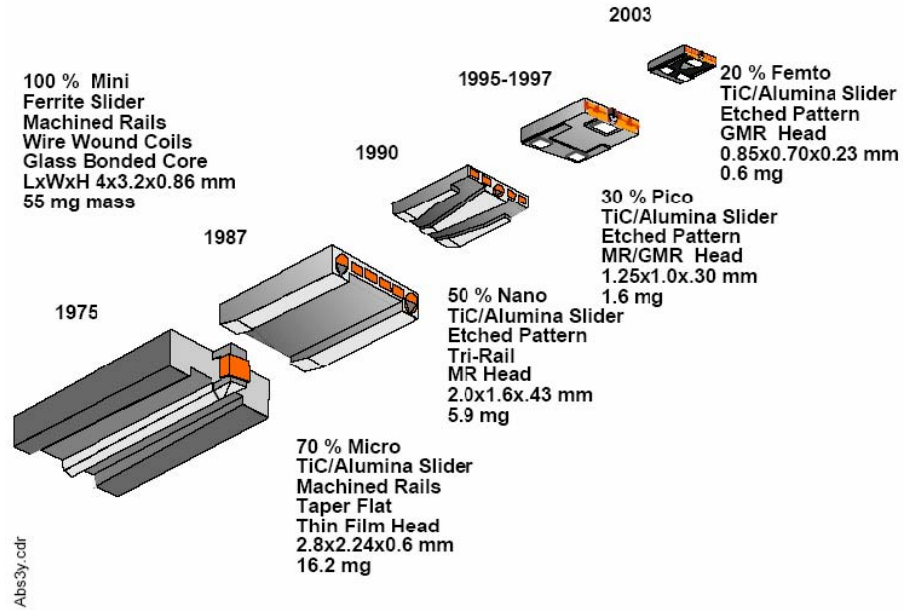


Fig.1.4. Evolution of the slider and air bearing surface (www.hgst.com)

Chapter 2 Contact Models for the Slider-Disk

Contact and Impact

The slider-disk impact and contact need to be properly modeled in the air bearing slider dynamic simulator in order to accurately simulate the dynamics of contact or partial-contact sliders for 1Tbit/in² or higher recording densities in hard disk drives. Static contact models, such as asperity-based contact models and the contact model based on influence coefficients, can be used to model the slider-disk contact and impact, since the contact and impact between the slider and the disk are quasi-static. The limitations of these models are discussed and the algorithms used for applying these models to the slider dynamic simulation are analyzed in order to efficiently use them in the simulation. Other contact models, such as the multi-asperity contact model proposed by Cha and Bogy [1] in the current CML air bearing program and the contact model proposed by Iida and Ono [2] in their simulations for contact and near-contact sliders, are also discussed in this chapter.

2.1 Introduction

The slider-disk spacing has to decrease to less than 3 nm for 1Tbit/in² magnetic recording density, resulting in a high likelihood of slider-disk contact or impact. In the contact or partial-contact head disk interface (HDI) design, the slider's trailing edge is expected to contact the disk surface during the reading and writing process. So the slider-disk impact and contact need to be properly modeled in the air bearing slider dynamic simulator in order to accurately analyze the dynamics of the contact or

partial-contact slider.

Models of the slider-disk contact and impact should be simple and accurate and have an efficient numerical algorithm so they can be used in the slider dynamic simulation. The CML slider dynamic simulator uses the Newmark-Beta method to solve the slider-disk interface dynamic equations [3]. The time step is at most 10^{-6} sec due to the high frequency of the slider's motion. This means that at least 10^3 time steps are required for the simulation of only 1ms of motion. When the slider contacts the disk, the simulator needs to solve for the slider-disk contact force several times as well as solving the dynamic Reynolds Equations for the air bearing pressure, until the entire system of the slider's motion equations converge at each time step. Hence the slider dynamic simulation needs a numerically efficient model for the slider-disk impact and contact.

In the early numerical simulations of the slider dynamics, the coefficient of restitution model of the slider-disk impact was used to calculate the approximate impact force and the speed of the slider after impact [4]. Another common approach was to use the contact stiffness and damping for the calculation of the slider-disk impact force [5]. These two methods are very convenient for computation; however, it is difficult to obtain the values of the required parameters, such as the coefficient of restitution, contact stiffness and damping coefficients for a 3-D slider-disk contact. Also the coefficient of restitution model cannot give the contact duration and the contact force at the same time. Later several static contact models were applied to the simulation, for example, the Greenwood-Williamson (GW) model [6], CEB model [7] and KE model [8]. All of these models belong to the class of asperity-based contact models. Cha and Bogy proposed a multiple asperity impact model [1], which is based on Chang and Ling's elastic-plastic model [9]. Peng et al. [10] used an elastic contact model based on influence coefficients

to simulate the slider-disk contact. Iida and Ono [2] numerically calculated the contact force considering the asperity contact and the deformation of the base plane of each asperity due to the bulk deformation. Influence coefficients are used in their model to calculate the deformation of each asperity's base plane. Although the finite element method (FEM) is adequate in solving elastic-plastic contact problems with acceptable accuracy [11 and 12], its requirement for a large number of elements reduces its effectiveness in analyzing surface contact with a practical size system. Its high computation cost makes it almost impossible to use the FEM to analyze the slider-disk contact in the slider dynamic simulation.

Currently the CML air bearing program uses the GW model and CEB model (also called elastic-plastic model, i.e. EP model) for the slider-disk asperity contact, which occurs when the gap between the slider and the disk is less than the glide height but higher than zero, and it uses Cha's model [1] for the crash contact, which occurs when the slider-disk gap is less than zero. In this Chapter we analyze all of these contact models, i.e. the asperity-based models and the elastic model with influence coefficients. Their applications and limitations to the slider dynamic simulation are examined. Finally a preferred approach for the simulation of the slider-disk contact and impact is proposed.

2.2 Slider-Disk Quasi-Static Impact

The dynamic impact between the slider and disk can be modeled as a quasi-static impact. The CML slider dynamic simulation shows that when the slider impacts the disk the impact speed of the slider is on the order of 10^{-1} m/s, which is much less than the elastic wave speeds in the slider and the disk. The sliding speed of the slider with respect to the disk, which is proportional to the disk rotation speed and the radial position of the

slider, is on the order of 10^1 m/s. This value is also much smaller than the elastic wave speeds. So the slider-disk impact is quasi-static, which means that the deformation is restricted to the vicinity of the contact area and can be obtained using the static contact theory. The elastic wave motion in the bodies can be ignored when only the slider-disk contact is considered. So we can use static contact models to approximate the slider-disk contact. In fact the asperity-based contact models, such as the GW model and the CEB model used by Hu [3] in the slider dynamic simulation and the KE model used by Suh and Polycarpou [13] for their two dimensional slider simulation, are all static contact models, as is Cha's multi-asperity contact model [1]. The influence coefficient model of contact is based on static linear elasticity and it can also be used as a quasi-static impact model.

2.3 Decoupled Normal Pressure and Tangential Friction

In the quasi-static slider-disk contact problem the normal pressure and the friction traction can be decoupled without significant loss of accuracy. Johnson [14] showed analytically that the influence of frictional traction on the normal pressure is very small for a sliding punch over the surface of a half-space with a friction coefficient 0.5. The friction coefficient between the slider and the disk is usually less than 0.5 due to the lubricant and carbon overcoat. The default value used in CML simulation is 0.3. So we can employ the contact models to obtain the contact force and then obtain the friction force through Coulomb's law with a constant friction coefficient.

2.4 Asperity-based Contact Models

Nomenclature

A_n nominal contact area

- A real contact area
- d separation between the mean asperity height of the slider and that of the disk
- d^* normalized separation ($d^* = d / \sigma_s$)
- E_s Young's modulus of the slider
- E_d Young's modulus of the disk
- E Hertz elastic modulus ($E = (\frac{1-\nu_s^2}{E_s} + \frac{1-\nu_d^2}{E_d})^{-1}$)
- H hardness of the softer material
- K hardness factor ($K = 0.454 + 0.410\nu$)
- N total number of asperities
- P total contact force
- R asperity radius of curvature
- t lubricant thickness
- u height of an asperity measured from the mean of asperity heights
- u^* normalized asperity height ($u^* = u / \sigma_s$)
- y_s distance between the mean of asperity heights and the mean of surface heights
- η area density of asperities
- ν Poisson's ratio of the softer material among the slider and the disk
- ν_s Poisson's ratio of the slider
- ν_d Poisson's ratio of the disk
- σ standard deviation of surface heights
- σ_s standard deviation of asperity height

ω contact interference of an asperity

ω_c critical interference at the inception of plastic deformation inside the asperity

ψ plasticity index

2.4.1 Single Asperity Contact and Contact Models

The general approach of an asperity-based contact model is to incorporate a single asperity contact into a statistical model of multiple asperity contacts. The contact of two rough surfaces can be modeled by an equivalent single rough surface contacting a flat rigid plane, as proved by Greenwood and Tripp [15]. For the equivalent rough surface, five assumptions are usually adopted in an asperity-based model.

- (1) The rough surface is isotropic.
- (2) The asperities have the same simple geometry near their summits, for example the asperities are spherical or ellipsoidal.
- (3) The asperity heights vary randomly but follow a probability distribution, for example, a Gaussian distribution.
- (4) Asperities deform due to the contact with the rigid surface. But asperities are far apart and interactions between them are negligible.
- (5) Bulk deformation is also negligible.

The first asperity-based contact model was presented in the pioneering work of Greenwood and Williamson (GW model) [6]. It is based on the Hertz elastic contact solution for a single elastic spherical asperity. So it is mainly valid for purely elastic contact. Much earlier some purely plastic contact models were proposed by Abbott and Firestone [16]. They were extended to asperity-based contact models for purely plastic contact. To bridge the gap between the purely elastic and the purely plastic contact,

Chang et al. [7] proposed the CEB model by introducing a critical interference (ω_c), above which an elastic contacting asperity turns to fully plastic deformation. The fully plastically deformed asperity is assumed to have a uniformly distributed contact pressure on the contact area and conserve the volume of the asperity tip. However, this simplification causes a discontinuity in the contact load at the transition from elastic to plastic contact. Evseev et al. [17], Chang [18] and Zhao et al. [19] proposed various mathematical modifications to smooth the discontinuity. Kogut and Etsion [8] developed an FEM solution to the elasto-plastic contact between a sphere and a flat surface and revised the CEB elastic-plastic model to the KE model, which does not have the discontinuity.

The GW model, CEB model and KE model are typical asperity-based contact models, which assume that the asperity tips are hemispheres with the same radius and the asperity heights are normally distributed. McCool [20] relaxed these two assumptions and treated the rough surface as anisotropic with a random distribution of asperity radii. However the results showed good agreement with those of the simple GW model. The GW model and CEB model, because of their simplicity, were extended to different asperity geometries and asperity height distributions, Horng [21], Kogut and Etsion [22], Yu and Polycarpou [23]. Also other modifications of these models were made, for example, the modification with a varying hardness by Jackson and Green [24]. However these papers [21-24] fail to show that the two simple assumptions of the GW, CEB and KE models produce results that deviate from real contact interfaces. In this Chapter we accept the assumptions of simple spherical asperities and Gaussian distribution of asperity heights and compare the three typical probabilistic models, i.e. the GW model, CEB model and KE model.

Obviously Assumptions (4) and (5) limit the applicability of the asperity-based

contact models. When the surface separation is less than zero, the asperities can undergo large deformations which may violate Assumption (4). For a large average contact pressure, the bulk deformation may become significant, which violates Assumption (5). So asperity-based contact models are valid only when the surface separation is larger than zero ($d > 0$) and the nominal contact pressure is much less than the hardness of the softer material in the contact interface ($\bar{p} \ll H$).

2.4.2 Surface Roughness Parameters

In the GW model, CEB model and KE model, a rough surface is described by the standard deviation of the asperity heights, the areal density of the asperities and the radius of curvature of their summits. McCool [25] showed a systematic way to obtain these parameters from the surface profile $z(x)$, assuming that $z(x)$ is a Gaussian random variable. Three spectral moments of the profile $z(x)$ are defined as,

$$m_0 = \text{Average}[z^2], \quad m_2 = \text{Average}\left[\left(\frac{dz}{dx}\right)^2\right], \quad m_4 = \text{Average}\left[\left(\frac{d^2z}{dx^2}\right)^2\right]. \quad (1)$$

Two isotropic rough surfaces in contact can be replaced by an equivalent rough surface contacting a rigid flat surface. Then three spectral moments of the equivalent rough surface are,

$$m_0 = (m_0)_1 + (m_0)_2, \quad m_2 = (m_2)_1 + (m_2)_2, \quad m_4 = (m_4)_1 + (m_4)_2. \quad (2)$$

Obviously m_0 is the variance of surface heights, i.e., the surface height standard deviation $\sigma = (m_0)^{1/2}$. The radius of curvature, the asperity density, and the asperity height standard deviation can be expressed as [25],

$$R = 0.375 \left(\frac{\pi}{m_4}\right)^{1/2}, \quad \eta = \frac{m_4}{6\pi\sqrt{3}m_2}, \quad \sigma_s = \sqrt{\sigma^2 - \frac{3.717 \times 10^{-4}}{\eta^2 r^2}}. \quad (3)$$

From a mathematical point of view, the above equations can be proved only for Gaussian random surfaces [26]. They are not valid for a Weibull random surface. So using a non-Gaussian asperity height distribution with the above equations, which was carried out in [23], has not been validated.

These three parameters, i.e. the radius of curvature, asperity density, and asperity height standard deviation, are scale-dependent. In practice the surface topography is not strictly a stationary random process and three spectral moments of the height distribution depend on the length of the statistical sample [27]. This means that instruments with different resolutions and scan lengths yield different values of these statistical parameters for the same surface. Majumdar and Bhushan [28] analyzed their dependence on the spatial resolution and surface magnification for a magnetic tape surface and a magnetic disk surface. They proposed a new contact model in which the rough surfaces are characterized by fractal geometry instead [29]. Based on that, contact analyses of elastic-plastic fractal surfaces were carried out [30 and 31]. However, all of these analyses retain Assumption 4 and Assumption 5, and they did not cite any experimental work as a proof that fractal contact models are superior to asperity-based contact models.

2.4.3 A Proper Model for Slider-Disk Asperity Contact

As mentioned above, the GW model is valid for purely elastic contact, the CEB model is a rough extension to elastic-plastic contact and the KE model is a more accurate elastic-plastic model based on the FEM analysis, but with the cost of much more complicated expressions. For specified rough surfaces all three of these models give the contact load and the real contact area as functions of the surface separation (d), where, in fact, $d=FH-ys$, or $d=FH-ys-t$ if a lubricant thickness t is considered.

GW model

$$P(d) = \frac{2}{3}(\pi RKH\omega_c)(A_n\eta) \int_d^\infty I^{1.5} \quad (4)$$

$$A(d) = (\pi R\omega_c)(A_n\eta) \int_d^\infty I^1 \quad (5)$$

CEB model

$$P(d) = \frac{2}{3}(\pi RKH\omega_c)(A_n\eta) \left(\int_d^{d+\omega_c} I^{1.5} + 1.5 \int_{d+\omega_c}^\infty \left(2 - \frac{\omega_c}{u-d}\right) I^1 \right) \quad (6)$$

$$A(d) = (\pi R\omega_c)(A_n\eta) \left(\int_d^{d+\omega_c} I^1 + \int_{d+\omega_c}^{d+6\omega_c} \left(2 - \frac{\omega_c}{u-d}\right) I^1 \right) \quad (7)$$

KE model

$$P(d) = \frac{2}{3}(\pi RKH\omega_c)(A_n\eta) \left(\int_d^{d+\omega_c} I^{1.5} + 1.03 \int_{d+\omega_c}^{d+6\omega_c} I^{1.425} + 1.4 \int_{d+6\omega_c}^{d+110\omega_c} I^{1.263} + \frac{3}{K} \int_{d+110\omega_c}^\infty I^1 \right) \quad (8)$$

$$A(d) = (\pi R\omega_c)(A_n\eta) \left(\int_d^{d+\omega_c} I^1 + 0.93 \int_{d+\omega_c}^{d+6\omega_c} I^{1.136} + 0.94 \int_{d+6\omega_c}^{d+110\omega_c} I^{1.146} + 2 \int_{d+110\omega_c}^\infty I^1 \right) \quad (9)$$

where $I^\alpha = \left(\frac{u-d}{\omega_c}\right)^\alpha \phi(u) du = \left(\frac{u-d}{\omega_c}\right)^\alpha \frac{1}{\sqrt{2\pi}\sigma_s} \exp\left(-\frac{u^2}{2\sigma_s^2}\right) du$ holds for the Gaussian

random surfaces.

The CEB model assumes the asperities are either elastically deformed ($\omega < \omega_c$) or fully plastically deformed ($\omega \geq \omega_c$), with the corresponding two terms on the right hand sides of Equations (6) and (7). However, the KE model uses the FEM results and asserts that asperities have four different deformation states. They are elastically deformed asperities ($\omega < \omega_c$), elastic-plastically deformed asperities with a plastic region under the contact interface ($\omega_c \leq \omega < 6\omega_c$), elastic-plastically deformed asperities with a plastic annulus on the contact interface ($6\omega_c \leq \omega < 110\omega_c$), and fully plastically deformed asperities ($\omega \geq 110\omega_c$). These four states correspond to the four terms on the right hand

sides of Equations (8) and (9).

Although the right hand sides of Equations (4-9) have many variables, they can be reduced to functions of the separation d and the plasticity index Ψ . The plasticity index, which is defined by Greenwood and Williamson and expressed as $\Psi = (\omega_c / \sigma_s)^{-1/2}$, determines the main deformation state of the contacting asperities, i.e. elastic, elastic-plastic, or plastic. Figure 2.1 shows the Gaussian distribution of asperity heights. All of the asperities with heights larger than the separation are in contact, shown as a dark region in Figure 2.1. All of the asperities with heights larger than the critical interference plus the separation are in elastic-plastic or plastic deformation. It is obvious that if the separation is larger than $3\sigma_s$, the number of asperities in contact is negligible and in fact the surfaces are practically separated. The number of asperities in elastic-plastic deformation is $N \int_{\omega_c+d}^{\infty} \phi(u) du$. Here we have a restriction $d > 0$ so that the assumption (4) is valid. The above number of asperities in elastic-plastic deformation is negligible if the critical interference is less than $3\sigma_s$, which corresponds to $\Psi < 0.58$. This is consistent with Greenwood and Williamson's comment [6] that when $\Psi < 0.6$ plastic contact could be caused only if the nominal pressure between two surfaces were very large. Further, we make the following conclusions,

- (1) The contacting asperities are mainly in elastic deformation if $\Psi < 0.58$, i.e. $\omega_c > 3\sigma_s$.
- (2) The number of plastically deformed asperities is negligible if $\Psi < 6.06$,
i. e. $110\omega_c > 3\sigma_s$.
- (3) If $0.58 < \Psi < 1.41$, i.e. $\omega_c < 3\sigma_s < 6\omega_c$, the number of elastic-plastically deformed asperities with plastic annulus on the contact interface is negligible, but the

elastic-plastically deformed asperities with a plastic region below the contact interface needs to be considered.

So if $\Psi < 1.41$ the asperities are mainly in elastic deformation or elastic-plastic deformation with a plastic region below the contact interface, which corresponds to the first two terms in Equations (8) and (9). Notice that the term in (8) $1.03 \int_{d+\omega_c}^{d+6\omega_c} I^{1.425}$ is close to $1.00 \int_{d+\omega_c}^{d+6\omega_c} I^{1.5}$ and the term in (9) $0.93 \int_{d+\omega_c}^{d+6\omega_c} I^{1.136}$ is close to $1.00 \int_{d+\omega_c}^{d+6\omega_c} I^1$. So we may expect that the KE model produces results close to those produced by the GW model when $\Psi < 1.41$.

Numerical results of three cases with different plasticity indices of the slider-disk contact are obtained using the GW model, CEB model and KE model. These three cases have typical slider and disk roughnesses and material parameters [13], as shown in Table 2.1, and they have $\Psi = 0.836, 0.587$ and 0.386 , respectively. For each case, the contact load versus the separation and the contact area versus the separation are plotted for these three contact models, respectively. As shown in Figure 2.2, the difference between the results of these three models is very small except for case 1, where the result of the CEB model deviates from those of the GW model and KE model for separations less than 1nm. In case 1 $\Psi = 0.836$, the asperities are either in elastic deformation or in elastic-plastic deformation with plastic regions below the contact interface. The CEB model improperly assumes all of the elastic-plastically deformed asperities are in fully plastic deformation, while the contact force and contact area of these elastic-plastically deformed asperities are much closer to those of elastically deformed asperities than to those of fully plastically deformed asperities. This is the reason why it gives different results. From this

point of view, the CEB model may not be accurate for the slider-disk contact analysis with a large ψ and a small separation.

For the slider-disk asperity contact, if the material parameters E is 85.29 GPa, H is 2.5 GPa, and ν is 0.2, the roughness parameters σ_s is less than 2 nm and R is on the order of

1 μm , then we can expect the plasticity index $\psi = \left(\frac{\omega_c}{\sigma_s}\right)^{-1/2} = \frac{2E}{\pi KH} \left(\frac{\sigma_s}{R}\right)^{1/2}$ to be around

1. So the contacting asperities are mainly in elastic or elastic-plastic deformation. Hence the difference between the GW model and the KE model is expected to be very small for slider-disk asperity contact. For simplicity we will use the GW contact model in the slider's dynamic simulation. If the slider-disk contact has $\Psi > 0.58$, we can turn to the KE model for better accuracy, but the GW model is still a good approximation. However, the CEB model may not be applicable to the slider-disk contact with $\Psi > 0.58$, as analyzed in the above slider-disk asperity contact cases.

2.4.4 Numerical Implementation of the GW Model and the KE Model

Notice that all of the terms in the Equations (4), (5), (8), and (9) have the following form,

$$\begin{aligned} \int_{l(d,\omega_c)}^{u(d,\omega_c)} I^\alpha &= \int_{l(d,\omega_c)}^{u(d,\omega_c)} \left(\frac{u-d}{\omega_c}\right)^\alpha \frac{1}{\sqrt{2\pi}\sigma_s} \exp\left(-\frac{u^2}{2\sigma_s^2}\right) du \\ &= \left(\frac{\sigma_s}{\omega_c}\right)^\alpha \int_{l(d,\omega_c)}^{u(d,\omega_c)} \left(\frac{u-d}{\sigma_s}\right)^\alpha \frac{1}{\sqrt{2\pi}\sigma_s} \exp\left(-\frac{u^2}{2\sigma_s^2}\right) du \\ &= \psi^{2\alpha} \int_{l(d^*,\psi)}^{u(d^*,\psi)} (u^* - d^*)^\alpha \frac{1}{\sqrt{2\pi}} \exp\left(-\frac{u^{*2}}{2}\right) du^*, \end{aligned} \quad (10)$$

where $u(d,\omega_c)$ and $l(d,\omega_c)$ are the upper and lower bounds of the integration, respectively. As seen from Equation (10), the integral is expressed as a function of d if Ψ is given. So in the GW model and the KE model the contact load and contact area are

only functions of the separation when the plasticity index of the contact interface is given.

To avoid the integration process at each time step, a table look-up method can be used in the computation. The look-up tables are composed of all integration results for various values of d^* . For the GW model the upper bound and lower bound in Equation (10) are independent of the given Ψ , so the tables can be predetermined. For the KE model the upper bound and lower bound in Equation (10) depend on the input Ψ . So the look-up tables have to be dynamically established in the program for different input values of Ψ . The improper integrals, which have ∞ as an upper bound, are approximated by proper integrals. Figure 2.1 shows that the density function of the Gaussian distribution,

i.e. $\frac{1}{\sqrt{2\pi}\sigma_s} \exp(-\frac{u^2}{2\sigma_s^2})$, decreases to near zero extremely fast as u increases beyond $3\sigma_s$.

So the upper bound in equation (10) can be replaced by a sufficiently large number, for example $3\sigma_s$ or $6\sigma_s$, without significant loss of accuracy. The Romberg method [32] is used to calculate the proper integrals to establish the tables, instead of the numerical integration method currently in the CML air bearing code. With the Romberg method, the CML air bearing code does not have the convergence problem when calculating the contact force.

Meshing the slider ABS is required in order to apply an asperity-based contact model to the slider-disk asperity contact. Due to the pitch and roll of the slider motion and the air bearing surface (ABS) patterns, the slider surface is not parallel to the disk. The slider ABS is meshed into small grids in the numerical simulation. Each grid on the ABS is assumed to have a uniform separation from the disk and the slider-disk contact force and contact area are hence discretized as step functions. The GW model or the KE model is

applied to each grid to obtain the contact load and contact area. Then the total contact load and contact area are the summation of the contact load and contact area of all grids. The table look-up method speeds up this process. In the CML air bearing simulation an adaptive grid generation based on the air pressure gradient is used to numerically solve the Reynolds Equation [33]. In this adaptive mesh the grid density is usually higher at ABS regions where the flying height is lower. Those places with lower flying heights are more likely to contact the disk. We can also use this adaptive mesh to analyze the slider-disk asperity contact in the slider dynamic simulation. This avoids introducing another mesh into the simulation.

Both contact force and contact area are nonlinear functions of separation. So the effects of pitch and roll on the contact force and contact area are not negligible even for pitch and roll angles on the order of microradians. Figure 2.3 shows the relationships between the contact force and the pitch angle and between the contact area ratio and the pitch angle for the rough slider and disk surfaces (case 1 in Table 2.1) with a minimum separation of 2 nm. Here the tailing pad of the slider is a $30\ \mu\text{m} \times 30\ \mu\text{m}$ square and it is in asperity contact with the disk. We can see that the GW model and KE model give the same results and that the contact force and contact area strongly depend on the pitch angle. We may also expect that the roll angle has a similar effect on the contact force and contact area. But the effect of the roll angle is less than that of the pitch angle, since the roll angle is much smaller than the pitch angle. The slider-disk contact simulation by Suh and Polycarpou [13] neglected the effect of the pitch and roll and only considered the effect of the contact pad area, i.e. nominal contact area (A_n), upon the total contact force. This may not be accurate in common cases.

2.4.5 Asperity Contact Models with Assumptions 4 and 5 Relaxed

There are several advanced asperity-based contact models that relax the last two assumptions of a typical asperity-based contact model, i.e. the assumption of no asperity interactions and the assumption of no bulk deformation. However, all of them are somewhat questionable.

For example, Zhao and Chang [34] proposed a model of asperity interactions in elastic-plastic contact of rough surfaces, which basically is a kind of asperity-based contact model. First they applied Saint-Venant's Principle of elasticity to equate the deformation at a given asperity due to pressures at all other contacting asperities, shown in Figure 2.4(a), to the deformation at that asperity due to an equivalent uniform pressure applied over the surface area outside the region of that asperity, shown in Figure 2.4(b). However, Saint-Venant's Principle is at best valid only for the strain and stress of a given point remote from loading regions. So it can not validate the equivalence of the two situations shown in Figure 2.4. To consider the interactions between asperities, they used the linear elasticity theory and the influence coefficient (or Love's formula [35]) to calculate the deformation of a given asperity due to the forces at all other contacting asperities, while the deformation of all contacting asperities is assumed to be elastic-plastic in their model. This approach also is questionable.

Iida and Ono [2] included the bulk deformation in their asperity-based elastic contact model for the contact and near-contact sliders. In their model, the displacement of the tip of each asperity is composed of two parts. One part is due to the deformation of the tip of the given asperity under Hertzian contact and the other part is due to the deformation of the base plane of the given asperity under the asperity contact forces of all other contacting asperities. In this sense, for the contact of a rigid flat surface and a single

spherical asperity on a half space, the displacement of the asperity tip is only due to the Hertzian contact between the rigid flat surface and the spherical asperity, which depends only on the Young's modulus of the asperity and the contact load. However, suppose that Young's modulus of the half space is different from that of the spherical asperity, it is obvious that the displacement of the asperity tip increases as the Young's modulus of the half space decreases. So Iida and Ono's contact model is also questionable.

2.5 Contact Model Based on Influence Coefficients

2.5.1 Influence Coefficient and Corresponding Contact Model

This kind of contact model is based on the linear elasticity theory of loading on an isotropic elastic half-space. The influence coefficient describes the effect of a uniform pressure acting on a rectangular area, as analyzed by Love [35]. The deflection of a general point (x, y) on the surface due to a uniform pressure p acting on a rectangular area $2a \times 2b$ centered at the origin is given by Love's formula [35],

$$\begin{aligned} \bar{u}_z(x, y; a, b) &= p \cdot \\ &\frac{1 - \nu^2}{\pi E} \left\{ (x + a) \ln \left[\frac{(y + b) + \sqrt{(y + b)^2 + (x + a)^2}}{(y - b) + \sqrt{(y - b)^2 + (x + a)^2}} \right] + (y + b) \ln \left[\frac{(x + a) + \sqrt{(y + b)^2 + (x + a)^2}}{(x - a) + \sqrt{(y + b)^2 + (x - a)^2}} \right] \right. \\ &\quad \left. + (x - a) \ln \left[\frac{(y - b) + \sqrt{(y - b)^2 + (x - a)^2}}{(y + b) + \sqrt{(y + b)^2 + (x - a)^2}} \right] + (y - b) \ln \left[\frac{(x - a) + \sqrt{(y - b)^2 + (x - a)^2}}{(x + a) + \sqrt{(y - b)^2 + (x + a)^2}} \right] \right\} \\ &= p \frac{1 - \nu^2}{\pi E} c(x, y; a, b) \end{aligned} \quad (11)$$

Here the function c is called the influence coefficient, which relates the normal pressure in the rectangle with the size of $2a \times 2b$ to the normal displacement at a given point (x, y) . Obviously c is only a function of the position of the given point and the size of the rectangular area. Love also found expressions from which the stress components at a

general point in the solid can be obtained. He commented that the component of shear stress theoretically becomes unbounded at the corners of the rectangle, but elsewhere all the stress components are bounded. These results are useful in the numerical solution of more general static contact problems of two bodies with uniformly loaded rectangles as “boundary elements”. First, the normal and tangential tractions can be decoupled with only a small loss of precision by neglecting the effect of the tangential traction on the normal pressure, which arises when the materials of the two bodies are different. Then the discretized normal displacement of a contacting rough surface and the discretized normal pressure are related through the influence coefficients. Finally, the normal displacement of the contacting rough surface and the normal pressure are solved through numerical methods. This approach is systematically described by Johnson [14].

For contact with a layered half space or contact in cases where the normal pressure and the tangential traction are coupled, the influence coefficient can be calculated using the FEM [36], where the influence of the applied unit load on the deflection at each node is analyzed using the finite element analysis, or using the elasticity solution for a unit load on the surface of the half space [37], where the Papkovitch-Neuber potentials are employed in a Fast Fourier analysis. By either method, the influence coefficient is still a function of the relative position and the size of the loading area.

2.5.2 Application to Slider-Disk Contact

Several approximations are made to simplify the slider-disk contact problem. We need not consider the layered structure of the disk since we are not interested in the stress field in the disk. The disk is simply assumed to be a homogeneous isotropic half space. As discussed before, the normal pressure and the friction traction are decoupled without significant loss of accuracy. So the influence coefficient expressed in Equation (11) can

be directly used. The slider and the projection of the slider on the disk are discretized into grids with the same mesh as shown Figure 2.5. Each grid rectangle has a center node. The gap between the slider and the disk, the slider profile and the disk profiles, the contact pressure between the slider and the disk, and the elastic normal displacements of the slider and disk surfaces due to contact are all assumed to be uniform on each rectangular grid with the value evaluated at the center node. In another words, all of them are discretized to stepwise functions.

The slider-disk gap h is the distance between the slider and disk profiles $Z_{(s)}$ and $Z_{(d)}$, i.e., $h = Z_{(s)} - Z_{(d)}$. In the slider's dynamic simulation h corresponds to the motion of the slider, which means h_i , the gap at node i , has the following property,

$$h_i \begin{cases} > 0, & \text{when node } i \text{ is not in contact} \\ < 0, & \text{when node } i \text{ is in contact} \end{cases} .$$

Provided there is no interpenetration, the elastic normal displacements of node i on the slider $\bar{u}_{z(s)i}$ and the elastic displacement of the corresponding node on the disk $\bar{u}_{z(d)i}$, then satisfy the relationship,

$$\bar{u}_{z(s)i} + \bar{u}_{z(d)i} + h_i \begin{cases} = 0, & \text{within a contact region} \\ > 0, & \text{outside contact regions} \end{cases} \quad (12)$$

The influence coefficient c_{ij} is used to express the displacement at node i due to a unit pressure element centered at node j acting on the rectangular grid. The total displacement at node i is then expressed by,

$$\bar{u}_{z(s)i} = \frac{1-\nu_s^2}{\pi E_s} \sum c_{ij(s)} p_j, \quad \bar{u}_{z(d)i} = \frac{1-\nu_d^2}{\pi E_d} \sum c_{ij(d)} p_j . \quad (13)$$

where $c_{ij(s)}$ and $c_{ij(d)}$ are the influence coefficient on the slider and on the disk surface, respectively. If we also apply Equation (11) to the slider surface for $c_{ij(d)}$, then we can obtain a similar equivalence of the contact between two rough surfaces and the contact between a flat and a rough surface as in [15]. Explicitly the relative displacement can be expressed as,

$$\begin{aligned}\bar{u}_{z(s)i} + \bar{u}_{z(d)i} &= \frac{1-\nu_s^2}{\pi E_s} \sum c_{ij} p_j + \frac{1-\nu_d^2}{\pi E_d} \sum c_{ij} p_j \\ &= \sum \left(\frac{1-\nu_s^2}{\pi E_s} + \frac{1-\nu_d^2}{\pi E_d} \right) c_{ij} p_j \\ &= \sum C_{ij} p_j ,\end{aligned}$$

where $C_{ij} = \frac{1-\nu_s^2}{\pi E_s} c_{ij} + \frac{1-\nu_d^2}{\pi E_d} c_{ij} = \frac{1}{E^*} c_{ij}$.

Then Equation (12) can be expressed as,

$$\sum C_{ij} p_j \begin{cases} = -h_i, & \text{within a contact region} \\ > -h_i, & \text{outside contact regions,} \end{cases} \quad (14)$$

Here the C_{ij} 's form a non-sparse matrix of the influence coefficients for the slider-disk contact interface and they define a linear system that relates the normal pressure to the elastic normal displacement. To simulate the slider dynamics, we need to solve the linear system and obtain the pressure elements. Notice that the pressure element p_i should satisfy $0 \leq p_i \leq H$. The total contact load P carried by the contact region is the sum of the pressure elements, i.e.

$$P = \sum p_i s_i , \text{ where } s_i \text{ is the area of the grid at node } i.$$

Obviously this elastic model with the influence coefficients considers the interactions between nearby grids and the effect of bulk deformation. This model can simulate the

contact between discretized real surfaces. However, this model is not applicable when a large number of contact nodes are plastically deformed, since the basis of the model is from linear elasticity theory. The accuracy of this model strongly depends on the fineness of the mesh; however, a fine discretization with a large grid number dramatically increases the computational time. So an efficient numerical scheme is of vital importance in applying this model to simulate the slider-disk contact.

2.5.3 Numerical Schemes for Solving the Obtained Linear System

Johnson [14] described two numerical methods – a matrix inversion method and a variational method – to solve the linear system, which is produced by the contact model based on influence coefficients for the normal pressure. In fact, almost all papers on the contact model based on influence coefficients uses one of these two numerical schemes, for example, [37-40]. Here we modify these two numerical methods and make them suitable for the simulation of slider-disk contact.

a) Conjugate Gradient (CG) method

The problem of the slider-disk contact is to find each contact region with known contact pressure p for a certain slider-disk gap h . A first approximation to the contact regions is the geometric overlap regions, i.e., all the nodes in contact regions are the nodes $\{Node\ i: h_i < 0\}$. Then the CG method instead of matrix inversion is used to solve the linear equations,

$$\sum_{j \in \text{Contact Region}} C_{ij} p_j = -h_i, \quad (15)$$

or in a matrix form, $[C]\{p\} = -\{h\}$.

The solution of Equation (15) may have pressure elements at some nodes with negative values, which implies that a tensile traction is required at those nodes to maintain contact

over the entire assumed contact region. Then a new approximation to the contact region can be taken as the former region without those negative pressure nodes. Repeat this step and refine the approximation of the contact region until a set of positive pressure elements is achieved. The obtained solution may have pressure elements at some nodes larger than the hardness H . Then we change the values of these pressure elements to H . With this modified pressure elements and Equation (14), i.e.

$$\sum_{j \in \text{Contact Region}} C_{ij} p_j \begin{cases} = -h_i, & \text{then node } i \text{ is in the new approximation of the contact region} \\ > -h_i, & \text{then node } i \text{ is out of the new approximation of the contact region} \end{cases}$$

the new approximation to the contact region can be calculated. Then we repeat the steps mentioned above until all of the pressure elements have values between 0 and H . The algorithm is illustrated in Figure 2.8.

The CG method itself is an iterative scheme that generates a sequence of approximations of the solution from an arbitrary initial approximation [32]. The method is represented by the following recurrence formulas,

$$\begin{aligned} \{p^{(s+1)}\} &= \{p^{(s)}\} + \frac{\{f^{(s)}\}^T \{t^{(s)}\}}{\{t^{(s)}\}^T [C] \{t^{(s)}\}} \{t^{(s)}\} \\ \{f^{(s+1)}\} &= \{f^{(s)}\} - \frac{\{f^{(s)}\}^T \{t^{(s)}\}}{\{t^{(s)}\}^T [C] \{t^{(s)}\}} [C] \{t^{(s)}\} \\ \{t^{(s+1)}\} &= \{f^{(s+1)}\} + \frac{\{f^{(s+1)}\}^T \{f^{(s+1)}\}}{\{f^{(s)}\}^T \{f^{(s)}\}} \{t^{(s)}\} \end{aligned}$$

where $s = 0, 1, 2, \dots$ is the step number. $\{t\}$ and $\{f\}$ are vectors of the same size as the pressure vector $\{p\}$. The starting pressure vector $\{p^{(0)}\}$ is arbitrary and $\{t^{(0)}\} = \{f^{(0)}\} = -\{h\} - [C] \{p^{(0)}\}$.

b) Gradient Projection Conjugate Gradient (GPCG) method

Mathematically the solution of the linear equations $[K]\{a\} = \{b\}$ is also the solution that minimizes the convex function $\Pi(\{a\}) = \frac{1}{2}\{a\}^T[K]\{a\} - \{a\}^T\{b\}$ if $[K]$ is a positive definite matrix. So obtaining the solution $\{p\}$ of the linear systems formed by the influence coefficient matrix, i.e. $[C]\{p\} = -\{h\}$, is equivalent to minimizing the function $f(\{p\}) = \frac{1}{2}\{p\}^T[C]\{p\} + \{h\}^T\{p\}$ if $[C]$ is a positive definite matrix, which is the case for a uniform mesh (the adaptive mesh is analyzed later). And the iterations in the CG method to obtain a solution $\{p\}$ with all components bounded by 0 and H are equivalent in effort to that required to minimize the function $f(\{p\}) = \frac{1}{2}\{p\}^T[C]\{p\} + \{h\}^T\{p\}$ within a bounded region $[0, H]$ for all components.

It was shown by Kalker [41] that the true contact area and distribution of surface tractions minimize the total complementary energy V^* ,

$$V^* = \frac{1}{2} \int_{\text{contact region}} p(\bar{u}_{z(s)} + \bar{u}_{z(d)i}) ds + \int_{\text{contact region}} ph ds. \quad (16)$$

Using a uniform mesh to discretize all functions we can express Equation (16) as,

$$\begin{aligned} V^* &= \frac{1}{2} \sum_{i,j \in \text{contact region}} s_i p_i C_{ij} p_j + \sum_{j \in \text{contact region}} s_i p_i h_i \\ &= s \left(\frac{1}{2} \sum_{i,j \in \text{contact region}} p_i C_{ij} p_j + \sum_{j \in \text{contact region}} p_j h_j \right) \\ &= sf(\{p\}). \end{aligned} \quad (17)$$

Equation (17) suggests the equivalence between minimizing V^* and minimizing the function $f(\{p\})$. The object function for minimization in the case of an adaptive mesh is discussed later.

We can still use the geometric overlap regions, which have all the nodes in the contact

region $\{\text{Node } i: h_i < 0\}$, as a first approximation to the contact area. Then the slider-disk contact problem becomes a standard quadratic minimization problem with simple bound constraints. Here we propose to use the GPCG method to deal with the quadratic minimization. The GPCG method was developed by More and Toraldo in 1991 [42]. It uses the conjugate gradient method to explore one active set of constraints and the gradient projection method to move to a new active set. It combines a multiple activation/inactivation strategy of gradient projection with the finite termination property of the CG method. It works efficiently for large-scale bound-constrained quadratic programming problems with a small number of iterations and a small number of function-gradient evaluations and Hessian vector products per iteration.

The GPCG method starts from an arbitrary initial approximation. At each iteration the inputs of the GPCG method are,

$$\text{Function evaluation: } \frac{1}{2} \{p^{(s)}\}^T [C] \{p^{(s)}\} + \{h\}^T \{p^{(s)}\}$$

$$\text{Gradient evolution: } [C] \{p^{(s)}\} + \{h\}$$

$$\text{Hessian-vector production: } [C] \{p^{(s)}\}$$

Obviously both the CG method and the GPCG method require a number of matrix-vector products. This is the reason why both of these two algorithms are quite time-consuming for larger scale contact problems, where the number of contacting nodes may be as large as 10^3 in CML dynamic simulations.

c) Uniform mesh

If the slider and its projection on the disk surface are discretized with a uniform mesh, the Fast Fourier Transform (FFT) method is usually used to improve the computation speed [37, 38, 39, and 40]. All grids are of the same size for a uniform mesh. Thus the

influence coefficient is only a function of relative position, which means $C_{ij} = C_{ji}$ and $C_{ij} = C(m-k, n-l)$, where (m, n) and (k, l) are the coordinates of node i and node j in the x-y frame shown as Figure 2.5, respectively. The total elastic strain energy is always positive for nonzero pressure distribution, i.e.

$$0 \leq U = \frac{1}{2} \int_{\text{contact region}} p(\bar{u}_{z(s)} + \bar{u}_{z(d)i}) ds = \frac{1}{2} \sum_{i,j \in \text{contact region}} s_i p_i C_{ij} p_j = \frac{1}{2} s \sum_{i,j \in \text{contact region}} p_i C_{ij} p_j,$$

where s is the grid area. This ensures that the influence coefficient matrix is positive definite. So the convergence of the CG method or the GPCG method is guaranteed. Notice that each iteration in the CG or the GPCG method involves a large number of computations of the product of the influence coefficient matrix and a pressure vector. We have the coefficient matrix $C_{ij} = C(m-k, n-l)$, and the pressure element at node j $p_j = p(k, l)$, which can be rewritten as a matrix $[p(k, l)]$ and the slider-disk gap at node i , $h_i = h(m, n)$, which can also be rewritten as a matrix $[h(m, n)]$. Then we have,

$$\sum_i C_{ij} p_j = -h_i \Leftrightarrow \sum_{k,l} C(m-k, n-l) p(k, l) = -h(m, n).$$

The summation of the multiplications on the left hand side of the second equation above has the form of a linear convolution. So the FFT can be used in the computation.

$$\sum_{k,l} C(m-k, n-l) p(k, l) = \text{Inverse FFT}\{\text{FFT}([C]) \bullet \text{FFT}([p])\},$$

where “ \bullet ” is the operation of element -by-element multiplication.

There are two numerical ways for applying the FFT to contact analysis. The general processes are simply sketched here. One way is based on the Continuous Convolution Theorem [38]. First, we use the FFT to transform the pressure vector to the frequency domain. Second, we calculate the influence coefficient matrix directly in the frequency

domain with the Fourier-transformed Papkovitch-Neuber potentials. Third, we multiply each component of the $FFT([p])$ with the influence coefficient matrix at the corresponding frequency. Forth, we compute the inverse FFT to obtain the displacement matrix. The other way is based on the Discrete Convolution Theorem [43]. It is similar to the first way at the first step and the last step. But at the second step it calculates the discrete influence coefficient matrix in the space domain and then uses the discrete FFT to transform the coefficient matrix to the frequency domain. Then at the third step it does an element-by-element multiplication of the matrix $FFT([C])$ and $FFT([p])$. Notice that here the pressure vector $\{p\}$ is not a periodic function. A periodic error occurs if $\{p\}$ is extended periodically for the purpose of computing the FFT. Some techniques have been developed to improve the accuracy of the FFT in contact analysis [39, 40, 43 and 44]. However, all of them require the computational domain to be much larger than the target domain, resulting in a decrease of calculation efficiency.

d) Adaptive mesh

No publication was found that performed contact analysis based on an adaptive mesh. In an adaptive mesh all of the grids are not the same size, which means that C_{ij} depends on the size of the grid at node j as well as the position of node i relative to node j . In this case, $C_{ij} \neq C_{ji}$ and the matrix-vector multiplication cannot be transferred to a convolution form. So the FFT cannot be used to speed up the computation of the matrix-vector multiplication. To make sure that the CG and the GPCG method still converge, we make some changes in the influence coefficient matrix for the CG method and the GPCG method for use with adaptive meshes.

Notice that $[C]\{p\} = -\{h\} \Leftrightarrow [C]^T[C]\{p\} = -[C]^T\{h\}$. So in the CG method we

solve $[C]^T[C]\{p\} = -[C]^T\{h\}$, where $[C]^T[C]$ is a symmetric and positive definite matrix, instead of $[C]\{p\} = -\{h\}$. In fact this is called the CG squared method. Another method, the Bi-conjugate Gradient method, can also be used for the original non-symmetric linear system.

The total complementary energy is,

$$\begin{aligned} V^* &= \frac{1}{2} \sum_{i,j \in \text{contact region}} s_i p_i C_{ij} p_j + \sum_{j \in \text{contact region}} s_i p_i h_i \\ &= \frac{1}{2} \sum_{i,j \in \text{contact region}} \frac{1}{2} (s_i p_i C_{ij} p_j + s_j p_j C_{ji} p_i) + \sum_{j \in \text{contact region}} s_i p_i h_i \\ &= \frac{1}{2} \sum_{i,j \in \text{contact region}} p_i \frac{(s_i C_{ij} + s_j C_{ji})}{2} p_j + \sum_{j \in \text{contact region}} p_i h_i s_i \end{aligned}$$

Let $C'_{ij} = \frac{(s_i C_{ij} + s_j C_{ji})}{2}$, $h'_i = h_i s_i$. Then we have $C'_{ij} = C'_{ji}$, and

$$V^* = \left(\frac{1}{2} \sum_{i,j \in \text{contact region}} p_i C'_{ij} p_j + \sum_{j \in \text{contact region}} p_i h'_i \right)$$

The total elastic strain energy is positive for any nonzero pressure distribution,

$$0 \leq U = \frac{1}{2} \int_{\text{contact region}} p(\bar{u}_{z(s)} + \bar{u}_{z(d)i}) ds = \frac{1}{2} \sum_{i,j \in \text{contact region}} s_i p_i C_{ij} p_j = \frac{1}{2} \sum_{i,j \in \text{contact region}} p_i C'_{ij} p_j.$$

So the matrix $[C'_{ij}]$ is symmetric and positive definite. Thus we can use this $[C'_{ij}]$ instead of $[C_{ij}]$ in the GPCG method.

In the CML air bearing simulation an adaptive grid generation scheme based on the air pressure gradient is used to numerically solve the Reynolds Equation [33]. In this adaptive mesh the grid density is higher at the ABS where the flying height is lower. Those places with lower flying height are more likely to contact the disk. So this adaptive mesh can be used to analyze the slider-disk contact in the slider dynamic simulation. This

avoids introducing a new mesh for the slider dynamic simulation.

2.5.4 Computation Time for the CG Method and the GPCG Method

The computation time of the CG method or the GPCG method is related to the size of the first approximation of the contact regions, i.e. the number of nodes in the geometrical overlap regions. The time consumption versus the node number is plotted in Figure 2.6 for the CG method and the GPCG method using a PC with 1.3 MHz CPU and 256 MB RAM. It is obvious that the GPCG method converges faster than the CG method. The reason is that the GPCG method has a smaller number of iterations and less matrix-vector multiplications per iteration. So we propose to use the GPCG method in the CML dynamic simulation.

2.5.5 Comparison of the Contact Model Based on Influence Coefficients and the Multi-asperity Contact Model by Cha

Cha and Bogy [1] proposed a multi-asperity contact model, which is used in the current CML air bearing simulation program for the slider-disk impact when $d < 0$. This multi-asperity contact model is based on Chang and Ling's elastic-plastic model [9]. This model considers the hysteresis between the loading and unloading process. In the unloading process, only the elastic strain energy is released. In Cha's model each contacting node is a part of a spherical asperity whose radius is calculated through the contact interferences at four nearest neighboring nodes. This model is accurate for Hertzian contact but it may give incorrect results for non-Hertzian contact. Here we do numerical simulations for two cases using this multi-asperity contact model and the new contact model based on influence coefficients. The first case has a flat rigid slider in contact with a spherical asperity on the disk surface, as shown as Figure 2.7(a). The equivalent Young's modulus E^* is 85.29 GPa and the maximum interference is 1.0 nm.

The asperity radius is 2.0 μm . Since the Young's modulus is high and the interference is only on the order of nanometer, the bulk deformation of the disk is negligible. So this case is very close to Hertzian contact. The second case is a rigid slider with a flat pad in contact with a smooth disk, as shown in Figure 2.7(b). This is non-Hertzian contact. The equivalent modulus E^* is 85.29 GPa and the interference is 1.0 nm. Simulation results of the influence coefficient model, Cha's model and the analytical solution are shown in Table 2.2(a) and (b), respectively. It is seen that with more nodes the contact model based on influence coefficients gives a more accurate result. And Cha's model produces a wrong result for non-Hertzian contact.

2.6 Conclusions

The GW model is proved to be the simplest and a sufficiently accurate model for the slider-disk asperity contact, while the KE model can give slightly more accurate results at the cost of computation efficiency. The CEB model, which is used in the current CML air bearing program, in fact can not give accurate contact results for the plasticity index larger than 0.58. When the slider crashes, i.e. the slider-disk gap is less than zero, these asperity-based contact models are no longer valid to model the slider-disk contact, since two of their pre-required assumptions may be violated. The contact model based on influence coefficients can be used for the slider-disk crash contact. The Gradient Projection Conjugate Gradient method is efficient in solving the linear system obtained from that contact model with the adaptive mesh generated by the air pressure gradient. The slider-disk contact may be non-Hertzian due to the ABS design and the arbitrary shape of the slider and disk surface profiles. In this case, Cha's multi-asperity contact model [1] may give an incorrect result for the slider-disk contact. Simulation of the

dynamics of a partial-contact head disk interface uses the analysis of slider-disk contact and impact in this Chapter.

The effect of the pitch and roll angles in slider-disk contact simulations should be considered in the simulation. Pitch and roll are important effects in the slider-disk contact. The total contact force and contact area decrease dramatically as the pitch angle increases from 0 to 200 μrad . Approaches considering only the effect of the area of the contact pad on the total contact force may not be sufficiently accurate.

References

- [1] E. Cha and D. B. Bogy, "Numerical Simulation of Slider Interaction with Multiple Asperity Using Herzian Contact Model," *ASME Jour. of Tribol.*, vol. 117, pp. 575-579, 1995.
- [2] K. Iida and K. Ono, "Design Consideration of Contact/Near-Contact Sliders Based on a Rough Surface Contact Models," *ASME Jour. of Tribol.*, vol. 125, pp. 562-570, 2003.
- [3] Y. Hu, P. M. Jones, P. T. Chang and D. B. Bogy, "Partial Contact Air Bearing Characteristics of Tripad Sliders for Proximity Recording," *ASME Jour. of Tribol.*, vol. 120, pp. 272-279, 1998.
- [4] D. B. Bogy, H. M. Stanley, M. Donovan and E. Cha, "Some Critical Tribological Issues in Contact and Near-Contact Recording," *IEEE Trans. Magn.*, vol. 29, pp. 230-234, 1993.
- [5] K. Ono, Y. Yamamura and T. Mizokoshi, "Computer Analysis of the Dynamic Contact Behavior and Tracking Characteristics of a Single-Degree-of-Freedom Slider Model for a Contact Recording Head," *ASME Jour. of Tribol.*, vol. 117, pp. 124-129,

- 1995.
- [6] J. A. Greenwood and J. B. P. Williamson, "Contact of Nominally Flat Surfaces," *Proc. Roy. Soc. (London)*, vol. A295, pp. 300-319, 1966.
- [7] W. R. Chang, I. Etsion and D. B. Bogy, "An Elastic-Plastic Model for the Contact of Rough Surfaces," *ASME Jour. of Tribol.*, vol. 109, pp. 257-263, 1987.
- [8] L. Kogut and I. Etsion, "A Finite Element Based Elastic-Plastic Model for the Contact of Rough Surfaces," *Trib. Trans.*, vol. 46, pp. 383-390, 2003.
- [9] W. R. Chang and F. F. Ling, "Normal Impact Model of Rough Surfaces," *ASME Jour. of Tribol.*, vol. 114, pp. 439-447, 1992.
- [10] W. Peng, J. Kiely and Y. T. Hsia, "Wear Analysis of Head-Disk Interface During Contact," *ASME Jour. of Tribol.*, vol. 171, pp. 171-179, 2005.
- [11] E. R. Kral and K. Komvopoulos, "Three-Dimensional Finite Element Analysis of Subsurface Stress and Strain Fields Due to Sliding Contact on an Elastic-Plastic Layered Medium," *ASME Jour. of Tribol.*, vol. 119, pp. 332-341, 1997.
- [12] K. Komvopoulos and N. Ye, "Elastic-Plastic Finite Element Analysis for the Head-Disk Interface with Fractal Topography Description," *ASME Jour. of Tribol.*, vol. 124, pp. 775-784, 2002.
- [13] A. Y. Suh and A. A. Polycarpou, "Adhesive Contact Modeling for Sub-5-nm Ultralow Flying Magnetic Storage Head-Disk Interfaces Including Roughness Effects," *Jour. of Applied Physics*, vol. 97, pp. 104328-104338, 2005.
- [14] K. L. Johnson, *Contact Mechanics*, Cambridge University Press, Cambridge, UK, 1985.
- [15] J. A. Greenwood and J. H. Tripp, "The Contact of Two Nominally Flat Rough Surfaces," *Proc. Instn. Mech. Engrs.*, vol. 185, pp. 625-633, 1971.

- [16]E. J. Abbott and F. A. Firestone, "Specifying Surface Quality- a Method Based on Accurate Measurement and Comparison," *Mech. Eng.*, vol. 55, pp. 569-573, 1933.
- [17]D. G. Evseev, B. M. Medvedev and G. G. Grigoriyan, "Modification of the Elastic-Plastic Model for the Contact of Rough Surfaces," *Wear*, vol. 150, pp. 79-88, 1991.
- [18]W. R. Chang, "An Elastic-Plastic Contact Model for a Rough Surface with an Ion-plated Soft Metallic Coating," *Wear*, vol. 212, pp. 229-237, 1997.
- [19]Y. Zhao, D. M. Maietta and L. Chang, "An Asperity Microcontact Model Incorporating the Transition from Elastic Deformation to Fully Plastic Flow," *ASME Jour. of Tribol.*, vol. 122, pp. 86-93, 2000.
- [20]J. I. McCool, "Predicting Microfracture in Ceramics via a Micro-contact Model," *ASME Jour. of Tribol.*, vol. 108, pp. 380-386, 1986.
- [21]J. H. Horng, "An Elastic-plastic Microcontact Model for rough surfaces," *ASME Jour. of Tribol.*, vol. 120, pp. 82-88, 1998.
- [22]L. Kogut and I. Etsion, "The Contact of a Compliant Curved and a Nominally Flat Rough Surfaces," *Trib. Trans.*, vol. 43, pp. 507-513, 2000.
- [23]N. Yu and A. A. Polycarpou, "Contact of Rough Surfaces with Asymmetric Distribution of Asperity Heights," *ASME Jour. of Tribol.*, vol. 124, pp. 367-376, 2002.
- [24]R. L. Jackson and I. Green, "A Statistical Model of Elasto-plastic Asperity Contact of Rough Surfaces," *Proceedings of 2003 STLE/ASME Joint International Tribology Conference*, 2003.
- [25]J. I. McCool, "Relating Profile Instrument Measurements to the Functional Performance of Rough Surfaces," *Trans. of the ASME*, pp. 264-270, 1987.

- [26] P. R. Nayak, "Random Process Model of Rough Surface," *Jour. of Lubric. Tech.*, vol. 93(3), pp. 398-407, 1973.
- [27] R. S. Sayles and T. R. Thomas, "Surface Topography as a Nonstationary Random Process," *Nature*, vol. 271, pp. 431-434, 1978.
- [28] A. Majumdar and B. Bhushan, "Role of Fractal Geometry in Roughness Characterization and Contact Mechanics of Surfaces," *ASME Jour. of Tribol.*, vol. 112, pp. 205-216, 1990.
- [29] A. Majumdar and B. Bhushan, "Fractal Model of Elastic-Plastic Contact between Rough Surfaces," *ASME Jour. of Tribol.*, vol. 113, pp. 1-11, 1991.
- [30] W. Yan and K. Komvopoulos, "Contact Analysis of Elastic-plastic Fractal Surfaces," *Jour. of Applied Physics*, vol. 84, pp. 3617-3624, 1998.
- [31] J. C. Chung and J. F. Lin, "Fractal Model Developed for Elliptical Elastic-Plastic Asperity Microcontacts of Rough Surfaces," *ASME Jour. of Tribol.*, vol. 126, pp. 646-654, 2004.
- [32] W. H. Press, S. A. Teukolsky, W. T. Wetterling and B. P. Flannery, *Numerical Recipes in FORTRAN, the Art of Scientific Computing*, 2nd ed., Cambridge University Press, Cambridge, UK, 1999.
- [33] S. Lu, "Numerical Simulation of Slider Air Bearings," Ph.D. Thesis, University of California at Berkeley, 1997.
- [34] Y. Zhao and L. Chang, "A Model of Asperity Interactions in Elastic-Plastic Contact of Rough Surfaces," *ASME Jour. of Tribol.*, vol. 123, pp. 857-864, 2001.
- [35] Love, A. E. H., "Stress Produced in a Semi-Infinite Solid by Pressure on Part of the Boundary," *Proc. Roy. Soc. (London)*, vol. A228, pp. 377-420, 1929.
- [36] F. H. Shi and Q. Wang, "A Method of Influence Functions for Thermal Analyses of

- Tribological Elements,” *Tribol. Trans.*, vol. 41, pp. 350–358, 1998.
- [37] T. C. O’Sullivan and R. B. King, “Sliding Contact Stress Field Due to a Spherical Indenter on a Layered Elastic Medium,” *ASME Jour. of Tribol.*, vol. 110, pp. 235-240, 1988.
- [38] T. Nogi and T. Kato, “Influence of a Hard Surface Layer on the Limit of Elastic Contact; Part I- Analysis Using a Real Surface Model,” *ASME Jour. of Tribol.*, vol. 119, pp. 493-500, 1997.
- [39] X. L. Ai and K. Sawamiphakdi, “Solving Elastic Contact Between Rough Surfaces as an Unconstrained Strain Energy Minimization by Using CGM and FFT Techniques,” *ASME Jour. of Tribol.*, vol. 120, pp. 668-676, 1991.
- [40] I. A. Polonsky and L. M. Keer, “A Fast and Accurate Method for Numerical Analysis of Elastic Layered Contacts,” *ASME Jour. of Tribol.*, vol. 121, pp. 668-679, 2000.
- [41] J. J. Kalker, “Variational Principles of Contact Elastostatics,” *Jour. Inst. Math. & Appl.*, vol. 20, pp. 199-219, 1977.
- [42] J. J. More and G. Toraldo, “On the Solution of Large Quadratic Programming Problems with Bound Constraints,” *SIAM Jour. of Optimization*, vol. 1, pp. 93–113, 1991.
- [43] S. B. Liu, Q. Wang and G. Liu, “A Versatile Method of Discrete Convolution and FFT (DC-FFT) for Contact Analysis,” *Wear*, vol. 243, pp. 101-110, 2000.
- [44] S. B. Liu and Q. Wang, “Studying Contact Stress Fields Caused by Surface Traction with a Discrete Convolution and Fast Fourier Transform Algorithm,” *ASME Jour. of Tribol.*, vol. 124, pp. 36-45, 2002.

Table 2.1 Slider and disk roughness and material parameters

Individual Surfaces	Disk 1	Disk 2	Disk 3	Slider
σ (nm)	1.486	1.066	0.123	0.643
R (μm)	3.765	8.431	14.204	7.147
η (μm^{-2})	7.071	5.683	18.163	8.849
Combined surfaces	Case 1: Slider/Disk 1	Case 2: Slider/Disk 2	Case 3: Slider/Disk 3	
σ (nm)	1.619	1.245	0.654	
R (μm)	3.331	5.452	6.384	
η (μm^{-2})	7.393	7.177	9.871	
σ_s (nm)	1.417	1.143	0.578	
y_s (nm)	1.866	1.174	0.729	
ψ	0.836	0.587	0.386	
Material Properties				
ν_d and ν_s	0.20, 0.21			
E_d and E_s (Gpa)	100, 450			
E (Gpa)	85.29			
H (Gpa)	2.5			

Table 2.2 Numerical results for two cases of slider-disk contact shown in Figure 2.7

a)

	Contact force (N)	Contact area (m^2)
Model based on influence coefficients with 9 nodes	5.277×10^{-6}	7.177×10^{-15}
Model based on influence coefficients with 261 nodes	5.097×10^{-6}	6.482×10^{-15}
Cha's contact model [7]	5.086×10^{-6}	6.283×10^{-15}
Analytical solution	5.086×10^{-6}	6.283×10^{-15}

b)

	Contact force (N)	Contact area (m^2)
Model based on influence coefficients with 9 nodes	3.010×10^{-4}	1.118×10^{-11}
Model based on influence coefficients with 261 nodes	3.291×10^{-4}	1.217×10^{-11}
Cha's contact model [7]	0.0	0.0
Analytical solution	3.412×10^{-4}	1.257×10^{-11}

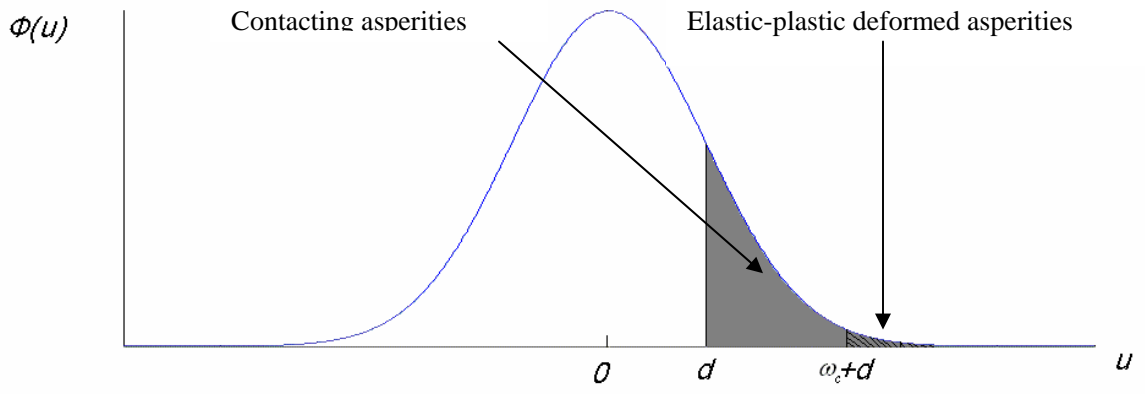


Fig.2.1. Density function of Gaussian distributed asperity height u .

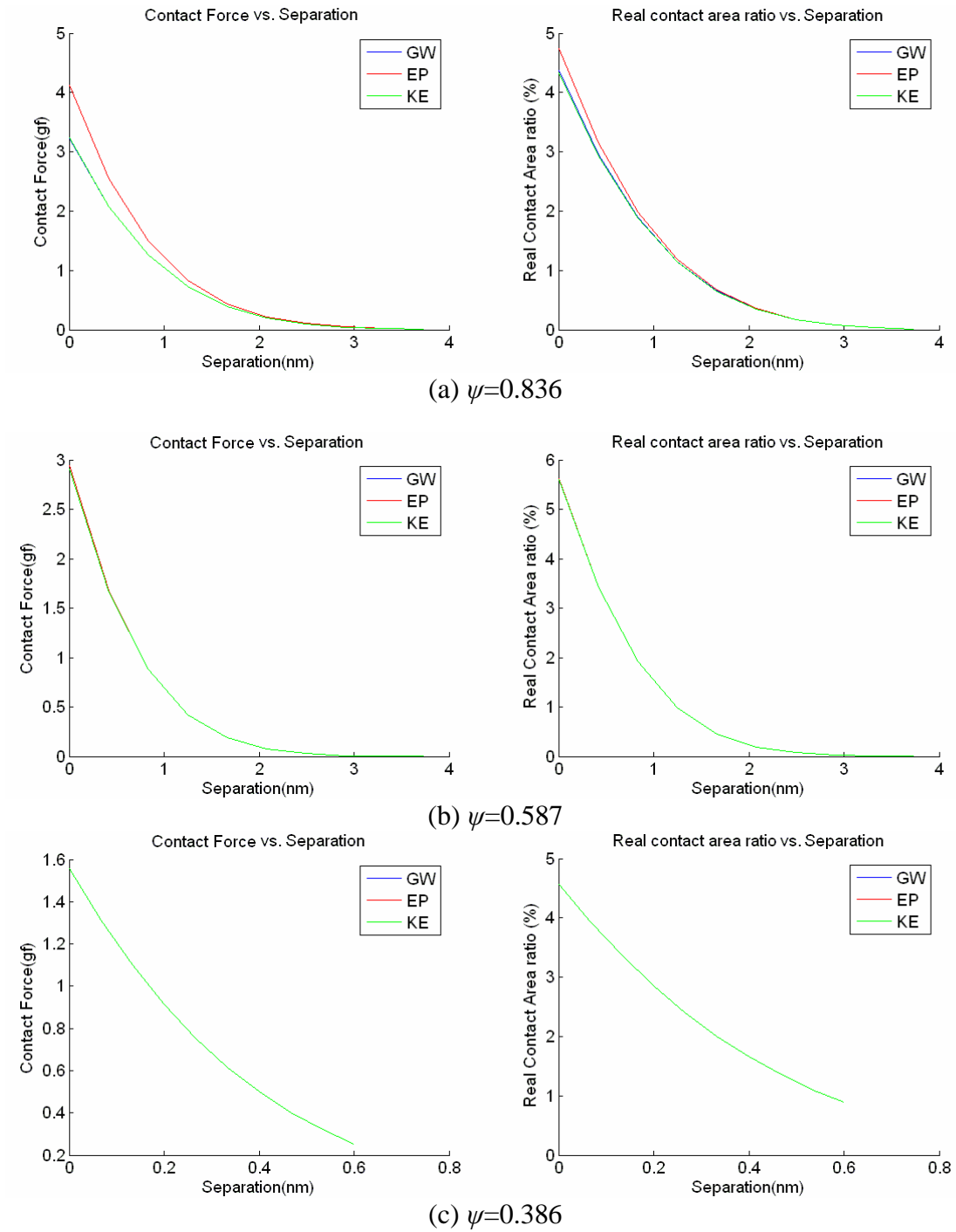


Fig.2.2. Contact force versus separation and real contact area ratio versus separation for three cases with GW, CEB (i.e., EP) and KE model with plasticity index ψ equal to 0.836, 0.587 and 0.386, respectively.

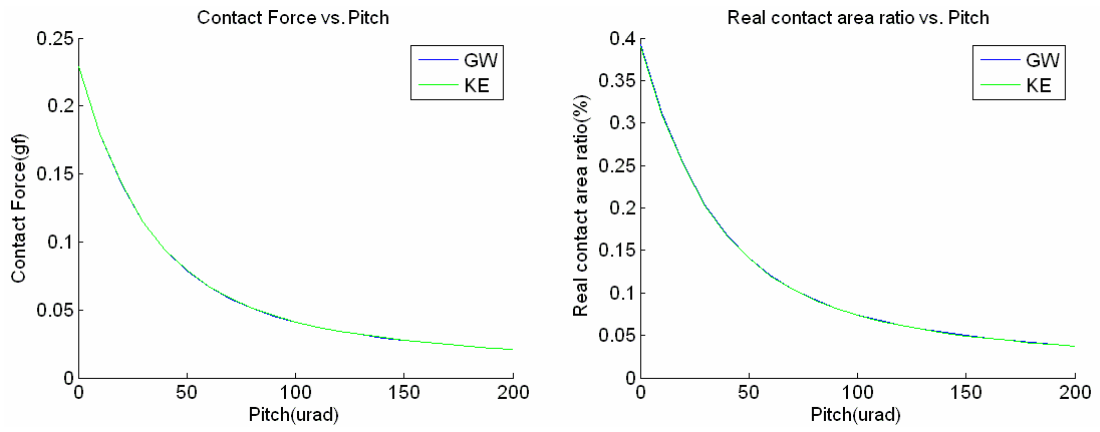
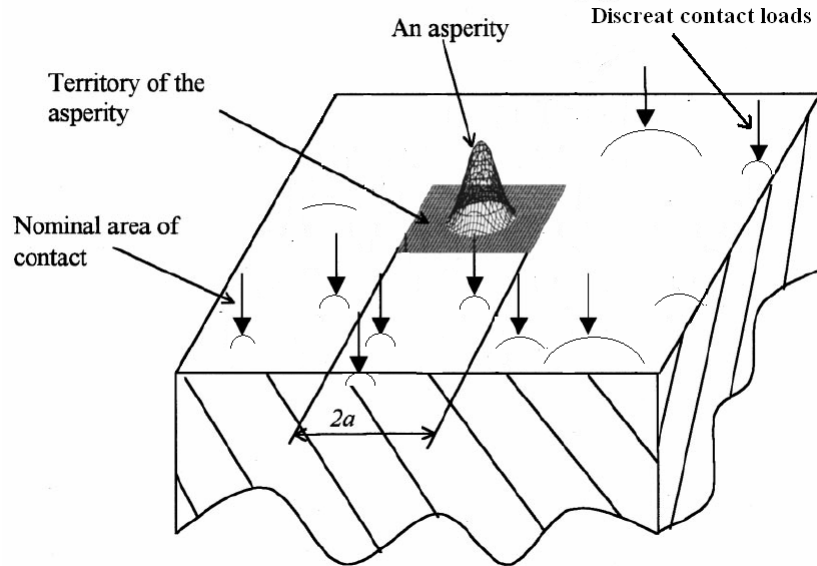
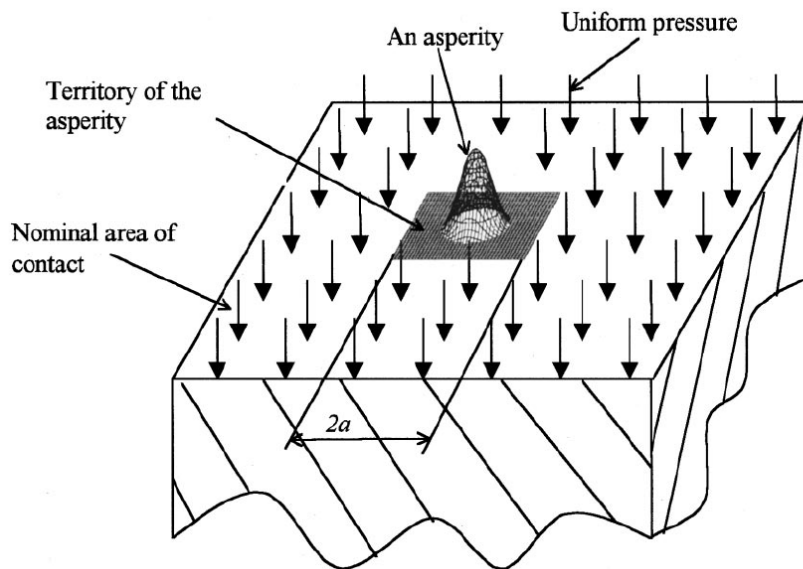


Fig.2.3. Contact force and real contact area versus pitch angles for GW and KE model.



(a) Deformation at a given asperity caused by pressures on all other contacting asperities



(b) Deformation at a given asperity due to an equivalent uniform pressure applied over the surface area outside the territory of the asperity [34]

Fig.2.4. Two different contact cases that can not be related through Saint-Venant's Principle.

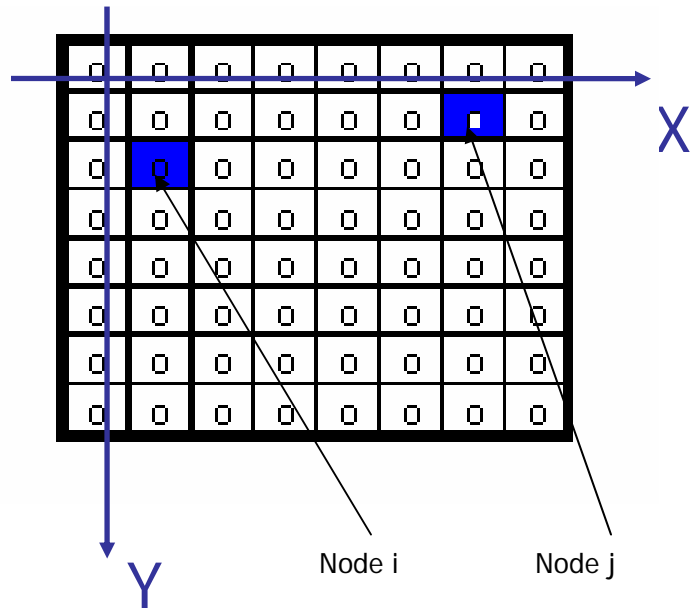


Fig.2.5. Demonstration of two nodes on meshed slider air bearing surface.

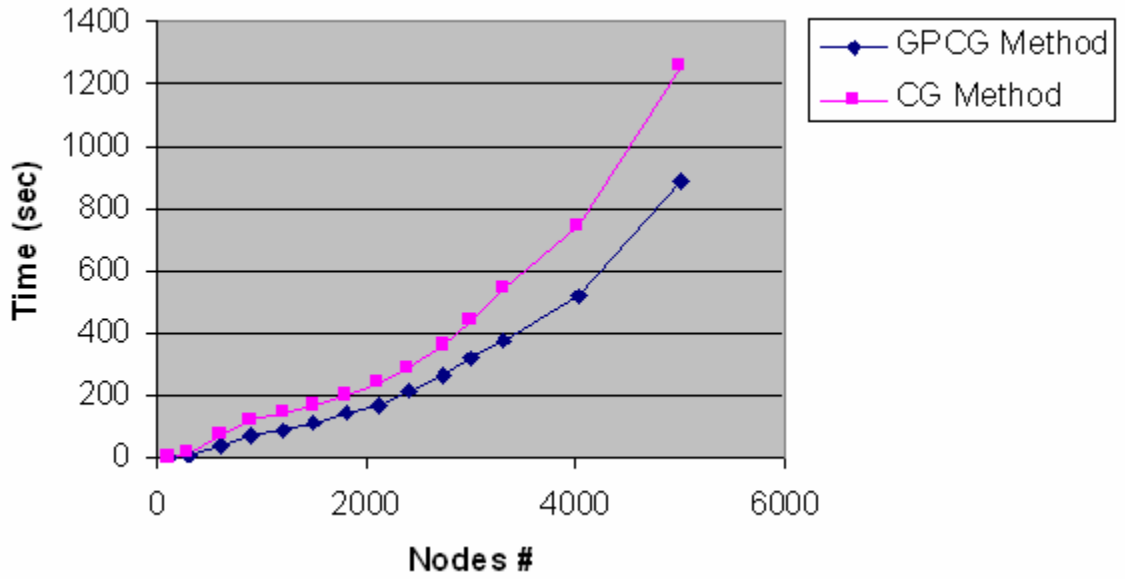


Fig.2.6. Time consumption of CG method and GPCG method on a computer with a Intel Pentium Mobile 1.3GHz processor.

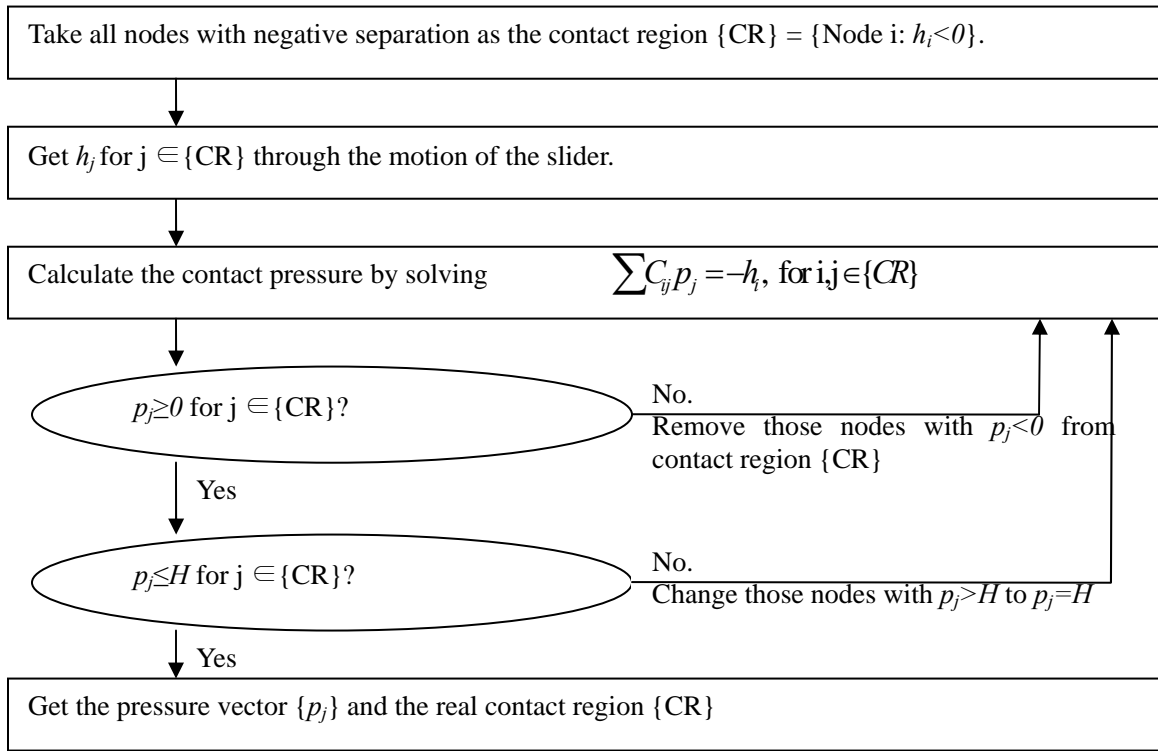


(a) A flat rigid slider in contact with a spherical asperity on the disk surface

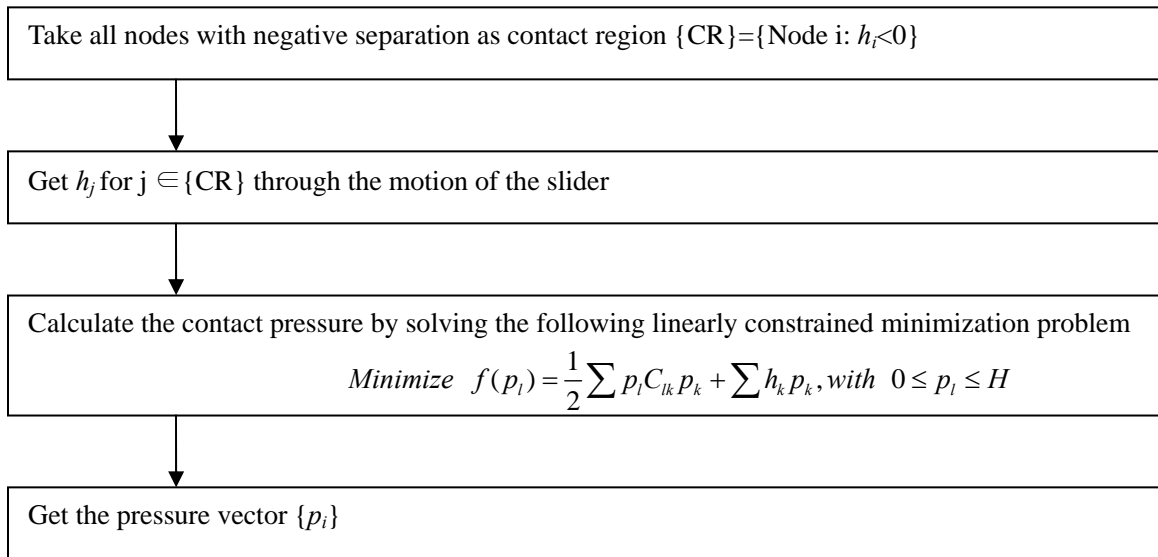


(b) A rigid slider with a flat pad in contact with a smooth disk

Fig.2.7. Two slider-disk contact cases.



(a) CG method



(b) GPCG method

Fig.2.8. Algorithms of two numerical schemes for contact analysis with the influent coefficient model.

Chapter 3 Intermolecular Adhesion between an Air Bearing Slider in Contact or Near Contact Regime and a Disk

When the minimum spacing between the slider and the disk is less than 5 nm, the intermolecular adhesion between the two solid surfaces can no longer be assumed to be zero. The model proposed by Wu and Bogy [1] can be viewed as a flat slider-disk intermolecular force model. A large repulsion between the slider and the disk is predicted in this model when the slider-disk spacing is in the contact regime. For accurate analysis of the intermolecular force effect on the head disk interface, we need to consider the slider and disk surface roughnesses when the flying height is comparable to the surface roughness root-mean-square value or when the slider-disk contact occurs. With the intermolecular force model and asperity roughness model implemented in the CML air bearing program, we analyze the effect of the intermolecular adhesion on the slider at an ultra-low flying height in static flying simulations. It is found that the intermolecular adhesion between the slider and the disk has a slight effect on the slider-disk interface for a flying slider.

3.1 Introduction

The effect of intermolecular adhesion on air bearing sliders in hard disk drives has been extensively investigated recently, starting with the paper by Wu and Bogy [1]. The intermolecular force between the slider and the disk is usually modeled based on the

Leonard-Jones potential, which describes the potential energy between two atoms as a function of the distance between their centers. In the implementation of this potential in a closely spaced slider-disk interface the force is expressed as a function of the distance between the slider and the disk, i.e. the local flying height (FH). However, when the FH is less than 3 nm, a contact distance ε (0.3-0.5 nm) needs to be considered and the intermolecular force then turns out to be a function of $FH + \varepsilon$. Hence for a very close spacing the intermolecular force is overestimated in Wu and Bogy [1], and others. With this modification, there occurs no unbounded repulsive intermolecular stress when the FH is less than 0.5 nm, or down to contact.

The model resulting from this modification can be viewed as a flat slider-disk intermolecular force model. In order to get more accurate analysis of the intermolecular adhesion effect on the head disk interface, the slider and disk surface roughnesses need to be considered when the flying height is comparable to the surface roughness root-mean-square (RMS) value or when the slider-disk contact occurs. The improved DMT (IDMT) models [2, 3 and 4], which are suitable for small, stiff spherical asperities, can be used to approximate the rough slider-disk intermolecular adhesion force. The intermolecular adhesion between measured rough slider and disk surfaces is calculated using the IDMT models, and the results are compared with the intermolecular force between the corresponding flat slider and disk surfaces. With this improvement implemented in the CML air bearing program, the effect of adhesion on the slider at low flying heights is analyzed in static flying simulations.

3.2 Intermolecular Adhesion Force Model

As a special case of the Mie Potential, the Lennard-Jones potential is widely used to

describe the interaction between two atoms or molecules. It is expressed as,

$$w(r) = -C/r^6 + D/r^{12}, \quad (1)$$

where r is the center-to-center distance between the atoms and C and D are constants. For two atoms in vacuum the values $C=10^{-77}\text{J}\cdot\text{m}^6$ and $D=10^{-134}\text{J}\cdot\text{m}^{12}$ are usually adopted [1]. Differentiating the Lennard-Jones potential with respect to the distance r , we obtain the Lennard-Jones force as,

$$f = \frac{dw}{dr} = \frac{6C}{r^7} - \frac{12D}{r^{13}}, \quad (2)$$

where the direction of adhesion is chosen as the positive direction of the force.

If we ignore the anisotropy, non-additivity, and retardation effects of the Lennard-Jones potential, and make the continuum assumption, we get through appropriate integration the potential between an infinite-half space and a unit area of a parallel infinite half space, as shown in Figure 3.1,

$$U = \rho_2 \int_h^\infty \left(-\frac{\pi C \rho_1}{6z^3} + \frac{\pi D \rho_1}{45z^9} \right) dz, \quad (3)$$

where ρ_1 and ρ_2 , respectively, are the number densities of atoms or molecules in these two infinite half spaces and h is the distance between the two center planes of the surface atoms or molecules. If we differentiate this potential with respect to the distance h , we get the intermolecular adhesion stress between two half spaces,

$$P(h) = \frac{dU}{dh} = \frac{A}{6\pi} \frac{1}{h^3} - \frac{B}{45\pi} \frac{1}{h^9}, \quad (4)$$

where the Hamaker constant $A = \pi^2 C \rho_1 \rho_2$ and another constant $B = \pi^2 D \rho_1 \rho_2$. This result is similar to the intermolecular force expression obtained by Wu and Bogoy [1] except that here h is the center-plane-to-center-plane distance instead of the local FH. We assume

that the surfaces of the two half spaces are in contact when the total potential energy is a minimum [5]. If the minimum potential is at the distance $h=\varepsilon$, then the flying height is equal to $h - \varepsilon$. We see that $P(h=\varepsilon)=0$ when the potential is minimal. Then, using Equation (4) we find

$$\varepsilon = \left(\frac{2B}{15A}\right)^{1/6}. \quad (5)$$

So Equation (4) can be written as,

$$P(h) = \frac{A}{6\pi\varepsilon^3} \left[\left(\frac{\varepsilon}{h}\right)^3 - \left(\frac{\varepsilon}{h}\right)^9 \right]. \quad (6)$$

If we take the difference in surface energy before and after contact as the required energy to separate the two contacting surfaces against the intermolecular adhesion, then we have

$$\Delta\gamma = \gamma_1 + \gamma_2 - \gamma_{12} = \int_{\varepsilon}^{\infty} P(h)dh = \frac{A}{16\pi\varepsilon^2}, \quad (7)$$

where γ_1 and γ_2 are the surface energies of the two surfaces before contact, and γ_{12} is the surface energy of their interface at contact.

The contact distance ε between two half-spaces was suggested to be 0.3-0.5 nm [2, 3, and 4]. Recently Yu and Polycarpou [6] re-calculated ε using the relationship between the ground-state property of a given crystal and its intermolecular potential, which is dominated by the nearest neighbors. This approach is valid for molecular crystals, in which the total energy is primarily the sum of all interaction potentials between the molecules. The weak intermolecular interaction can be approximated by the Lennard-Jones potential. However, for covalent crystals, such as diamond and metals, the inter-atomic bonds are covalent bonds or metallic bonds, which cannot be described by the Lennard-Jones potential [7]. Another issue is the incompatibility between the

continuum approach and the molecular approach with the nearest neighbor assumption. The continuum approach considers the interaction between one atom or molecule and those non-nearest neighbors. So if we use the molecular approach and assume that only the nearest neighbors contribute the interaction energy, the obtained results can not be applied to the continuum approach.

It is approximated that $\Delta\gamma = \gamma_1 + \gamma_2 - \gamma_{12} \approx 2\gamma$ for two surfaces composed of the same material, where γ is their surface energy. Hence for two diamond-like carbon (DLC) surfaces, we know the surface energy $\gamma \approx 0.04 J/m^2$ [8] and the Hamaker constant $A = 1.80 \times 10^{-19} J$ [9], then we can estimate the contact distance ε for DLC surfaces through Equation (7). This estimation gives $\varepsilon \approx 0.22$ nm. So it is reasonable to take $\varepsilon \approx 0.3$ nm.

If we take $\varepsilon \approx 0.3$ nm, then the FH can not be approximated by h when it is comparable to ε . Figure 3.2 shows the adhesion stresses with $FH=h$ and $FH=h-\varepsilon$. When $FH=0$, i.e. $h=\varepsilon$, the two surfaces are in contact, and the contact force can be obtained through contact mechanics. When the contact distance ε is considered, we will not have the result that an infinite repulsion will occur between the slider and disk when the flying height approaches zero. This is reasonable since the slider may contact the disk and even crash on the disk.

3.3 Improved DMT Model for Asperity Adhesion

If we also consider the surface roughness we cannot use the above simple integration method to calculate the total potential and adhesion stress between two surfaces. We need to turn to other asperity-based adhesion models. For a single asperity contact, Derjaguin et al. [5] proposed the IDMT model, which assumes that the adhesion is the sum of all the

intermolecular interactions outside the contact zone, and that there is no contribution from the contact area. Another, somewhat opposite model, called the JKR model [10], assumes that the adhesion is confined to the contact region. As pointed out by Tabor [11], these two models work under different conditions, which are determined by the adhesion parameter λ ,

$$\lambda = \left(\frac{R\Delta\gamma^2}{E^2\epsilon^3} \right)^{1/3}, \quad (8)$$

where E is the equivalent Young's modulus and R is the radius of curvature of the asperity. It is shown that small values of λ ($\lambda < 1$) correspond to a regime where the DMT model applies and large values of λ correspond to the JKR regime. The Maugis model [12], which used the Dugdale approximation [13] to the Lennard-Jones force, can be viewed as a bridge between the IDMT and JKR models, and it applies to a wide range of adhesion parameters. For a slider-disk interface, R is on the order of $10^1 \mu\text{m}$, E is on the order of 10^1 GPa and $\Delta\gamma$ is on the order of 10^{-2} J/m^2 , then though Equation (8) we determine that λ is approximately 0.15, which is much less than 1. So we can use the DMT model for the adhesion problem in the slider-disk interface. Of course here we have made the assumption that the adhesion between the slider and disk is quasi-static.

The contact between two rough surfaces can be modeled by an equivalent single rough surface contacting a flat rigid plane. Some of the asperities on the equivalent rough surface are in contact with the flat surface, while others are not in contact. So we need to use the IDMT model [4] to consider the adhesion between those non-contacting asperities and the flat surface as well as the adhesion due to contacting asperities. Since the IDMT model only uses the Hertz profile of an elastically deformed asperity for all contacting asperities, Chang et al. [2] proposed a CEB-IDMT model with the profile obtained

through the volume conservation theory for plastic contact; Kogut and Etsion [3] developed the KE-IDMT model with the asperity profile from the finite element method (FEM) solution. The difference between the CEB-IDMT model and KE-IDMT model, numerically shown in [3], partially comes from the inaccuracy of Equation (19a) in [3], which occurs when the dimensionless interference is less than 0.1. Here we directly use Equation (15) in [3] for the KE-IDMT model.

We use the equivalent slider and disk surface parameters as given in [14], shown in Table 3.1, and calculate the adhesion stresses based on these three adhesion models, i.e. IDMT, CEB-IDMT and KE-IDMT. The results are shown in Figure 3.3. Here the local FH is defined as the distance between the mean asperity surfaces of the slider and the disk, while the local FH between an ideally flat slider and flat disk is just the distance between them. Obviously the local FH is a function of position. It is found that the difference predicted by those various adhesion models is very small for low values of the plasticity index, which characterizes the elastic-plastic deformation of asperities. Asperities are mostly elastically deformed in the contact interfaces with the smaller plasticity index. If we compare the adhesion stress obtained using the IDMT model with that obtained using the intermolecular force model, i.e. the result shown in Figure 3.2 with that in Figure 3.3, we find that the IDMT models give much a smaller adhesion stress than the intermolecular force model.

3.4 Net Adhesion Stress

The net adhesion stress on the slider is the asperity adhesion stress minus the asperity contact pressure. Asperity contacts occur when the distance between the slider and the disk is below the glide height. In the simulations we can take three times the standard

deviation of the disk surface height as the glide height. The asperity contact pressure increases as the distance between the slider and disk surfaces decreases towards zero.

To model the slider-disk asperity contact we assume that all of the contacts are quasi-static. For the multi-asperity static contact between two parallel surfaces, the GW model [15], CEB model [16] and KE model [17] give different relationships between the contact pressure and the distance between two parallel surfaces, as described in Chapter 2. The GW model assumes that all of the contacting asperities are elastically deformed. The CEB model assumes that the contacting asperities are either elastically deformed when the interference is less than a critical value, or directly become fully plastically deformed when the interference is greater than the critical interference. In the KE model the elastic-plastic deformation of a single contacting asperity is analyzed using the FEM. Although the results of these three models are different, the difference is negligible when the plasticity index of the contact interface is small and only a few of the contacting asperities are fully plastically deformed. Figure 3.4 shows the contact pressures versus FH for the slider and the disk, using the surface parameters in Table 3.1. The results of these three models are close to each other for these three contact interfaces, except that the CEB model gives slightly larger contact pressure than the others when the plasticity index is 0.836. The reason is that the total contact force of a fully plastically deformed asperity is much larger than for an elastically or elastic-plastically deformed asperity. So the assumption of the CEB model is expected to predict a larger contact pressure.

Figure 3.5 shows the net adhesion stress for these three slider-disk interfaces for the three models versus the flying height. The net adhesion stress in Figure 3.5 is much smaller than the intermolecular adhesion stress shown in Figure 3.2. Also, for the rougher slider-disk interface the net adhesion stress can become negative at a low flying height,

which means a repulsion effect instead of adhesion effect on the slider.

3.5 Static Simulation of an Air Bearing Slider

The adhesion stress calculation needs to be implemented in the air bearing simulation, in order to analyze the effect of the intermolecular adhesion on the slider. We can not make a simple conclusion that the effect of adhesion is negligible when the FH is above 3 nm simply because in Figure 3.2 or Figure 3.5 the adhesion stress is close to zero when the flying height is above 3 nm. The reason is that the adhesion stress may still be comparable to the air bearing pressure although it looks very small in Figure 3.2 or Figure 3.3 for a FH greater than 3 nm. In addition, different regions on the slider have different flying heights, due to the pitch, roll and the air bearing surface (ABS) design features of the slider, and hence they have different adhesion pressures. The correct way to analyze the effect of adhesion is to consider the adhesion stress in the slider flying simulations. As shown above, the choices among these asperity contact and adhesion models do not make much difference for the flying slider/disk interface. So we picked the KE-IDMT adhesion and KE contact models in the following slider static simulations.

The CML air bearing static simulation program is used in the simulations. In this program the generalized Reynolds equation is modified by the Fukui-Kaneko slip correction [18] to account for the rarefaction of the air at the slider/disk spacing down to asperity contact. The modified Reynolds equation is then discretized using Patankar's control volume method, and the final discretization equations are solved using the alternating direction line sweep method combined with the full multi-grid algorithm. The ABS is discretized to small grids, which are approximately parallel to the disk surface with various flying heights. Then the intermolecular force model or asperity

adhesion/contact models are applied to each grid. Air bearing shear stress on the ABS is also considered in the simulation program and its effects on the pitch and roll of the slider have been analyzed previously [19]. The effect of the slider-disk asperity contact on the air bearing pressure is not considered due to the negligible real contact area as compared with the air bearing surface. In addition, the surface roughness effects are not included in the air bearing model. For a given ABS design the static simulation program uses the quasi-Newton method to calculate the slider's static flying altitude, i.e., the equilibrium state.

In the simulation we use a CML designed femto slider with the ABS shown in Figure 3.6. Three cases are simulated, including the slider-disk interfaces with two types of surface roughness parameters, case 2 and case 3 in Table 3.1, and a flat slider/disk interface. The asperity adhesion/contact models are applied to the first two cases and the last one uses the intermolecular force models. Figure 3.7 shows the relationship between the disk revolutions per minute (RPM) and the slider's minimum flying height for these cases. As the disk RPM decreases, the slider's minimum flying height also decreases. Both the original and modified intermolecular force models show significant flying height decreases due to the intermolecular adhesion stress. At the same disk RPM the minimum flying height obtained using the modified intermolecular force model is higher than that obtained using the original intermolecular force model. This can be explained by the smaller adhesion stress calculated with the consideration of the contact distance in the modified intermolecular force model. However, the rougher and smoother slider disk interfaces using the asperity adhesion/contact model show less effect of adhesion. The minimum flying heights are close to that obtained without considering the slider-disk adhesion, when they are above the glide height, i.e., 3 times the standard deviation of the

surface height. When the minimum flying height is below the glide height, the rougher slider-disk interface, i.e. case 2 in Table 3.1, has a higher minimum flying height than in the case without considering slider-disk adhesion or contact, while the smoother slider-disk interface, i.e. case 3 in Table 3.1, shows the opposite trend. This indicates that the net adhesion stress takes effect only when the minimum flying height is less than the glide height. For the rougher slider-disk interfaces, the net adhesion stress becomes negative at a flying height below the glide height. Hence the slider has a higher minimum flying height. On the other hand, for the smoother slider-disk interface the net adhesion stress is positive, and it increases as the flying height decreases, so the slider has a lower flying height.

In Figure 3.7 we also see that the modified intermolecular force model produces two minimum flying heights for one low value of disk RPM, as does the original intermolecular force model. The smaller of the two flying heights corresponds to an unstable equilibrium [20]. However, this unstable equilibrium has not been found in experiments. On the other hand, the asperity contact/adhesion models do not produce such an unstable flying height, and therefore they agree better with experimental results, which is reasonable since practical slider and disk surfaces always have certain roughnesses.

3.6 Conclusions

In this chapter we investigate the intermolecular force model and asperity adhesion/contact models for ultra-low flying height sliders. A contact distance is introduced and included in the original intermolecular force model, after which it is found that no infinite repulsive force occurs as the flying height approaches zero. The IDMT

model and GW models are recommended for multi-asperity adhesion and contact simulations, respectively. Other improved models have negligible difference for the slider-disk interface, which has a low plasticity index, high hardness and Young's modulus. Asperity adhesion/contact models are implemented in the CML static air bearing simulation program and the following conclusions may be drawn from the simulations,

1. The intermolecular force model overestimates the slider disk adhesion due to the neglect of the roughness of the slider and disk surfaces.
2. For practical slider and disk surfaces with certain roughnesses, the effect of asperity adhesion/contact is negligible when the minimal flying height is above the glide height.
3. The modified intermolecular force model that incorporates the contact distance predicts a smaller reduction in flying height than the original intermolecular force model. The effect is further reduced when surface roughness is included.
4. When the slider and disk roughness is considered, the slider static simulation does not obtain an unstable equilibrium at low disk RPM.
5. When the slider's minimum flying height is less than the glide height, the minimum flying height is higher on rougher slider/disk interfaces since the net adhesion stress is smaller and may even become negative for rougher interfaces.

References

- [1] L. Wu and D. B. Bogy, "Effect of the Intermolecular Forces on the Flying Attitude of Sub-5 nm Flying Height Air Bearing Sliders in Hard Disk Drives," *ASME Jour. of Tribol.*, vol. 124, pp. 562-567, 2002.
- [2] W. R. Chang, I. Etsion and D. B. Bogy, "Adhesion Model for Metallic Rough

- Surface,” *ASME Jour. of Tribol.*, vol. 110, pp. 50-56, 1988.
- [3] L. Kogut and I. Etsion, “Adhesion in Elastic–Plastic Spherical Microcontact,” *Jour. of Colloid and Interface Sci.*, vol. 261, pp. 372-378, 2003.
- [4] V. M. Muller, B. V. Derjaguin and V. P. Toporov, “On Two Methods of Calculation of the Force of Sticking of an Elastic Sphere to a Rigid Plane,” *Colloid and Surfaces*, vol. 7, pp. 251-259, 1983.
- [5] B. V. Derjaguin, V. M. Muller and Y. P. Toporov, “Effect of Contact Deformations on the Adhesion of Particles,” *Jour. of Colloid and Interface Sci.*, vol. 53, pp. 314-326, 1975.
- [6] N. Yu and A. A. Polycarpou, “Adhesive Contact Based on the Lennard-Jones Potential: a Correction to the Value of the Equilibrium Distance as Used in the Potential,” *Jour. of Colloid and Interface Sci.*, vol. 278, pp. 428-35, 2004.
- [7] J. N. Israelachvili, *Intermolecular and Surface Forces*, second edition, Academic Press, San Diego, 1992.
- [8] L. Y. Ostrovskaya, “Studies of Diamond and Diamond-Like Film Surfaces Using XAES, AFM and Wetting,” *Vacuum*, vol. 68, pp. 219-38, 2003.
- [9] B. Zhang and A. Nakajima, “Possibility of Surface Force Effect in Slider Air Bearings of 100 Gbit/in² Hard Disks,” *Tribol. Int.*, vol. 36, pp. 291-296, 2003.
- [10] K. L. Johnson, K. Kendall and A. D. Roberts, “Surface Energy and the Contact of Elastic Solids,” *Proc. Roy. Soc. (London)*, vol. A324, pp. 301-313, 1971.
- [11] D. Tabor, “Surface Forces and Surface Interactions,” *Jour. of Colloid and Interface Sci.*, vol. 58, pp. 1-13, 1977.
- [12] D. Maugis, “The JKR-DMT Transition Using a Dugdale Model,” *Jour. of Colloid Interface Sci.*, vol. 150, pp. 243-269, 1992.

- [13]D. S. Dugdale, “Yielding in Steel Sheets Containing Slits,” *Jour. of Mech. Phys. Solids*, vol. 8, pp. 100–104, 1960.
- [14]A. Y. Suh and A. A. Polycarpou, “Adhesive Contact Modeling for Sub-5-nm Ultralow Flying Magnetic Storage Head-Disk Interfaces Including Roughness Effects,” *Jour. Applied Physics*, vol. 97, pp. 104328-104338, 2005.
- [15]J. A. Greenwood and J. B. P. Williamson, “Contact of Nominally Flat Surfaces,” *Proc. R. Soc. London*, vol. A295, pp. 300-319, 1966.
- [16]W. R. Chang, I. Etsion and D. B. Bogy, “An Elastic-Plastic Model for the Contact of Rough Surfaces,” *ASME Jour. of Tribol.*, vol. 109, pp. 257-263, 1987.
- [17]L. Kogut and I. Etsion, “A Finite Element Based Elastic-Plastic Model for the Contact of Rough Surfaces,” *Trib. Trans.*, vol. 46, pp. 383-390, 2003.
- [18] S. Fukui and R. Kaneko, “Analysis of Ultra-Thin Gas Film Lubrication Based on Linearized Boltzmann Equation: First Report-Derivation of a Generalized Lubrication Equation Including Thermal Creep Flow,” *ASME J. Tribol.*, vol. 110, pp. 253–262., 1988.
- [19]D. Chen and D. B. Bogy, “A Comparison of Two Rarefaction Models in the Compressible Reynolds Equation Used in Air Bearing Design for Hard Disk Drives,” Technical Report No. 2005-010, Computer Mechanics Lab, Department of Mechanical Engineering, University of California, Berkeley, 2005.
- [20]V. Gupta and D. B. Bogy, “Effect of Intermolecular Forces on the Static and Dynamic Performance of Air Bearing Sliders: Part I—Effect of Initial Excitations and Slider Form Factor on the Stability,” *ASME Jour. of Tribol.*, vol. 128, pp. 197-202, 2006.

Table 3.1 Slider/disk equivalent roughness parameters

Equivalent roughness parameter	Case 1 (slider/disk 1)	Case 2 (slider/disk 2)	Case 3 (slider/disk 3)
Standard deviation of surface height (nm)	1.619	1.245	0.654
Asperity radius (μm)	3.331	5.452	6.384
Asperity density (μm^{-2})	7.393	7.177	9.871
Standard deviation of asperity height (nm)	1.417	1.143	0.578
Plasticity index Ψ	0.836	0.587	0.386
Glide height (nm)	4.857	3.735	1.962

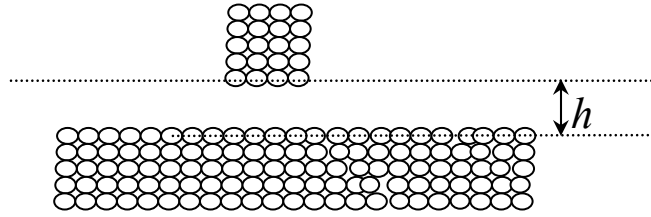


Fig.3.1. An infinite half space and a unit surface area of a parallel infinite half space.

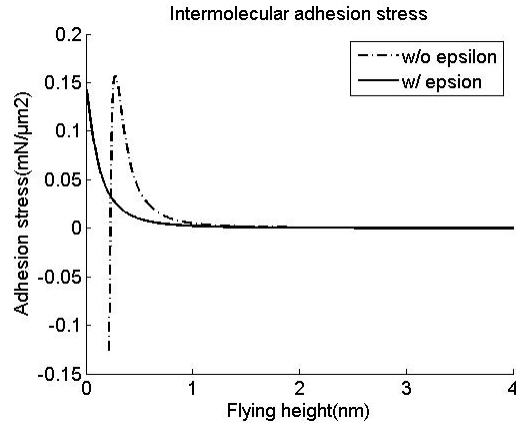


Fig.3.2. Adhesion stress obtained through intermolecular force model with and without considering the contact distance ϵ .

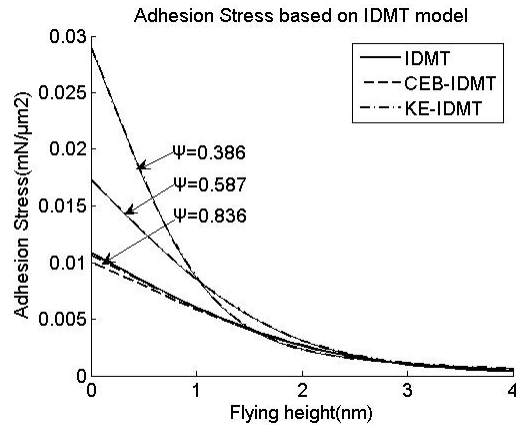


Fig.3.3. Adhesion stresses obtained through the IDMT, CEB-IDMT and KE-IDMT model.

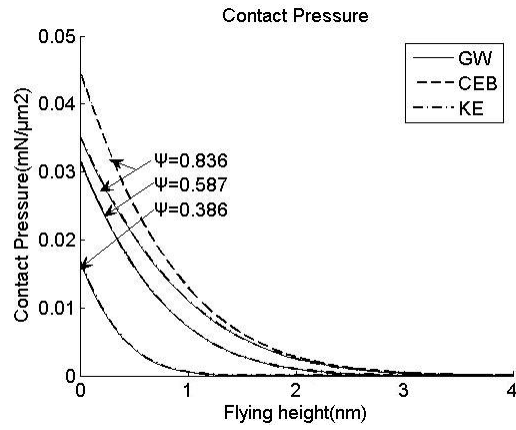


Fig.3.4. Contact pressure obtained through the GW, CEB and KE model.

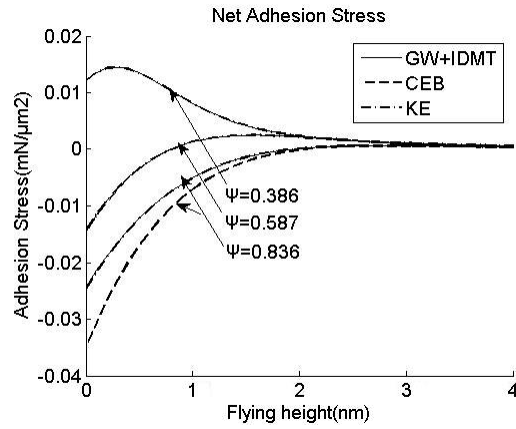


Fig.3.5. Net adhesion pressure obtained through the GW, CEB and KE contact and adhesion models.

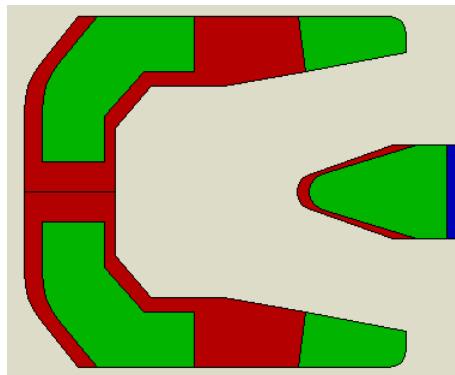


Fig.3.6. Air bearing surface of CML femto slider.

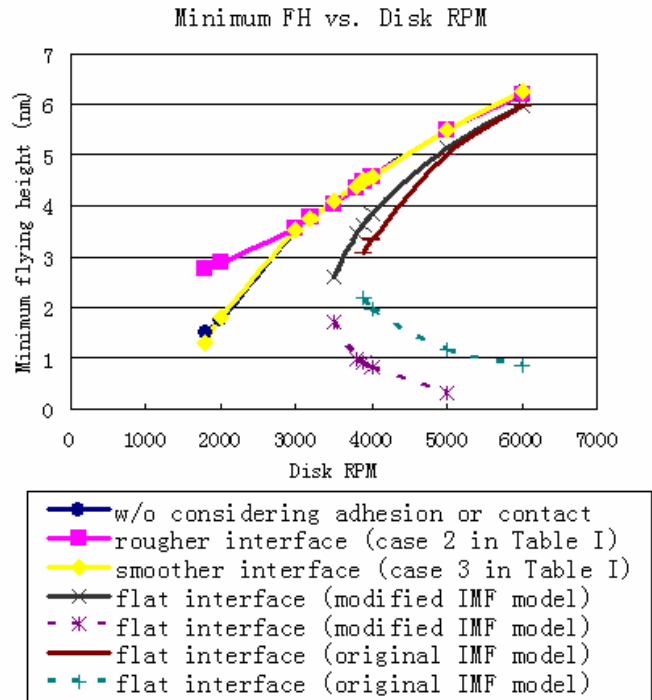


Fig.3.7. Minimum flying height versus disk RPM for the rougher slider/disk surfaces (case 2 in Table 3.1), smoother slider/disk surfaces (case 3 in Table 3.2), flat slider/disk interfaces and the case without considering the slider/disk adhesion or contact (the solid lines represent stable equilibria and the dotted lines represent unstable equilibria).

Chapter 4 Dynamics of a Partial-Contact

Head Disk Interface

Based on the contact models and intermolecular adhesion models analyzed in Chapter 2 and Chapter 3, a nonlinear dynamics model is developed in this chapter to analyze the bouncing vibration of partial-contact air bearing sliders, which are designed for the areal density of 1 Tbit/in² and even above. In this model the air bearing with contact is modeled using the generalized Reynolds equation modified with the Fukui-Kaneko slip correction [1] and a recent slip correction for the contact situation [2]. The adhesion, contact and friction between the slider and the disk are also considered in this model. The adhesion force is calculated using a modified intermolecular force model as presented in the previous chapter; the contact force is obtained through an elastic quasi-static contact model that incorporates the slider and disk measured roughnesses. Realistic measured profiles of the slider and disk are used in the simulation. It is found that minimizing the trailing pad size can significantly reduce the slider's bouncing and crash likelihood. The surface roughness and adhesion have a strong effect on the slider's bouncing vibration, while the friction between the slider and disk is found here to have less effect. The slider's bouncing can be decreased without much increase in contact force, to some extent, through increasing the preload.

4.1 Introduction

Reducing the flying height (FH) of sliders is a requirement to achieve higher recording densities in hard disk drives. The Wallace spacing loss equation reveals that the

magnetic signal increases exponentially as the distance decreases between the magnetic media and the read/write transducer. Reducing the flying height of the slider is necessary to achieve this lower spacing, since the protective layers- e.g. the slider and disk DLC and lubricant- must have certain minimum thicknesses for their performance. The maximum magnetic signal can be obtained at a spacing of zero, but this requires a contact recording interface.

There are several contact interface designs under consideration for the planned magnetic recording density of 1 Tbit/in² or more in Hard Disk Drives (HDD): “wear in”, “proximity”, and “full contact”. By a “wear-in” interface we mean an air bearing slider that initially flies with its trailing pad contacting the tallest disk asperities. After an initial service period it is expected that these asperities will be slightly worn so that the contact is lost. By “proximity” we mean an air bearing in which there continues to be intermittent or continuous contact between the trailing pad and the disk, while “full contact” means a contact interface without an air bearing. It is expected that all of these technologies, except possibly the last one, will rely on an air bearing to support most of the suspension load, while the trailing pad of the slider is in contact with the disk at the beginning, frequently or continuously. In this sense the HDI has partial contact.

In this chapter we develop a nonlinear dynamics model to analyze the bouncing vibration and contact of partial-contact sliders. In the model the partial air bearing is obtained through the generalized Reynolds equation modified with the Fukui-Kaneko slip correction [1] and a recent slip correction for the contact condition [2]. The adhesion, contact and friction between the slider and disk are also considered in this model. Realistic measured roughnesses of the slider and the disk are used in the simulation. It is found that minimizing the trailing pad size can reduce the slider’s bouncing and tendency

to crash. The surface roughnesses and adhesion between the slider and disk have a strong effect on the slider's bouncing vibration, while the friction between the slider and disk has less effect. The slider's bouncing can be decreased without much increase in contact force, to some extent, through increasing the preload.

4.2 Dynamics, Adhesion and Contact Models

The generalized time-dependent Reynolds equation is used to model the air bearing between the partial-contact slider and the disk. The Reynolds equation is modified using the Fukui-Kaneko (FK) slip correction [2] to account for the rarefaction of the ultra thin air film within the slider/disk spacing. As indicated in Wu and Bogy [1], the FK correction has an unbounded contact pressure singularity for the air bearing with contact. They proposed a new second order slip model without the pressure singularity, which predicts results not far from the FK correction when the modified inverse Knudsen number is small. For the contact region in an air bearing, Huang and Bogy [3] adopted in their Monte Carlo method a no-fly-zone condition, which assumes that air molecules can not enter a gap smaller than themselves. Here we combine the FK model and the new second order slip model. When the air film thickness is larger than 0.3 nm, close to the diameter of an oxygen or nitrogen atom, we use the FK model; when it is less than 0.3 nm, we use the new second order slip model to avoid the pressure singularity.

As analyzed in Chapter 2, the impact between the partial-contact slider and the disk is quasi-static and therefore can be modeled with an elastic contact model based on the static influence coefficient matrix. The CML slider dynamic simulation shows that the impact speed of the slider is on the order of 10^{-1} m/s. The sliding speed of the slider with respect to the disk, which is proportional to the disk rotation speed and the radial position

of the slider, is on the order of 10^1 m/s. Both speeds are much less than the elastic wave speeds in the disk media. So the slider-disk impact is quasi-static, which means that the deformation is restricted to the vicinity of the contact area and can be obtained through use of static contact theory. Johnson [4] described a contact model based on influence coefficients from an elasticity analysis of loading on an elastic half-space. This model can be incorporated with the approach that approximates the contact between two rough surfaces as that between a rigid flat surface and an equivalent elastic rough surface. We use this model instead of asperity-based contact models, such as that in the CEB model [5], because those models are only valid when bulk deformation and interactions between asperities are negligible. For a partial-contact HDI, the flying height at some parts of the air bearing surface (ABS) may be negative, which means that the distance between those parts of the slider and the undeformed disk surface is less than zero. Under this condition, bulk deformation and interactions between asperities are not negligible.

Adhesion is calculated through the modified intermolecular force model [6], which does not suffer from an infinite repulsion pressure when the slider and disk are in contact. The effect of the lubricant is included through the value of the surface energy difference before and after contact. This model is used instead of the asperity-based adhesion models, such as the CEB model, also because of the non-negligible bulk deformation and interactions between asperities.

As for the friction between the slider and disk, we use coulomb's law, the product of the normal contract force and a friction coefficient. Asperity-based friction force models, such as the CEB friction force model [7], are only valid for static friction with negligible bulk deformation and interactions between asperities. They are not suitable for the dynamic simulation of the partial-contact HDI. And no experimental work has shown that

the dynamic friction between the slider and the disk fits well with the asperity-based static friction model, although these models have been used in some published research papers.

All of these models were implemented in the CML slider dynamic air bearing program. The ABS is discretized into small grids, which are approximately parallel to the disk surface with different flying heights. The modified Reynolds equation is then discretized using Patankar's control volume method [8], and the final discretization equations are solved using the alternating direction line sweep method combined with the full multi-grid algorithm. Then the modified intermolecular force model and the elastic contact model are applied to each grid. The suspension is approximated here using three springs and three dampers in the vertical, pitch and roll directions. The dynamic program uses the Newmark Beta method to solve the slider dynamics equations.

4.3 Simulation Results and Discussion

Using the models described above, we analyze the dynamics of a partial-contact HDI. We employ micro-trailing pad sliders in the simulations. As was found in [9], in the contact regime a slider with a minimized trailing pad incurs smaller short range attractive forces between the slider and disk as well as less contact force. The ABS design of the slider is shown in Figure 4.1, and the related slider, disk and suspension parameters are listed in Table 4.1. In the dynamic simulation we analyze the effect of the trailing pad width, disk roughness, change of surface energy ($\Delta\gamma$), friction coefficient and suspension preload on the slider's bouncing vibration and the contact force. These parameters have various values and those with an upper asterisk are the default values used in the simulations. A partial-contact HDI should have less slider bouncing and a smaller contact

force. Less bouncing keeps a stable head media spacing; smaller contact force does not incur serious wear, and therefore gives a more stable and reliable HDI.

4.3.1 Disk Roughness and Surface Energy Change

We use one ideally smooth disk and two real disks with measured track profiles in the simulation. The root-mean-square (RMS) values of the two surface profiles are 0.2 nm and 0.6 nm, respectively. Figure 4.2 shows the history of the flying height, pitch angle, roll angle and contact force, as well as the frequency analyses of the flying height, pitch angle and roll angle of the slider on the disk surface with RMS roughness equal to 0.6 nm. It is seen that the slider continuously bounces on the rougher surface with two frequency components; one is around 150 KHz and the other is about 900 KHz. The slider's pitch motion also has these two frequency components. The situation is the same on the disk surface with RMS roughness equal to 0.2 nm. On the flat disk the slider flies on the disk with a slight contact. And its vibration does not have the 900 KHz frequency component. This higher frequency component is evidently associated with the slider-disk contact. The elastic contact between the slider and the disk has a much larger contact stiffness than the rear air bearing, and this evidently causes the higher pitch frequency. The roughness of the disk can excite this high frequency component.

Figure 4.3 shows the 3-sigma of slider bouncing displacement vibration and the mean contact force on disk surfaces with various RMS roughness and $\Delta\gamma$ values. It is seen that disk roughness is the main cause of the slider's bouncing. On the ideally smooth disk the slider achieves steady state without bouncing, while the slider's bouncing increases as the disk surface becomes rougher. Since $\Delta\gamma$ is proportional to the Hamaker constant [6], increased $\Delta\gamma$ means increased slider-disk adhesion. Increased slider-disk adhesion incurs more slider bouncing and larger contact force.

Usually the smoother the disk surfaces are, the larger is the adhesion between the slider and the disk [6]. Our dynamic model separates the roughness factor and the adhesion factor. But we still can see that a partial-contact HDI needs to balance the surface roughness and the adhesion.

4.3.2 Friction Coefficient

The dynamic friction coefficient of today's DLC coated disks with lube is usually less than 1. In our simulation we use three different values, 0, 0.3 and 0.6. Figure 4.4 shows the corresponding 3-sigma of slider bouncing displacement vibration and mean contact force on disk surfaces with two values of $\Delta\gamma$. It shows no dramatic difference between these cases with different friction coefficients. This partially contradicts the analysis of Ono and Yamane [10] on the effect of a wide range of friction coefficients. They asserted that friction excites the slider vibration. Actually the adhesion and contact force exerts larger torques than the friction force with respect to the slider's mass center, since the pitch angle is on the order of several hundred micro radians and the friction force is almost parallel to the ABS. So the effect of the friction force on slider bouncing might be important when the friction coefficient is larger than 1 and the slider's pitch angle is also very large. In our cases we do not expect major effects of the friction coefficient on the partial-contact slider dynamics.

4.3.3 Micro-Trailing Pad Width

Here we analyze the dynamics of partial-contact sliders with the trailing pad widths of 120 μm , 100 μm to 80 μm . Figure 4.5 shows the 3σ of the slider's bouncing displacement vibration and mean contact force of each design. Obviously the decrease of trailing pad size from 120 μm to 100 μm causes a decrease of the slider's bouncing and

contact. However, the further decrease from 100 μm to 80 μm only slightly reduces the mean contact force. Decreasing the slider's trailing pad width can lessen the slider's bouncing and contact to some extent. A partial-contact HDI relies on a trailing pad contact to support part of the suspension load. Also the read/write structure needs to be embedded in the trailing pad. So the trailing pad width can not be decreased beyond a certain value. For a stable HDI the micro trailing pad needs to be optimized as part of the ABS design.

4.3.4 Preload

The effect of suspension preload on the slider dynamics is analyzed with a simple spring-damper model for the suspension. Three levels of preload are used in the simulation, 0.1 gm, 0.8gm and 1.6gm, where 0.8gm is a typical preload for a femto slider. Figure 4.6 shows the 3-sigma of the slider bouncing displacement vibration and mean contact force under different values of preload. The result illustrates the high nonlinearity of the air bearing. The increased preload changes the slider attitude, causing the air bearing force to increase. Hence the mean contact force does not increase as much as the preload. As the preload increases, the mean contact force increases, while the slider's bouncing vibration decreases. However, the slope of the decreasing bouncing vibration is much steeper than that of the increasing mean contact force. This means that the slider's bouncing can be suppressed without much increase in the mean contact force, to some extent, through increasing the preload.

4.4 Conclusions

Our nonlinear dynamics model, which includes the generalized Reynolds equations for the air bearing, an elastic contact model for the slider-disk impact and the modified

intermolecular force model for the slider-disk adhesion can simulate the partial-contact head disk interface. In the dynamic simulations we found that,

1. As the slider-disk adhesion increases, the slider's bouncing amplitude is increased and the contact force is also increased.
2. Disk roughness is a main factor of slider bouncing.
3. The friction coefficient of the disk surface has a slight effect on the slider's bouncing.
4. Minimizing the trailing pad width can decrease the slider's bouncing and slider-disk contact to some extent.
5. The slider's bouncing can be suppressed without much increase in the mean contact force through increasing the preload.

References

- [1] S. Fukui and R. Kaneko, "Analysis of Ultra-Thin Gas Film Lubrication Based on Linearized Boltzmann Equation: First Report-Derivation of a Generalized Lubrication Equation Including Thermal Creep Flow," *ASME J. Tribol.*, vol. 110, pp. 253–262., 1988.
- [2] L. Wu and D. B. Bogy, "New First and Second Order Slip Models for the Compressible Reynolds Equation," *ASME J. Tribol.*, vol. 125, pp. 558-561, July 2003.
- [3] W. Huang and D. B. Bogy, "An Investigation of a Slider Air Bearing with an Asperity Contact by a Three-Dimensional Direct Simulation Monte Carlo Method," *IEEE Trans. Magn.*, vol. 34, No. 4, pp. 1810–1812, 1998.
- [4] K. L. Johnson, *Contact Mechanics*, Cambridge University Press, Cambridge, UK, 1985.

- [5] W. R. Chang, I. Etsion and D. B. Bogy, "An Elastic-Plastic Model for the Contact of Rough Surfaces," *ASME Jour. of Trib.*, vol. 109, pp 257-263, 1987.
- [6] D. Chen and D. B. Bogy, "Intermolecular Force and Surface Roughness Models for Air Bearing Simulations for Sub-5nm Flying Height Sliders," Technical Report No. 2006-016, Computer Mechanics Lab, Department of Mechanical Engineering, University of California, Berkeley.
- [7] W. R. Chang, I. Etsion and D. B. Bogy, "Static Friction Coefficient Model for Metallic Rough Surfaces," *ASME J. Tribol.*, vol. 110, pp. 57–63, 1988.
- [8] S. V. Patankar, *Numerical Heat Transfer and Fluid Flow*, McGraw-Hill, New York, 1980
- [9] J. Y. Juang, D. Chen and D. B. Bogy, "Alternate Air Bearing Slider Designs for Areal Density of 1 Tbit/in²," *IEEE Trans. Magn.*, vol. 42, No. 2, pp. 241-247, 2006.
- [10] K. Ono and M. Yamane, "Improved Analysis of Unstable Bouncing Vibration and Stabilizing Design of Flying Head Slider in Near-Contact Region," *ASME J. Tribol.*, vol. 129, pp. 65-74, 2007.

Table 4.1 Slider, disk and suspension specifications

Slider	Trailing pad width: 120 μm , 100 μm^* , 80 μm ; Slider Size: 0.85 \times 0.7 \times 0.23mm ³ ; Crown: 18 nm; Camber: 2.5nm; Twist: 0.0nm.
Disk	RMS: 0.0 nm, 0.2 nm [*] , 0.6nm; Change of surface energy: 0.008 J/m ² [*] , 0.08 J/m ² ; Friction coefficient: 0, 0.3 [*] , 0.6; Disk RPM: 10000; Slider skew angle: 6.65 $^\circ$.
Suspension	Preload: 0.1 gm, 0.8gm [*] and 1.6 gm.

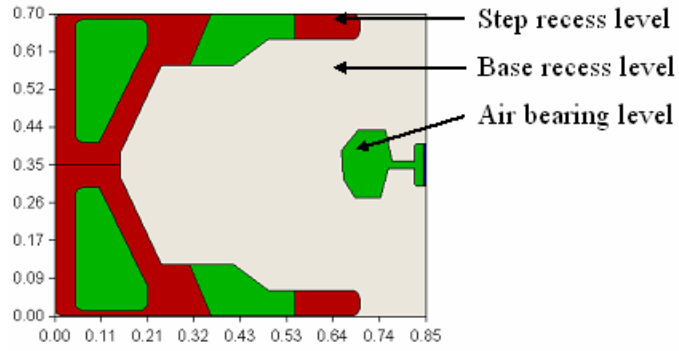
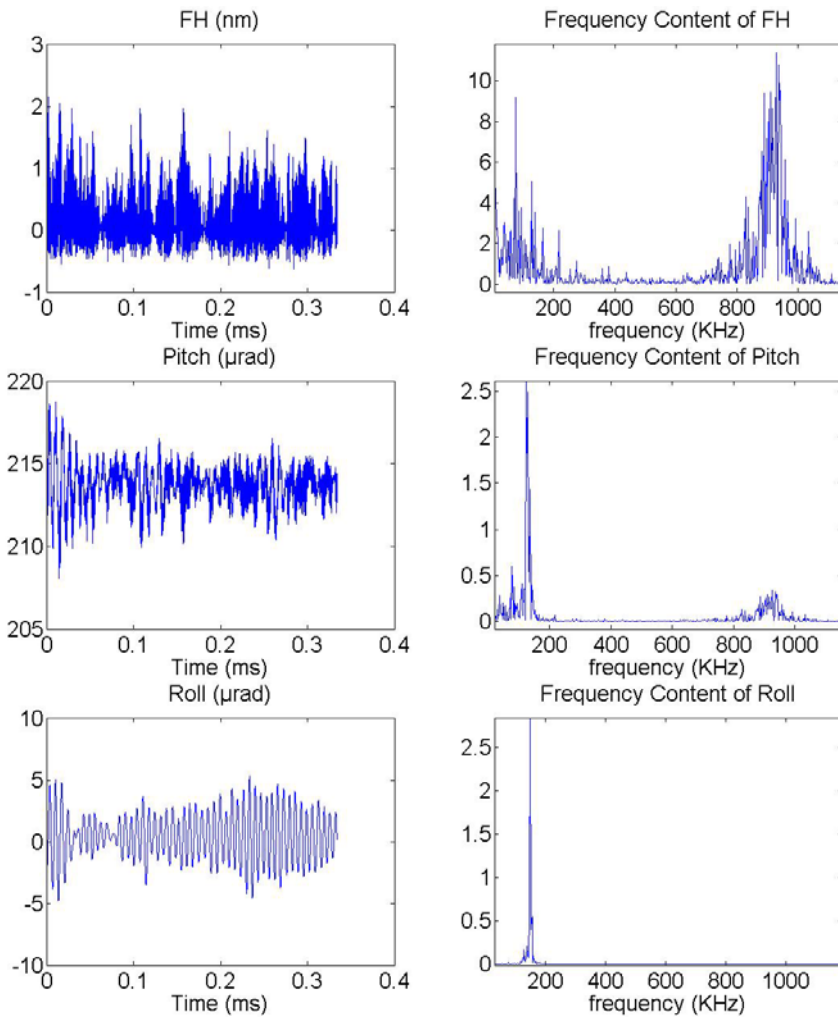


Fig.4.1. Air bearing surface design (unit: mm).



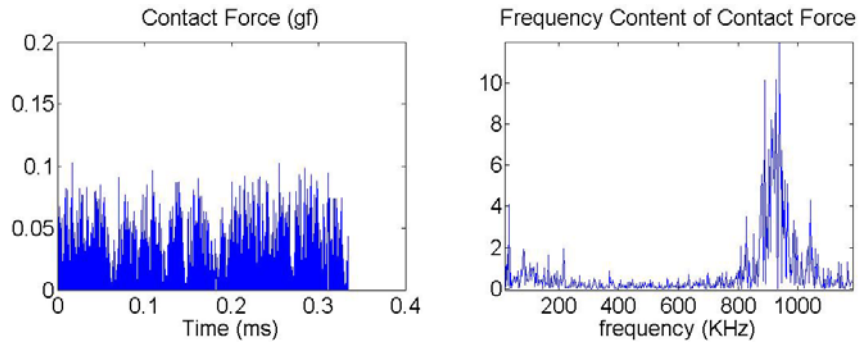


Fig.4.2. History of the FH, pitch, roll and contact force and their frequency analyses on the disk surface with RMS 0.6 nm.

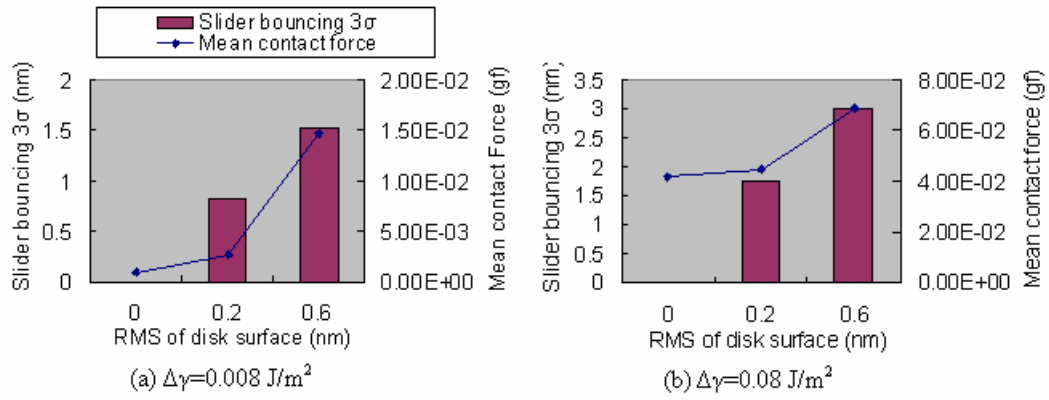


Fig.4.3. Slider bouncing 3σ and contact force on disk surfaces with various RMS and $\Delta\gamma$ values.

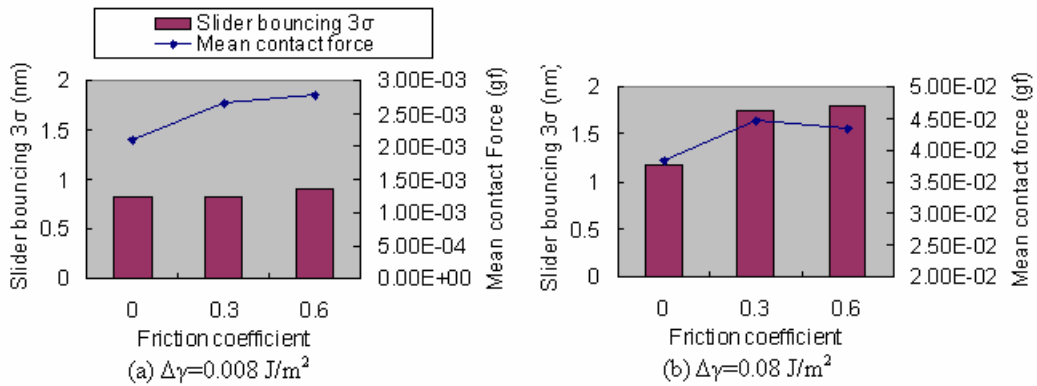


Fig.4.4. Slider bouncing 3σ and contact force on disk surfaces with various friction coefficients and $\Delta\gamma$ values.

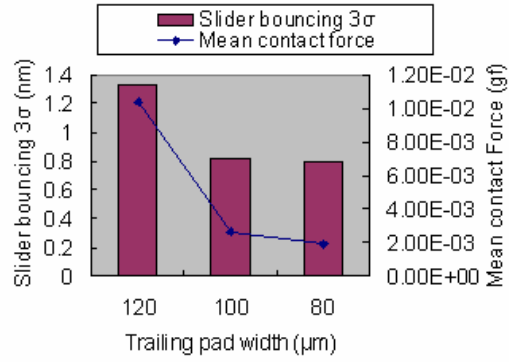


Fig.4.5. Slider bouncing 3σ and contact force of micro trailing pad sliders with various pad widths.

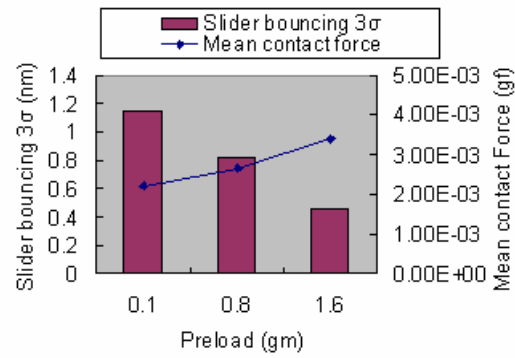


Fig.4.6. Slider bouncing 3σ and contact force of micro trailing pad sliders with various values of preload.

Chapter 5 Six-Degree-of-Freedom Vibrations of Partial-Contact Sliders in Hard Disk Drives

For a partial-contact slider the air shear and friction acting on the air bearing surface may cause the slider to experience in-plane motions, so that the slider has both bouncing and in-plane vibrations on the disk surface. The slider's bouncing vibration may cause an unacceptably large FH variation, while the in-plane vibration may cause a large off-track variance, which reduces the slider's track following capability. In this chapter we develop a nonlinear dynamic model to numerically analyze the in-plane vibrations of partial-contact sliders. The slider's motion in the vertical, pitch, roll, down-track, off-track and yaw directions, the partial-contact air bearing and the adhesion, contact and friction between the slider and disk are all considered in this model. Realistic, measured disk track profiles are used in the simulations. It is found that the in-plane vibrations of the partial-contact slider with a micro-trailing pad are dominated by the suspension modes, and they are forced vibrations caused by the slider-disk friction. Increasing the suspension damping is critical to minimizing the in-plane vibration amplitudes. Friction and contact pad size have important effects on the slider's in-plane vibrations.

5.1 Introduction

As discussed in previous chapters, reducing the flying height (FH) of sliders is a requirement to achieve higher recording densities in hard disk drives, and it leads to the

proposal of a partial-contact head disk interface. For a partial-contact slider the air shear and friction acting on the air bearing surface (ABS) may cause in-plane vibrations as well as a bouncing vibration of the slider on the disk. The slider's bouncing vibration may cause an unacceptably large FH variation; on the other hand, the in-plane vibration may cause a large off-track variance. The off-track vibration reduces the slider's track following capability and affects the recording track density. In this chapter we develop a nonlinear dynamic model to numerically analyze the in-plane vibrations of partial-contact sliders. In the model the partial-contact air bearing is obtained using the generalized Reynolds equation modified with the Fukui-Kaneko slip correction together with a recent slip correction for the contact condition, as in Chapter 4. A six-degree-of-freedom (6-DOF) model of the slider's motion is implemented to model the slider's vibrations in the vertical, pitch, roll, down-track, off-track and yaw directions, the last three of which contribute to the slider's in-plane vibration. The adhesion, contact and friction between the slider and disk are also considered in this model. Realistic, measured disk track profiles are used in the simulations.

It is found that the in-plane vibrations of the partial-contact slider with a micro-trailing pad are dominated not by the air bearing modes but by the suspension modes. Increasing the suspension damping is critical to decrease the in-plane vibration amplitudes. The in-plane vibrations are forced vibrations under the slider-disk friction. The disk micro-waviness and roughness can excite the vertical bouncing of the slider but they may not directly excite the in-plane vibration. Friction and contact pad size have important effects on the slider's in-plane vibrations.

5.2 Air bearing, Adhesion, Contact and Friction Models for Partial-Contact Sliders

The air bearing with contact, the slider-disk adhesion, contact and friction are all modeled as in Chapter 4. The generalized time-dependent Reynolds equation is used to model the air bearing between the partial-contact slider and the disk. When the air film thickness is larger than 0.3 nm, close to the diameter of an oxygen or nitrogen atom, we use the FK model; when it is less than 0.3nm, we use the new second order slip model to avoid the pressure singularity. The quasi-static impact between the partial-contact slider and the disk is modeled with an elastic contact model based on the static influence coefficient matrix. Coulomb's law is used for the slider-disk dynamic friction, i.e. the product of the normal contact force and a friction coefficient.

All of these models were implemented in the CML slider dynamic air bearing program. The ABS is discretized into small grids, which are approximately parallel to the disk surface with various spacings from the disk. The modified Reynolds equation is then discretized using Patankar's control volume method, and the final discretized equations are solved using the alternating direction line sweep method combined with the full multi-grid algorithm. The modified intermolecular force model and the elastic contact model are applied to each grid.

5.3 Six-DOF Slider Dynamic Model

Suppose that the suspension with length r rotates with an angular velocity ω and an angular acceleration a . The suspension is approximated here using six linear springs and six linear dampers in the x , y , z , roll, pitch and yaw directions. The x , y and z directions are shown in Figure 5.1, where the xyz coordinate system is attached to the suspension.

Let φ , θ and β indicate the roll, pitch and yaw angles of the slider's motion. The position of the suspension load point on the slider's upper surface is (x_0, y_0, z_0) . Let (x_c, y_c, z_c) indicate the position of the slider's mass center. If we have obtained the air bearing pressure p , the adhesion/contact force and moment with respect to the mass center, F_d and M_d , the air shear force and moment, F_a and M_a , the slider-disk friction force and moment F_f and M_f , then the equations of motion of the slider's mass center within the xyz coordinate system are,

$$\begin{aligned}
m\ddot{x}_c + c_x\dot{x}_c + k_x x_c &= F_{sx} + F_{fx} + m\omega^2 r + 2m\omega\dot{y}_c \\
m\ddot{y}_c + c_y\dot{y}_c + k_y y_c &= F_{sy} + F_{fy} + mar + 2m\omega\dot{x}_c \\
m\ddot{z}_c + c_z\dot{z}_c + k_z z_c &= F_0 + F_d + \iint_{ABS} (p - p_0)dA
\end{aligned} \tag{1}$$

The $x'y'z'$ coordinate system is attached to the slider's mass center with x' , y' and z' along the slider's length, width, and thickness directions, respectively. Suppose that the slider's vibrations in the pitch, roll and yaw directions are very small, then the directions of the x' , y' and z' axes are very close to those of the x , y and z axes, respectively. Neglecting the second order terms and using Euler's equations for dynamics of a rigid body, we can approximate the slider's equations of angular motion as,

$$\begin{aligned}
I_\varphi\ddot{\varphi} + c_\varphi\dot{\varphi} + k_\varphi\varphi + \dot{\theta}\dot{\beta}(I_\beta - I_\theta) &= M_{d\varphi} + M_{f\varphi} + M_{s\varphi} + (k_z z_0 + f_0)(y_c - y_0) \\
&\quad + \iint (p - p_0)(y_c - y)dA + k_y y_0 z_c \\
I_\theta\ddot{\theta} + c_\theta\dot{\theta} + k_\theta\theta + \dot{\beta}\dot{\varphi}(I_\varphi - I_\beta) &= M_{f\theta} + M_{s\theta} + M_{d\theta} + (k_z z_0 + f_0)(x_0 - x_c) \\
&\quad + \iint (p - p_s)(x_c - x)dA + k_x x_0 z_c \\
I_\beta\ddot{\beta} + c_\beta\dot{\beta} + k_\beta\beta + \dot{\varphi}\dot{\theta}(I_\theta - I_\varphi) &= M_{f\beta} + M_{s\beta} + k_x x_0 (y_c - y_0) + k_y y_0 (x_0 - x_c)
\end{aligned} \tag{2}$$

where I_φ , I_θ and I_β are the mass moments of inertia of the slider about the roll, pitch and yaw directions, respectively. The slider's equations of motion show that the in-plane vibration is caused by the air shear and slider-disk friction acting on the ABS. The effect of the

load offset, which corresponds to the terms $k_x x_0 (y_c - y_0)$ and $k_y y_0 (x_0 - x_c)$, can be damped out. The in-plane displacements also have effects on the slider's movement in the pitch and roll directions.

The Newark-Beta method is used in the CML dynamic program to solve the six equations of motion of the 6-DOF slider. The in-plane vibrations of the slider include the slider's vibration in the x , y and yaw directions. Let C denote the point at the trailing edge center, and let ψ denote the skew angle. Then the off-track and down-track displacements of the trailing edge center can be expressed as,

$$\begin{aligned} \text{off-track} &= \cos \psi (\|GC\| \sin \beta + y_c) + \sin \psi (\|GC\| \cos \beta + x_c), \\ \text{down-track} &= \sin \psi (\|GC\| \sin \beta + y_c) + \cos \psi (\|GC\| \cos \beta + x_c). \end{aligned} \quad (3)$$

5.4 Dynamic Simulations of a Micro Trailing Pad Slider

A micro-trailing pad slider is employed in the simulations. As was found in [1], in the contact regime a slider with a minimized trailing pad incurs smaller short range attractive forces between the slider and disk as well as less contact force. It is a good candidate to be a partial-contact slider with small bouncing vibrations and small contact and adhesion forces. The ABS design of the slider is shown in Figure 5.2. The steady state minimum flying height of the slider on a flat disk surface is approximately 0.5 nm and the transducer flying height is 2.5 nm. The suspension stiffness parameters are listed in Table 5.1, which are obtained from the finite element analysis of a suspension model. And the suspension damping coefficients used in the simulation are also listed in Table 5.1.

5.4.1 Dynamic response to an Initial Excitation

The dynamic response of the micro-trailing-pad partial-contact slider to an initial excitation is analyzed first. The slider is loaded onto a flat disk surface from a 2 nm initial

FH, steady state pitch and roll angles, zero in-plane displacements and zero yaw angle. Figure 5.3 shows the time histories of the slider's minimum FH, pitch, roll, down-track, off-track displacements and contact force and the corresponding power spectra. It is seen that the minimum FH, pitch and roll have only small variations at the beginning. Then the initial excitation is damped out quickly and the slider achieves a steady state with a minimum FH close to 0.5 nm. The corresponding spectra plots show that the minimum FH and pitch vibration have frequency peaks around 8 kHz, 126 kHz and 385 kHz with its harmonic frequency around 770 kHz. The roll vibration has two peaks around 8 kHz and 133 kHz. The 1st pitch, roll and 2nd pitch modes of the air bearing are clearly shown. The down-track and off-track vibrations are dominated by only one frequency component around 8 kHz and they are damped out much more slowly than the vertical vibrations. The in-plane suspension force acting on the slider due to the slider's in-plane displacement exerts a moment with respect to the slider's mass center, since the load point is on the slider's upper surface. This moment has components in the pitch and roll directions. So the slider's pitch, roll and minimum flying height are affected by the slider's in-plane vibration and they all have the 8 kHz frequency component. This frequency is clearly associated with a suspension mode. However, due to the simple spring-damper model of the suspension, the modes of the suspension can not be fully shown in the slider's in-plane vibration.

If no suspension damping is added in the simulation the slider's dynamic response changes to that in Figure 5.4. The vertical, pitch and roll vibration components with air bearing frequencies are still damped out quickly. However, the low-frequency components of the out-of-plane and in-plane vibrations can not be damped out. The high damping ratio of the air bearing has no effect on the slider's in-plane vibrations. This

agrees with all of the simulation results with a full suspension model in [2], which have zero suspension damping. So the suspension damping is critical to the slider's in-plane vibration.

5.4.2 Effect of Disk Micro-Waviness and Roughness

As shown in [3], the disk micro-waviness and roughness, which move through the HDI as the disk rotates, can excite the slider's vertical bouncing vibration. The effect of disk roughness on the slider's in-plane vibration needs to be investigated. Figure 5.5 shows a measured track with RMS roughness of 0.2 nm and the power spectrum of the track profile with a speed of 24 m/s, which corresponds to 10000 rpm. The power spectrum of the disk profile has peaks in a wide frequency range. Figure 5.6 shows the time history of the slider's minimum FH, down-track and off-track displacements and contact force on this track and the corresponding power spectra. The slider's vertical bouncing is excited and its two dominant frequencies are approximately 8 kHz and 400 kHz with its harmonic frequency 800 kHz. The disk roughness moves into the HDI as the disk rotates, so the excitation never stops and the slider's vertical bouncing vibration is continuous. The excited air bearing frequency is increased due to the slider-disk contact. The power spectra of shear forces in the X and Y directions show that all of the spectrum peaks are less than 0 dB. So the variation of shear force is extremely small. The contact force has frequency content similar to that of the minimum FH. The friction force, which is proportional to contact force, has the same frequency content. Notice that in this case the skew angle is zero, so the friction force is mainly along the slider's length direction, i.e. down-track direction. Therefore the off-track vibration does not contain the air bearing frequency component and the vibration amplitude is negligible. However, the down-track vibration does not contain the air bearing frequency components, either. This

can be simply explained with the steady state response of a one-degree-of-freedom forced spring mass system. The steady state vibration amplitude is

$$\frac{F_0}{K} / \sqrt{\left(1 - \frac{f^2}{f_n^2}\right)^2 + \left(2\zeta \frac{f}{f_n}\right)^2}, \quad (4)$$

where F_0 is the amplitude of the external force and f is its frequency; K , ζ and f_n are the stiffness, damping factor and natural frequency of the system, respectively. Here we take $K = 1.316 \times 10^3$ N/m, i.e. the X -stiffness of the suspension; $f_n = 8$ kHz, the suspension frequency, and $f = 400$ kHz, an excited air bearing frequency. Even if we take the damping factor to be zero and the peak to peak amplitude of the contact force at 400 kHz to be 0.1 gf, then $F_0 = 0.1/2 \times 0.3 \times 9.8$ mN = 0.147 mN, and the steady state amplitude obtained is approximately 0.05 nm. This small vibration amplitude is still negligible compared with the down-track vibrations shown in Figure 5.6. This calculation qualitatively agrees with the experimental analysis of [4], in which one of the experimental cases showed that the air bearing pitch modes had amplitudes as large as 20.5 nm in vertical bouncing but only 1 nm in the down-track vibration and 0.01 nm in the off-track vibration.

5.4.3 Effect of Skew Angle

It is expected that the component of the friction force along the off-track direction increases from zero and hence the off-track vibration increases, as the skew angle deviates from zero. But the effect of skew angle on slider dynamics interferes with other effects. In simulations it is difficult to change the skew angle while keeping the slider's air bearing and static flying height unchanged. Figure 5.7 shows the time histories of the minimum FH, off-track and down-track displacements of the same simulation case as in

Figure 5.6 except that the skew angle is changed from 0° to 6.65° . The in-plane vibration amplitudes are increased. This is partially caused by the increased vertical bouncing vibrations and the increased contact force variation, which is due to the change of skew angle. But the off-track vibration amplitude increases by three orders of magnitude. This is caused by the non-zero friction force in the slider's width direction, due to the non-zero skew angle.

5.4.4 Effect of Friction

The effect of friction force on the slider's motion can be analyzed with simulations using different friction coefficients, since Coulomb's law is used for the friction force. Figure 5.7 shows the vertical bouncing, contact force, down-track and off-track vibrations of the slider on a smooth disk with friction coefficients 0, 0.3, 0.6, 1 and 2, respectively. Here the skew angle is 6.65° . When the friction coefficient is zero, the initial in-plane vibrations are totally damped out. The reason is that the air shear almost remains constant, and it can not excite the in-plane vibrations. As shown in [3] the vertical bouncing vibration is almost not affected by the change of friction coefficient. However, as the friction force increases, the in-plane vibration amplitudes increase. Here we can roughly conclude that the off-track vibration peak-to-peak amplitude is on the order of 10 nm and the down-track vibration peak-to-peak amplitude is on the order of 100 nm when the contact force is less than 0.25 gf and the friction coefficient is less than 0.3. So a small dynamic friction coefficient is important for small in-plane vibrations.

5.4.5 Effect of the Micro Trailing Pad Width

The micro-trailing pad of the slider used in the above simulations has a width of 100 μm . Figure 5.8 shows the vertical bouncing, on-track and off-track vibrations of the slider with micro-trailing pad widths of 100 μm , 80 μm and 60 μm , respectively. As discussed

in [3], the slider's vertical bouncing reduces as the pad's width reduces. Here the simulations of in-plane vibrations show that down-track and off-track vibrations also decrease. If we check the contact force, we can see that the variation of the contact force decreases as the micro-trailing pad width decreases. A smaller contact pad helps to decrease the vertical bouncing and the variation of contact force; then the variation of friction force and in-plane vibrations are also reduced. This result agrees with the experimental observations in [5]. On the other hand, the width of the micro-trailing pad should also be large enough to embed the read/write transducer. So an optimized trailing pad size is important for reducing the vertical bouncing and the in-plane vibrations.

5.5 Conclusions

A six-degree-of-freedom slider dynamic simulator is developed to analyze the slider's motion in the vertical, pitch, roll, yaw, length and width directions. The modified time-dependent Reynolds equation is used to model the air bearing and a new second order slip model is used for a bounded contact air bearing pressure. The simulator considers the air bearing shear acting on the ABS and the slider-disk contact and adhesion. Dynamic simulations of a partial-contact slider with a micro-trailing pad are carried out. The simulation results show the following,

1. Within the HDI, the slider's in-plane vibrations are forced vibrations by the air shear and slider-disk friction. The air shear remains almost constant and the in-plane vibration is mainly caused by the slider-disk friction.
2. The in-plane vibrations are dominated by the suspension modes. The air bearing modes and damping do not have much effect on the in-plane vibrations. The damping of the suspension is critical to the decrease of in-plane vibration amplitudes.

3. Disk surface micro-waviness and roughness excite the slider's vertical bouncing. But the micro-waviness and roughness can not excite the slider's in-plane vibrations.
4. The slider's skew angle affects the slider's off-track vibrations. The change of skew angle can cause a change in the order of magnitude of the off-track vibration amplitude. The skew angle also has an effect on the slider's flying and contact attitude; accordingly, the vertical and in-plane vibrations are affected.
5. The slider-disk friction is critical to the in-plane vibration, although it does not affect the vertical bouncing. The smaller the slider-disk friction, the smaller will be the in-plane vibration amplitudes. The dynamic simulator roughly predicts that the off-track vibration peak-to-peak amplitude is on the order of 10 nm and the down-track vibration peak-to-peak amplitude is on the order of 100 nm when the contact force is less than 0.25 gf and the friction coefficient is less than 0.3.
6. For the micro-trailing pad slider, the slider with a reduced trailing pad width incurs smaller contact force variation, smaller contact force and smaller slider-disk adhesion force. And the vertical and in-plane vibrations are also reduced.

References

- [1] J. Y. Juang, D. Chen and D. B. Bogy, "Alternate Air Bearing Slider Designs for Areal Density of 1 Tbit/in²," *IEEE Trans. Magn.*, vol. 42, No. 2, pp. 241-247, 2006.
- [2] S. K. Yu, B. Liu, W. Hua and W. D. Zhou, "Contact-Induced Off-Track Vibrations of Air Bearing-Slider-Suspension System in Hard Disk Drives," *Tribol. Letters*, vol. 24, No. 1, pp. 27-36, 2006.
- [3] D. Chen and D. B. Bogy, "Dynamics of Partial Contact Head Disk Interface," *IEEE Trans. Magn.*, vol. 43, No. 6, pp. 2220-2222, 2007.

- [4] J. Kiely and Y. T. Hsia, "Three-Dimensional Motion of Sliders Contacting Media," *ASME J. Tribol.*, vol. 128, pp. 525-533, 2006.
- [5] J. Xu, H. Kohira, H. Tanaka and S. Saegusa, "Partial-Contact Head-Disk Interface Approach for High-Density Recording," *IEEE Trans. Magn.*, vol. 41, No. 10, pp. 3031-3033, 2005.

Table 5.1 Suspension model used in the simulation

Suspension model specifications
Suspension Load: 0.8gf
X stiffness: 1.316×10^3 N/m
Y stiffness: 1.458×10^3 N/m
Z stiffness: 1.593×10^1 N/m
Roll stiffness: 6.987×10^{-5} N·m/rad
Pitch stiffness: 3.769×10^{-5} N·m/rad
Yaw stiffness: 4.847×10^{-2} N·m/rad
X-damping: 5.13×10^{-3} N·s/m
Y-damping: 3.94×10^{-3} N·s/m
Z-damping: 4.73×10^{-5} N·s/m
Roll-damping: 3.42×10^{-10} N·m·s/rad
Pitch-damping: 2.82×10^{-10} N·m·s/rad
Yaw-damping: 3.20×10^{-6} N·m·s/rad

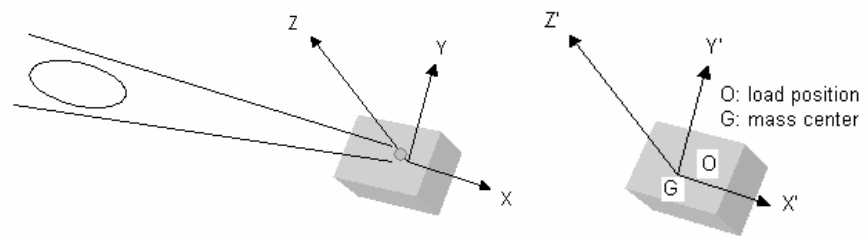


Fig.5.1. Suspension and slider coordinate systems.

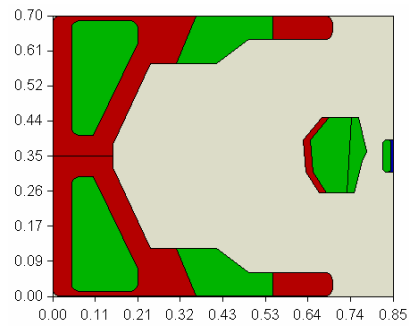


Fig.5.2. Air bearing surface design of femto slider (unit: mm).

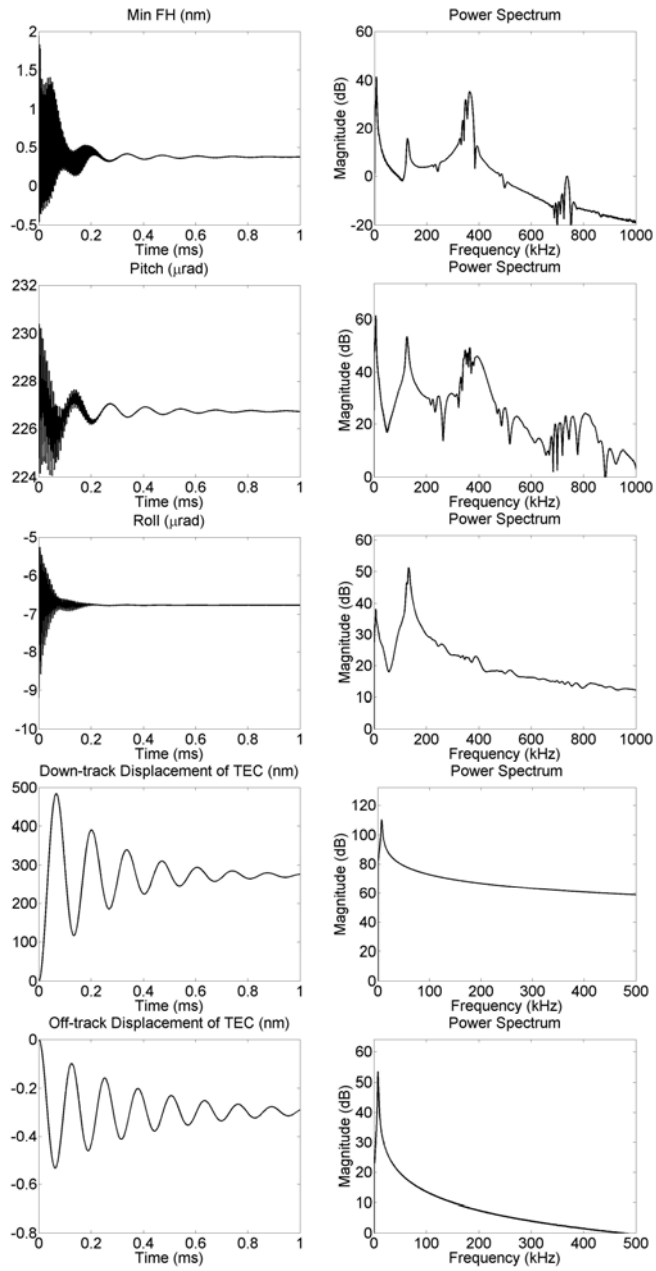


Fig.5.3. Dynamic response to an initial excitation of loading the slider from 2 nm onto a flat disk surface.

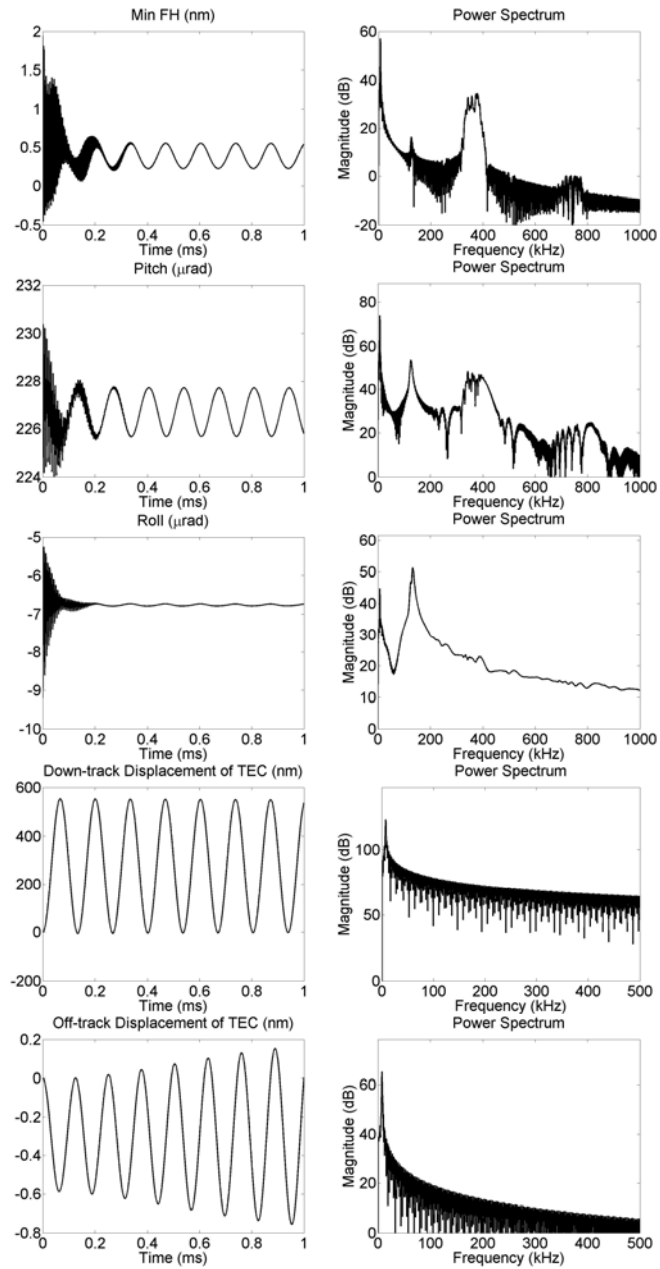


Fig.5.4. Dynamic response to an initial excitation of loading the slider from 2 nm onto a flat disk surface with zero suspension damping in the simulation.

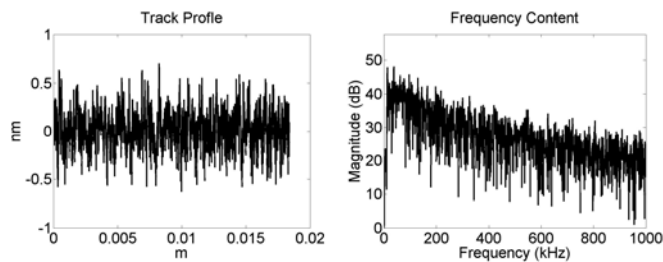


Fig.5.5. Measured track profile and its power spectrum at the disk velocity 24 m/s.

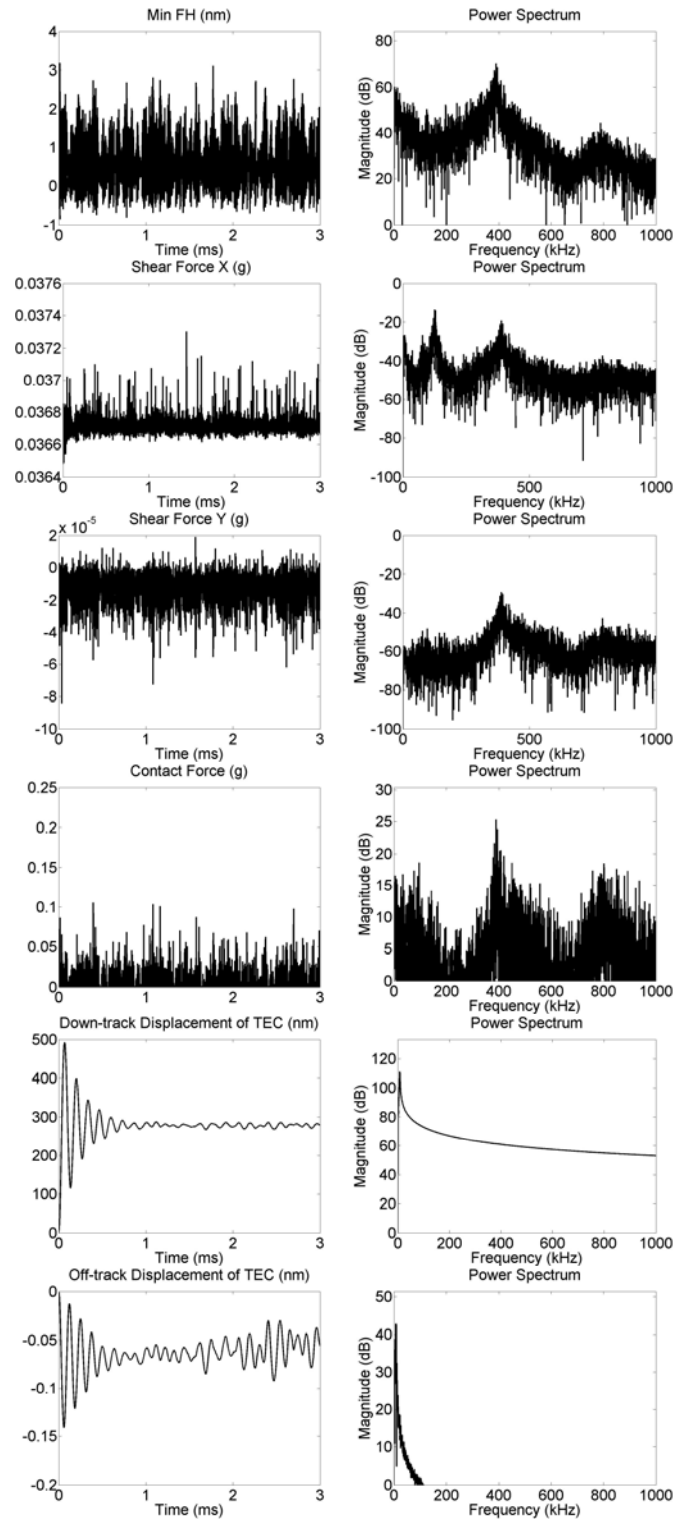


Fig.5.6. Time history of the slider on a smooth disk with RMS 0.2 nm and the corresponding power spectrum.

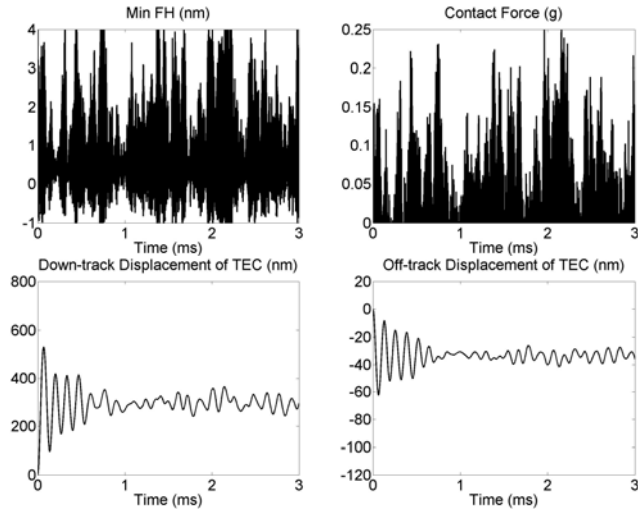
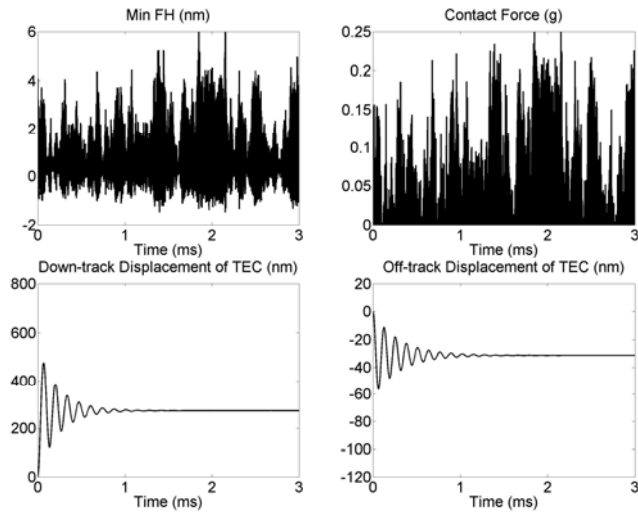
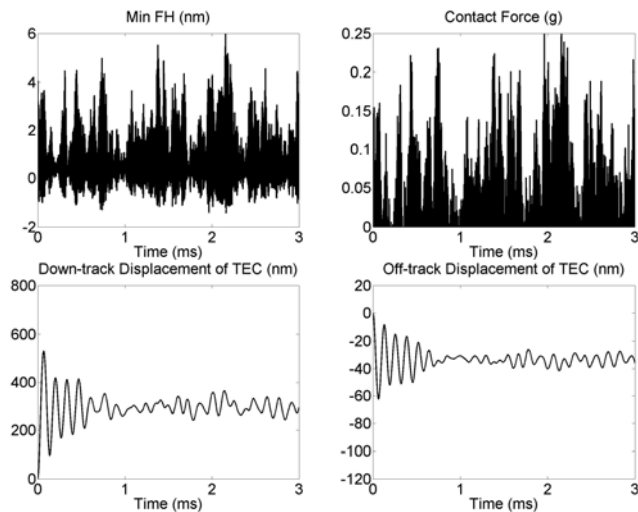


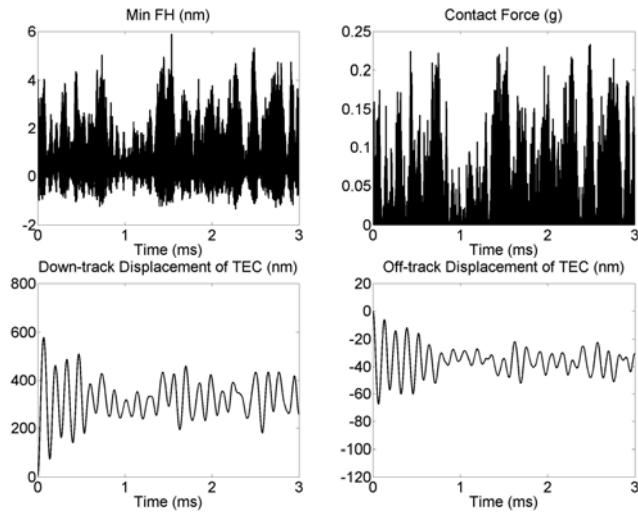
Fig.5.7. Time history of the slider with a skew angle of 6.65° .



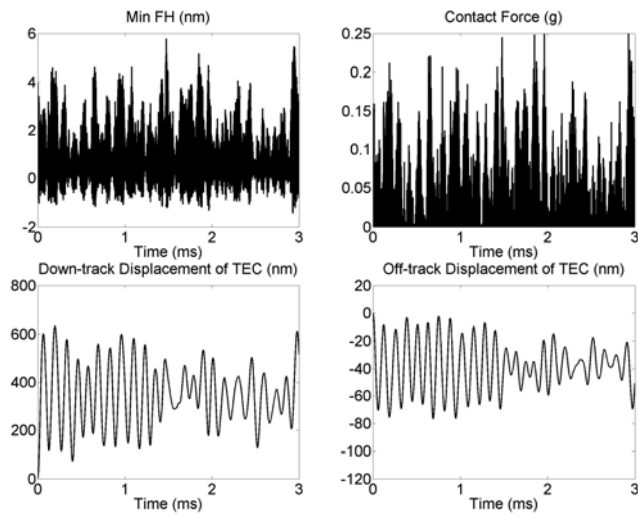
(a) Friction Coefficient 0.0



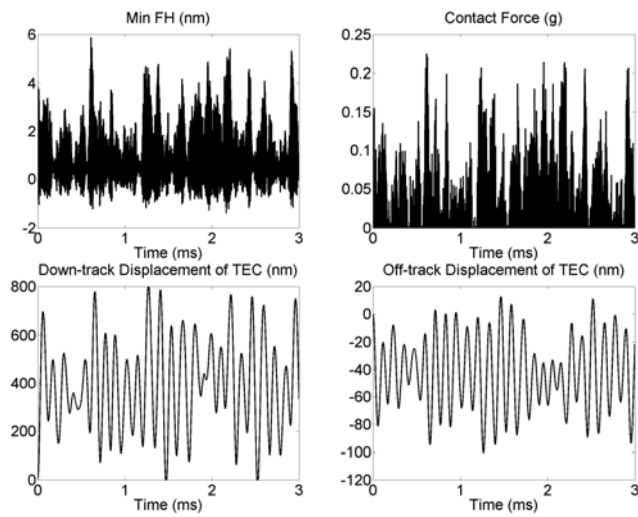
(b) Friction Coefficient 0.3



(c) Fiction Coefficient 0.6



(d) Fiction Coefficient 1.0



(e) Fiction Coefficient 2.0

Fig.5.8. Time history of the slider on a smooth disk on a smooth disk with different friction coefficients.

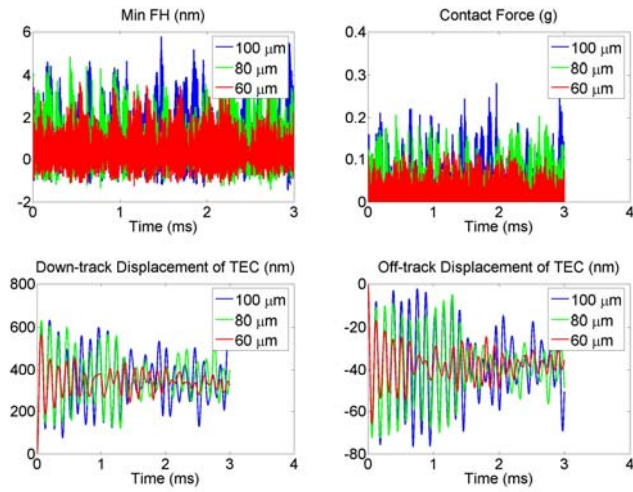


Fig.5.9 Time history of the slider with trailing pad width of 100 μm , 80 μm and 60 μm .

Chapter 6 Numerical Investigation of Bouncing Vibrations of an Air Bearing Slider in Near or Partial Contact

The bouncing vibration of an air bearing slider in near or partial contact with the disk is numerically analyzed using three different nonlinear slider dynamics models. The near or partial-contact slider is designed for the future areal recording density in hard disk drives of 1 Tbit/in² or even higher. In these three slider dynamics models, the air bearing with contact is modeled either using the generalized Reynolds equation modified with the Fukui-Kaneko slip correction and a recent second order slip correction for the contact situation, or using nonlinear springs to represent the air bearing. The contact and adhesion between the slider and the disk are considered either through an elastic contact model and an improved intermolecular adhesion model, respectively, or using an Ono-Yamane [1] multi-asperity contact and adhesion model. The contact friction is calculated by Coulomb's law. The simulation results from all models show that the slider's bouncing vibration occurs as a forced vibration caused by the micro-waviness and roughness. The disk surface micro-waviness and roughness, which move into the head disk interface (HDI) as the disk rotates, excite the bouncing vibration of the partial-contact slider. The contact, adhesion and friction between the slider and the disk do not directly cause a bouncing vibration in the absence of disk micro-waviness or roughness.

6.1 Introduction

As discussed in previous chapters, reducing the flying height (FH) of sliders is a requirement for achieving higher recording densities in hard disk drives, and it finally leads to a partial-contact head disk interface (HDI). As observed in experiments, the slider bounces on the disk surface as it touches the rotating disk. As to the cause of the slider's bouncing, different explanations have been put forward. The contact friction [1] or short-range forces between the slider and the disk [3 and 4] are two such proposed causes.

In order to investigate these mechanism further, three different nonlinear slider dynamics models are used in this chapter to numerically analyze the vertical bouncing vibration of an air bearing slider in the near or partial-contact region. Numerical simulations of the slider's dynamics show that the slider's bouncing vibration is a forced vibration caused by the micro-waviness and roughness. The disk surface micro-waviness and roughness, which move into the HDI as the disk rotates, excite the bouncing vibration of the partial-contact slider. The contact, adhesion and friction between the slider and the disk do not directly cause a bouncing vibration in the absence of disk micro-waviness or roughness.

6.2 Dynamics, Adhesion and Contact Models

The generalized time-dependent Reynolds equation is used to model the air bearing between the partial-contact slider and the disk. As discussed in Chapter 4, when the air film thickness is larger than 0.3 nm, which is approximately the diameter of an oxygen or nitrogen atom, the FK slip correction [2] is used to account for the rarefaction of the ultra

thin air film within the slider/disk spacing; when it is less than 0.3 nm, the new second order slip model is used to avoid the pressure singularity.

A simple alternative air bearing model uses non-linear springs to represent the air bearing [1]. The air bearing of the entire air bearing surface is modeled with a front lumped nonlinear spring, a front linear dashpot, a rear lumped nonlinear spring and a rear linear dashpot. The springs and dashpots are located at the front or rear air bearing pressure center. The spring stiffness values are chosen to match otherwise calculated or experimentally measured air bearing frequencies. And the damping coefficients are determined by preset damping ratios.

The impact between the partial-contact slider and the disk is quasi-static and therefore can be modeled using an elastic contact model based on the static influence coefficient matrix, as described in Chapter 2. Because of the bulk deformation, asperity adhesion models and asperity-based friction models are also not suitable for the dynamic simulation of the partial-contact HDI. Here adhesion is calculated through the improved intermolecular force model developed in Chapter 3, which does not predict an infinite repulsion when the slider and disk are in contact. The adhesion effect of the lubricant is modeled using the value of the surface energy difference before and after contact. Coulomb's law is used for the friction between the slider and disk.

Another slider-disk contact and adhesion model, developed by Ono and Yamane [1], is also used here for comparison. It is a complicated multi-asperity contact and adhesion model, which considers the bulk deformation of the contact interface and assumes that the lubricant meniscus is the only source of adhesion between the slider and disk. This model gives a stochastically averaged contact and adhesion force and the effect of asperities, which model the equivalent rough disk surface, on the air bearing is not

considered. In this model the contact and adhesion forces between a slider and a disk are functions of the spacing between the contact pad and the disk, given the statistical characteristics of the roughness on the disk surface (including the radius of curvature of asperities, the asperity density and the standard deviation of asperity heights), the contact pad area and the surface energy of the lubricant. With the assumption that the contact area does not change at any interference depth, the slider-disk contact characteristics can be simply described using the maximum value of adhesion force, the bulk contact stiffness, the initial real contact force at the beginning of contact and the touch-down and take-off flying heights [1].

6.3 Three Slider Dynamics Models

Two slider dynamics models are obtained by implementing the two sets of contact and adhesion models discussed above into the CML slider dynamics air bearing program. The ABS is discretized into small grids, which are approximately parallel to the disk surface with various flying heights. The modified Reynolds equation is then discretized using Patankar's control volume method, and the final discretization equations are solved using the alternating direction line sweep method combined with the full multi-grid algorithm. The dynamics program uses the Newmark-Beta method to solve the slider dynamics equations.

The third slider dynamics model analyzed in this chapter is the two-degree-of-freedom (2-DOF) slider model developed by Ono and Yamane [1]. It includes the nonlinear air bearing spring model and the simplified multi-asperity contact and adhesion model. The 4th order Runger-Kutta method is used to solve the slider's equations of motion, as was done in [1].

6.4 Slider Dynamics Simulation and Results

6.4.1 Dynamic Simulations Using the CML Air Bearing Model, the Elastic Contact

Model and the Modified Intermolecular Force Model

Using the first model described above we analyze the vertical bouncing vibration of a partial-contact HDI. We employ micro-trailing pad sliders in the simulations. As was found in [5], a slider in the contact regime with a smaller trailing pad may incur smaller short range attractive forces between the slider and disk as well as a reduced contact force. This helps to decrease the slider's tendency to crash in the partial-contact process. The ABS design of the slider is shown in Figure 6.1.

Here three different disk surfaces are used in the simulation. The first is an ideally flat disk surface, i.e. the RMS of the surface roughness is zero; the second is a "rough" disk surface with RMS roughness equal to 0.2 nm; the third is the same rough disk surface, but the disk micro-waviness and roughness within the HDI remains stationary. The third case is not practical, since the disk surface profile within the HDI keeps changing with the disk rotation. But we use this case to analyze the effect of dynamic roughness on the partial-contact HDI by comparison with the previous case.

Figure 6.2 shows the time histories of the minimum spacing between the slider and the mean plane of the disk surface, the pitch, the roll, and the corresponding power spectra of the minimum spacing for these three cases. We can see that in Case I and Case III the initial response of the slider to the loading process is quickly damped out and the slider achieves a continuous contact steady state. However, in Case II the slider keeps bouncing on the disk surface and the bouncing vibrations can not be damped. The frequency spectra of the minimum spacing in Case I and Case III are similar, while the

frequency spectrum in Case II is different and it has a series of peaks around 800 kHz. These higher frequency components are evidently associated with the slider-disk contact. The micro-waviness and roughness on the disk surface, which move into the HDI as the disk rotates, excite these high frequency components, and they cause the slider's continuous vertical bouncing vibration.

6.4.2 Dynamic Simulations Using the CML Air Bearing Model and the Multi-Asperity Contact and Meniscus Adhesion Model of Ono and Yamane

Ono and Yamane [1] successfully implemented their multi-asperity contact and adhesion model in their 2-DOF slider dynamics model to study the unsteady bouncing vibration of low flying height sliders on a disk surface without micro-waviness or roughness. They reached a conclusion that the bouncing vibration can also be a self-excited vibration caused by the adhesion and friction forces in the absence of moving disk micro-waviness or roughness. This is different from the conclusion presented above.

To analyze this self-excited vibration, Ono and Yamane's contact and adhesion model [1] is incorporated in the CML slider dynamics model in place of the elastic contact and improved intermolecular force models used above. First, in order to avoid the difficulties in applying this contact and adhesion model to the 3-DOF slider model in the CML air bearing program, we reduce the CML slider model to a 2-DOF one by employing a very large suspension roll stiffness so that the motion in the roll direction is negligible. Second, the simplified contact characteristic model is used instead of the full multi-asperity contact and adhesion model. The contact area is assumed to be constant and the statistical characteristics of the equivalent disk surface are the same as those used by Ono and Yamane. The separation between the contact pad and the mean disk surface is assumed to be equal to the minimum spacing between the slider and the mean disk surface. Here we

fix the bulk contact stiffness to be 5.0×10^6 N/m, the initial contact force to be 5.0 mN and the touch-down FH to be 3.0 nm. Values of the minimum adhesion force, the bulk contact stiffness and the takeoff flying height are shown in Table 6.1, where those with an upper asterisk are the default values used in the simulations.

The force hysteresis needs to be considered in implementing Ono and Yamane's model. Figure 6.3 shows the relations of the real contact force F_{cr} , adhesion force F_m , contact force F_c (the sum of real contact and adhesion force) versus the separation d between the contact pad and the disk in the simplified model. The arrows on the lines denote the touch-down and take-off processes. In the simulation it is assumed that the slider's initial state is touch-down if the initial separation is less than the take-off FH d_e . Then, the slider's current separation d determines the slider's state at the next time step, if the time step size used in the simulation is small enough. When the separation d is larger than d_e , the slider's state at the next time step is touch-down. When the separation d is less than d_s , the slider's state at the next time step is take-off or touch-down, but it can be set to take-off since the touch-down line and take-off line coincide when d is less than d_s . Then the slider's state at the next time step remains the same as the current state when the separation is between d_s and d_e .

A CML slider design is used in the simulation. The air bearing surface is shown in Figure 6.4. It is a pico size slider (1.25 mm \times 1.00 mm). The suspension preload is 1.5 gf and the disk RPM is 5400. Its static minimum flying height is approximately 3.2 nm and its pitch angle is approximately 176 μ rad on a flat disk surface. This means that the disk may contact the slider if the take-off FH is above 3.2 nm. Figures 6.5-6.8 show the time histories of the slider's dynamics with different maximum meniscus force, take-off FH, friction coefficient and initial FH, respectively.

The negative contact force in Figure 6.5 shows that the flying slider contacts the disk when the maximum meniscus force is increased to 15 mN. However, the slider's bouncing vibration is damped out even when the slider contacts the disk with a negative total contact force.

Figures 6.6-6.8 indicate the existence of two different steady states. Figure 6.6 shows that when the take-off FH is 4 nm, the slider does not contact the disk in the steady state; when the take-off FH is 5.5 nm or 8 nm, the slider contacts the disk in the steady state. Figure 6.7 shows that the slider contacts the disk in the steady state when the friction coefficient is increased to 2.0. Figure 6.8 shows that different initial FHs may also produce different final steady states. With an initial FH of 3.5 or 10 nm the slider does not contact the disk in the steady state; with an initial FH of 5 nm or 20 nm, the slider contacts the disk in the steady state. All of these indicate that the slider may have two different final steady states. One state is a flying state, i.e. the slider does not contact the disk. The other is a contact state with lower spacing, in which the slider contacts the disk with a negative total contact force. This negative total contact force is compensated by the increased air bearing force due to the lower spacing. The final state is determined by the take-off FH, the friction coefficient or the initial FH. However, the existence of these two steady states does not mean that the slider will vibrate between two states. Instead the slider's bouncing vibration is damped out quickly. In addition, the effect of the friction coefficient and the take-off FH can be seen from the simulation results. The contact steady state in Figure 6.7 has a smaller pitch angle than the contact steady state in Figure 6.8. This shows that a large friction coefficient may cause a low pitch angle when the slider contacts the disk. In Figure 6.6, the slider doesn't contact the disk until the take-off

FH is increased beyond 5.5 nm. It corresponds to an experimental observation that higher take-off FH causes a greater likelihood of slider disk contact.

In conclusion, the simulation results of the CML 2-DOF slider dynamics model, which incorporates Ono and Yamane's simple contact characteristic model for the slider disk contact and adhesion, show that the slider-disk contact, adhesion and friction are not the direct cause of the slider's bouncing vibrations. So this implies that the near or partial-contact slider-disk interface is not an adhesion and friction caused self-excited system as shown in [1]. The destabilizing mechanism of friction force shown in [1] might not provide a strong proof. On one hand, the work done by the friction to the air bearing-slider-suspension system is not guaranteed to be always positive. On the other hand, not only the friction force between the slider and the disk but also the contact force does work on the slider. The moment arm of the contact force is much larger than that of the friction force, given that the pitch angle is on the order of μrad . From these two points of view, the friction appears not to be the main cause of the slider's vibration. With the statistically averaged contact and adhesion model, it is even found that the adhesion force actually helps to reduce the bouncing vibrations [4].

6.4.3 Dynamic Simulations Using Ono and Yamane's 2-DOF Dynamics Model

The 2-DOF slider dynamics model of Ono and Yamane [1], with the simple nonlinear air bearing model and the multi-asperity contact and adhesion model, is re-analyzed here in an attempt to obtain a non-decayed bouncing vibration of a slider in the near or partial-contact regime on a disk without micro-waviness, which is shown in Section 3.3 of [1]. Figure 6.9 shows this 2-DOF system model. The air bearing is simply represented by two lumped nonlinear springs (stiffness coefficients k_f and k_r) and two linear dashpots (damping coefficients c_f and c_r) located at the front and rear bearing pressure centers,

respectively. With z_f and z_g denoting the spacing at the front and rear air bearing pressure center, respectively, the air bearing stiffnesses used in the model are expressed as,

$$k_r = \begin{cases} \frac{k_{r0} z_{r0}^2}{z_r^2}, & \text{when } z_r > d_1 \\ 0, & \text{when } z_r < d_1 \end{cases}; k_f = \begin{cases} \frac{k_{f0} z_{f0}^2}{z_f^2}, & \text{when } z_f > d_1 \\ 0, & \text{when } z_f < d_1 \end{cases}, \quad (1)$$

where the subscript 0 denotes the parameters in the static state and d_1 is a preset parameter. And the corresponding damping coefficients are $c_f = 2\xi_f \sqrt{Mk_{f0}}$ and $c_r = 2\xi_r \sqrt{Mk_{r0}}$. The suspension is represented by a normal linear spring (k) and dashpot ($c = 2\xi \sqrt{Mk}$), an angular spring (k_θ) and dashpot ($c_\theta = 2\xi_\theta \sqrt{Jk_\theta}$), static load (F_0) and static moment (M_0). The simplified contact characteristic model shown in Figure 6.3 is used to model the slider-disk adhesion and contact.

For a slider with a static flying height FH at the transducer and a static pitch angle θ_0 , the equation of motion of the slider is derived in [1] as,

$$\begin{aligned} \begin{bmatrix} M & 0 \\ 0 & J \end{bmatrix} \begin{Bmatrix} \ddot{z}_g \\ \ddot{\theta} \end{Bmatrix} + \begin{bmatrix} c_{11} & c_{21} \\ c_{21} & c_{22} \end{bmatrix} \begin{Bmatrix} \dot{z}_g \\ \dot{\theta} \end{Bmatrix} + \begin{bmatrix} k_{11} & k_{21} \\ k_{21} & k_{22} \end{bmatrix} \begin{Bmatrix} z_g \\ \theta \end{Bmatrix} \\ = \begin{Bmatrix} F_c(z_p) + F_0(FH, \theta_0) \\ -\frac{1}{2} b \mu F_{cr}(z_p) + d_h F_c(z_p) + M_0(FH, \theta_0) \end{Bmatrix}, \quad (2) \end{aligned}$$

where z_g denotes the vertical displacement of the center of mass from the mean roughness plane of the disk and θ denotes the angular displacement in the counter clockwise direction from the horizontal line.

Notice that for the static state,

$$\begin{bmatrix} k_{11} & k_{21} \\ k_{21} & k_{22} \end{bmatrix} \begin{Bmatrix} z_{g0} \\ \theta_0 \end{Bmatrix} = \begin{Bmatrix} F_0(FH, \theta_0) \\ M_0(FH, \theta_0) \end{Bmatrix} \quad (3)$$

Then if we define $z'_g = z_g - z_{g0}$ and $\theta' = \theta - \theta_0$, we can re-write the equations of motion as,

$$\begin{bmatrix} M & 0 \\ 0 & J \end{bmatrix} \begin{Bmatrix} \ddot{z}'_g \\ \ddot{\theta}' \end{Bmatrix} + \begin{bmatrix} c_{11} & c_{21} \\ c_{21} & c_{22} \end{bmatrix} \begin{Bmatrix} \dot{z}'_g \\ \dot{\theta}' \end{Bmatrix} + \begin{bmatrix} k_{11} & k_{21} \\ k_{21} & k_{22} \end{bmatrix} \begin{Bmatrix} z'_g \\ \theta' \end{Bmatrix} = \begin{Bmatrix} F_c(z_p) \\ -\frac{1}{2}b\mu F_{cr}(z_p) + d_h F_c(z_p) \end{Bmatrix} \quad (4)$$

The total energy of the air bearing, slider and suspension system, without considering the elastic contact energy, can be expressed as,

$$E = \frac{1}{2}m\dot{z}_p^2 + \frac{1}{2}m\dot{\theta}^2 + \frac{1}{2}k(z_g - z_{g0})^2 + k_{f0}z_{f0}^2 \left[\frac{z_{f0}}{z_f} - \ln\left(\frac{z_{f0}}{z_f}\right) - 1 \right] + k_{r0}z_{r0}^2 \left[\frac{z_{r0}}{z_r} - \ln\left(\frac{z_{r0}}{z_r}\right) - 1 \right] \quad (5)$$

The same parameter values as used in section 3.3 of [1], which are shown in Table 6.2, are used in the simulation here. The parameter d_l used in the air bearing model is not discussed in [1]. With the no-fly-zone condition, d_l can be set to 0.3 nm; or d_l is set to be equal to d_s [6], which means that the air bearing is lost when the separation is less than the touch-down flying height. We use both of these values in the following simulations.

The 4th order Runger-Kutta method is used to solve the equations of motion as in [1]. If $d_l = 0.3$ nm is set, the time history of the slider dynamics of a 7 nm slider with an initial condition of $FH = 250$ nm and $\theta = 0$ μ rad is shown in Figure 6.10 (a). It is obvious that the slider's vibration is damped quickly and the slider achieves a steady state, which is the same as its static state. If $d_l = d_s$, the time history of the slider's dynamics with the same initial conditions is shown in Figure 6.10 (b). It is seen that the slider's dynamics doesn't change with d_l . The slider's vibration is still damped out and the slider achieves its steady state quickly. The straight black line in the FH plot is the d_l line. In both cases the spacing at the rear air bearing center is always above d_l .

Figure 6.11 shows the simulation results with the parameter values in Table 6.2 except that the friction coefficient μ is changed to 2.0. It is seen that the slider's vibration is again damped out quickly. The increase in friction force has no effect on this 7-nm flying slider.

Figure 6.12 shows the simulation results with the parameter values in Table 6.2 except that the maximum meniscus force f_m is changed to 50 mN. When $d_l=0.3$ nm, the slider's vibration is damped out quickly and the slider attains a contact steady state. The FH of the steady state is 1.6 nm and the pitch angle is 94.2 μ rad. The slider has a lower FH and higher pitch angle than previously due to the large adhesion force of 50 mN. But the slider doesn't bounce continuously on the disk. When $d_l = d_s$, the numerical calculation doesn't converge even with the time step as small as 10^{-9} s. The spacing at the rear air bearing center is sometimes less than d_s at the beginning of the vertical bouncing. This causes a corresponding sharp change of the rear air bearing stiffness from a positive value to zero. This abrupt change in the rear air bearing stiffness causes the divergence of the calculation and produces some complex values. These complex values in the simulation result in negative values of system energy, which is shown in Figure 6.12 (b).

Figure 6.13 shows the simulation results with the parameter values in Table 6.2 except that the take-off FH is set to 8 nm, which means that the static flying without considering contact and adhesion is below the take-off FH. In the steady state the slider contacts the disk, which is shown from the non-zero contact force and non-zero system energy. In both cases of $d_l=0.3$ nm and $d_l=d_s$, the FH of the steady state is 3.8 nm and the pitch angle is 94.2 μ rad.

Figure 6.14 shows the simulation results with the parameter values in Table 6.2 except that the air bearing damping ratios are changed from 0.01 to 0.002. If $d_l=0.3$ nm,

the slider eventually obtains a steady state. If d_l is set to be d_s , initially the spacing at the rear air bearing center becomes less than d_l , the system energy becomes negative, but the slider goes to its steady state. The steady states in both cases are the same as the slider's static state. The low air bearing damping ratios only cause a slow decay of the bouncing vibration.

No continuous bouncing vibrations are observed in the simulations with a 7 nm slider. Now we turn to sliders with even lower FHs – a 4 nm FH slider and a 3 nm FH slider. Here d_l is set to be d_s , the air bearing damping ratios are kept at 0.002, but the initial FH is varied. The simulation results are listed in Table 6.3. In some cases the numerical solution does not converge, i.e. the numerical scheme does not produce the same result as the time step size is reduced from 10^{-8} s to 10^{-9} s. However, it is seen that none of them show a slider with a continuous bouncing vibration. If the air bearing damping ratios are changed back to the default value 0.01, all of the numerical calculations converge and the slider achieves a steady state in all of the cases with different initial FH.

As a summary of the above simulations with a simplified air bearing model and a simplified contact and adhesion model, no continuous bouncing vibration of the type shown in Section 3.3 of [1] is obtained. The bouncing vibration can always be damped out and the slider achieves a steady state on a flat disk without micro-waviness. This is in agreement with the results we obtained using the CML air bearing contact model with a smooth disk.

6.5 Conclusions

Three different nonlinear slider dynamics models are used for the numerical analysis of the bouncing vibration of an air bearing slider in near or partial contact with

the disk. In these three slider dynamics models, the air bearing with contact is modeled either using the generalized Reynolds equation modified with the Fukui-Kaneko slip correction and a new second order slip correction for the contact situation, or using nonlinear air bearing springs. The contact and adhesion between the slider and the disk are considered either using an elastic contact model and an improved intermolecular adhesion model, respectively, or using the Ono-Yamane [1] multi-asperity contact and adhesion model. The contact friction is calculated using Coulomb's law. All of the simulation results show that the slider's bouncing vibration is a forced vibration caused by the micro-waviness and roughness. The disk surface micro-waviness and roughness, which move into the head disk interface (HDI) as the disk rotates, excite the bouncing vibration of the partial-contact slider. The contact, adhesion and friction between the slider and the disk are not the direct causes of the slider's bouncing vibration, since none of the simulations predict bouncing in the absence of a moving rough disk surface. However, the contact and adhesion affect the bouncing amplitude of a partial-contact slider, as analyzed in [7]. So in order to design a partial-contact slider with small bouncing, the disk surface, slider-disk contact and adhesion need to be systematically modeled in the simulation process.

References

- [1] K. Ono and M. Yamane, "Improved Analysis of Unstable Bouncing Vibration and Stabilizing Design of Flying Head Slider in Near-Contact Region," *ASME Jour. Tribol.*, vol. 129, pp. 65-74, 2007.
- [2] S. Fukui and R. Kaneko, "Analysis of Ultra-Thin Gas Film Lubrication Based on Linearized Boltzmann Equation: First Report-Derivation of a Generalized Lubrication

- Equation Including Thermal Creep Flow,” *ASME Jour. Tribol.*, vol. 110, pp. 253–262, 1988.
- [3] R. Ambekar, V. Gupta and D. B. Bogy, “Experimental and Numerical Investigation of Dynamic Instability in the Head Disk Interface at Proximity,” *ASME Jour. Tribol.*, vol. 127, pp. 530-536, 2005.
- [4] S. C. Lee and A. A. Polycarpou, “Microtribodynamics of Pseudo-Contacting Head-Disk Interface Intended for 1 Tbit/in²,” *IEEE Trans. Magn.*, vol. 41(2), pp. 812-818, 2005.
- [5] J. Y. Juang, D. Chen and D. B. Bogy, “Alternate Air Bearing Slider Designs for Areal Density of 1 Tbit/in²,” *IEEE Trans. Magn.*, vol. 42(2), pp. 241-247, 2006.
- [6] K. Ono and M. Yamane, “Experimental and Theoretical Investigation of Bouncing Vibrations of a Flying Head Slider in the Near-Contact Region,” *ASME Jour. Tribol.*, vol. 129, pp. 246-255, 2007
- [7] D. Chen and D. B. Bogy, “Dynamics of Partial Contact Head Disk Interface,” *IEEE Trans. Magn.*, vol. 43(6), pp. 2220-2222, 2007

Table 6.1 Parameter values used in the multi-asperity contact and adhesion model for the slider-disk contact (upper asterisks denote the default values used in the simulations)

Maximum meniscus force (f_m)	5.0 mN, 10.0 mN*, 20.0 mN
Take-off FH (d_e)	4.0 nm*, 5.5 nm, 8.0 nm
Friction coefficient (μ)	0.5, 1*, 2

Table 6.2 Parameter values used for 2-DOF slider dynamic simulations

slider width (b)	0.3 mm
slider mass (M)	1.59 mg
slider's moment of inertia (J)	$2.19 \times 10^{-13} \text{ kg} \cdot \text{m}^2$
Distance between the mass center and the contact pad (d_h)	-0.550 nm
Distance between the mass center and the front air bearing center (d_f)	0.250 nm
Distance between the mass center and the rear air bearing center (d_r)	-0.525 nm
Suspension normal stiffness (k)	4.9 N/m
Suspension angular stiffness (k_θ)	$1.6 \times 10^{-4} \text{ N} \cdot \text{m}/\text{rad}$
Suspension normal damping ratio (ζ)	0.002
Suspension angular damping ratio (ζ_θ)	0.002
Static front air bearing stiffness (k_{f0})	$5.0 \times 10^5 \text{ N} \cdot \text{m}$
Static rear air bearing stiffness (k_{r0})	$1.3 \times 10^6 \text{ N} \cdot \text{m}$
Front air bearing damping ratio (ζ_f)	0.01
Rear air bearing damping ratio (ζ_r)	0.01
Friction coefficient (μ)	1.0
Contact stiffness (k_c)	$5.0 \times 10^6 \text{ N} \cdot \text{m}$
Real contact force at the beginning of contact (f_{c0})	5.0 mN
Maximum meniscus force (f_m)	10.0 mN
Touch-down FH (d_s)	3.0 nm
Take-off FH (d_e)	4.0 nm
Static pitch angle (θ_0)	90 μrad
Static FH	7.0 nm
Initial excitation	250 nm FH and 0 μrad pitch angle

Table 6.3 Simulation results of a 4 nm slider and a 3 nm slider with $\zeta_f = \zeta_r = 0.002$ and $d_l = d_s$

	Initial FH and pitch angle	Does the numerical calculation converge?	Does the slider achieve a steady state finally?
4 nm slider	100 nm and 0 μ rad	Yes	Yes
	50 nm and 0 μ rad	Yes	Yes
	10 nm and 0 μ rad	No	The FH becomes several microns.
3 nm slider	100 nm and 0 μ rad	Yes	Yes
	50 nm and 0 μ rad	Yes	Yes
	10 nm and 0 μ rad	No	Yes

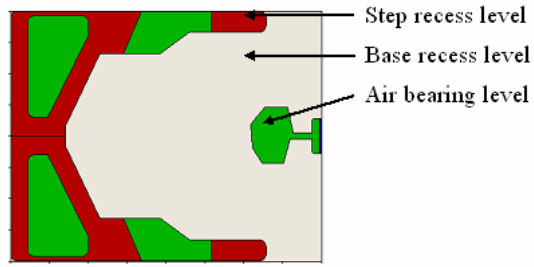
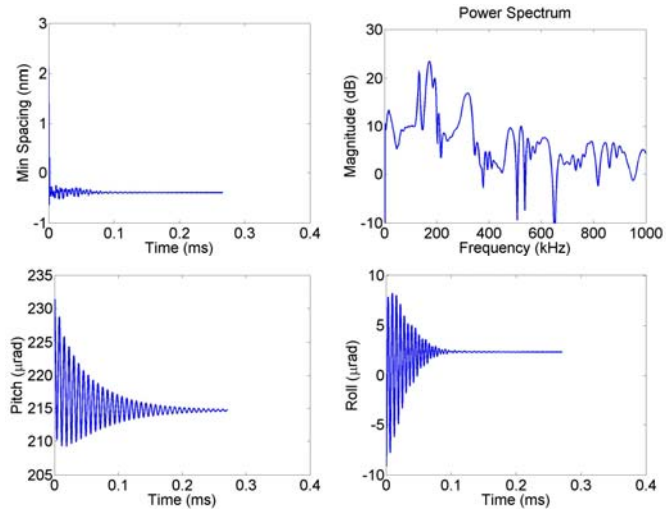
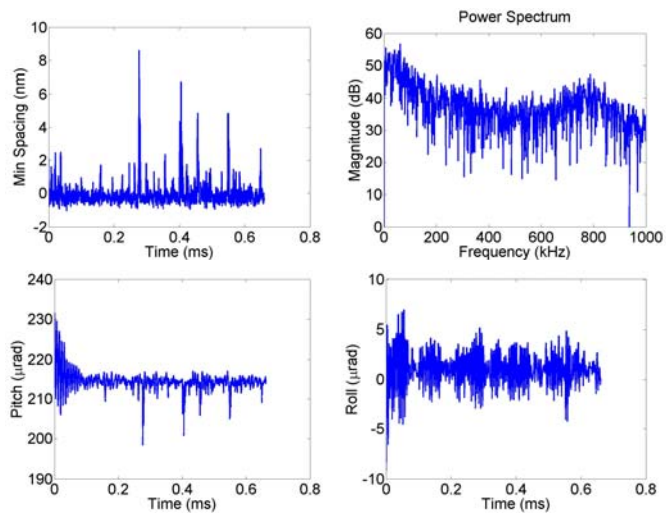


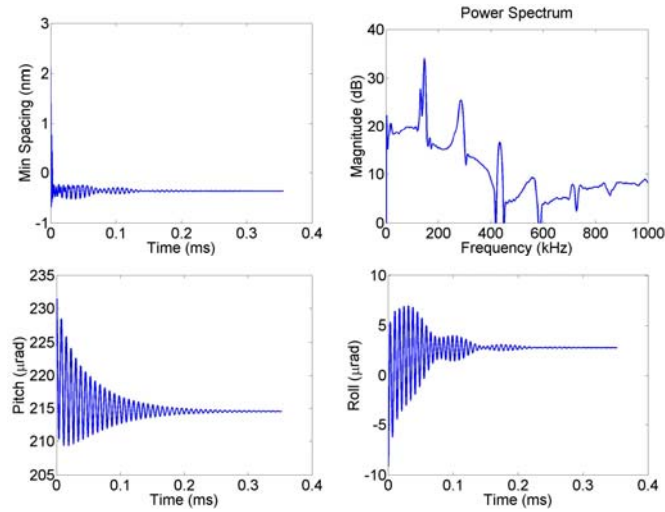
Fig.6.1. Air bearing surface design of a micro-trailing pad slider



(a) Case I



(b) Case II



(c) Case III

Fig.6.2. Time histories of the minimum spacing, the pitch, the roll and the power spectra of the minimum spacing of case I (the micro trailing pad slider on the ideally flat disk surface), case II (the micro trailing pad slider on a rough disk surface with moving roughness within the HDI) and case III (the micro trailing pad slider on a rough disk surface with stationary roughness within the HDI)

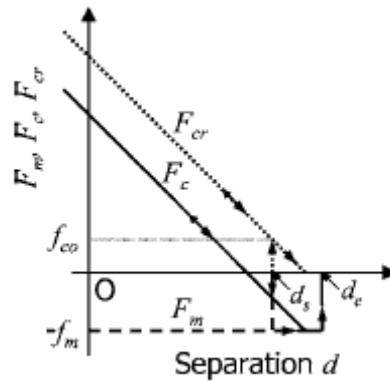


Fig.6.3. Simplified characteristic model of real contact force, adhesion force and contact force as functions of separation [1]

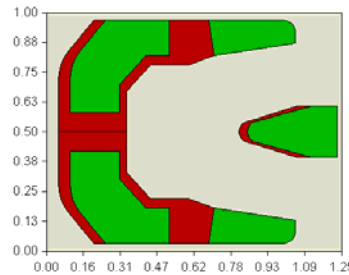


Fig.6.4. Air bearing surface design of the CML slider used in the CML 2-DOF slider dynamic simulation

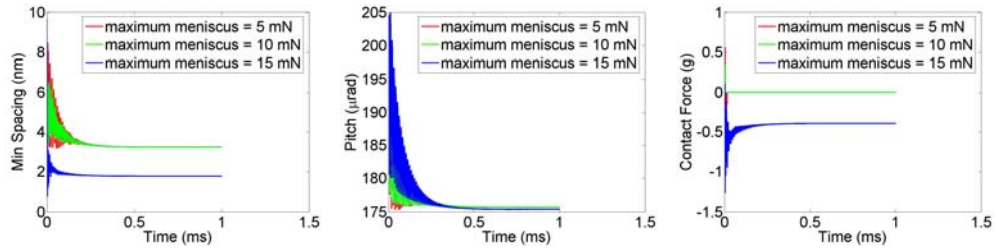


Fig.6.5. Time history of the slider dynamics with different maximum meniscus force f_m

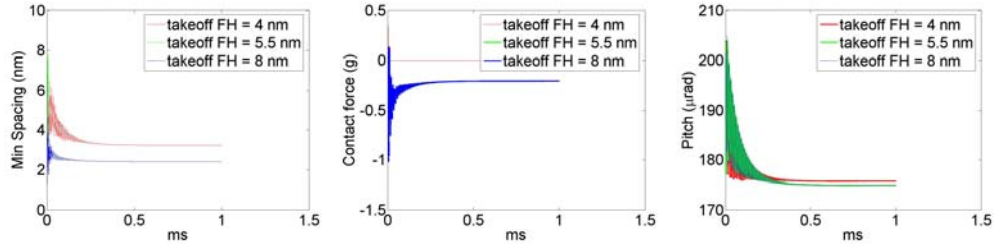


Fig.6.6. Time history of the slider dynamics with different take-off FH d_e

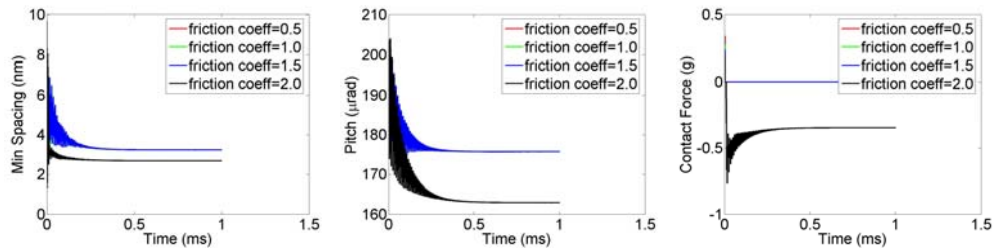


Fig.6.7. Time history of the slider dynamics with the different friction coefficient μ

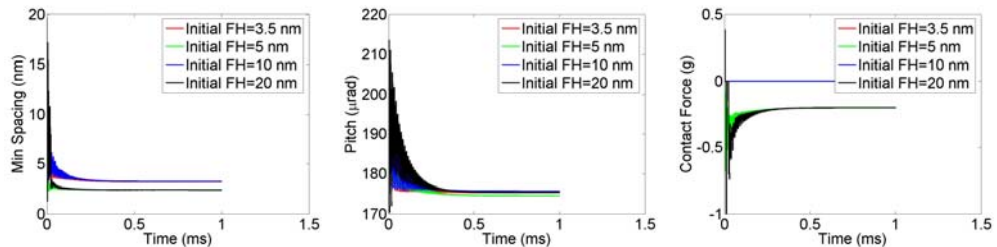


Fig.6.8. Time history of the slider dynamics with different initial FH

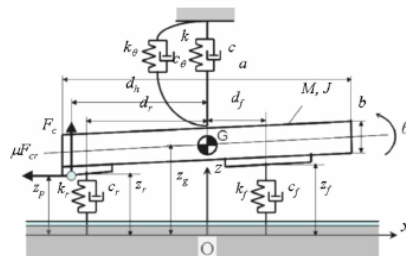
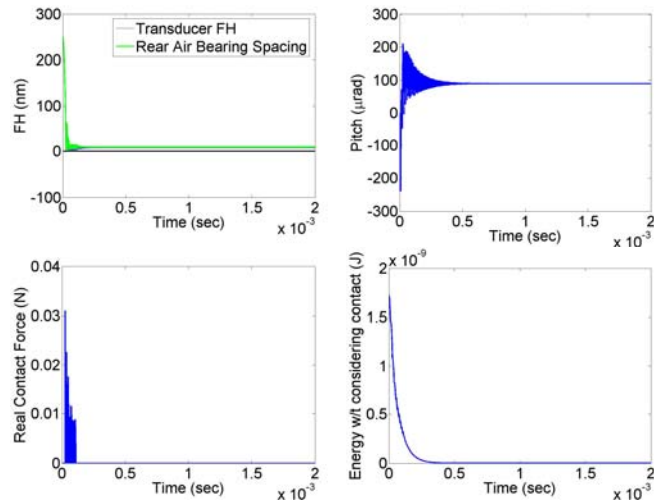
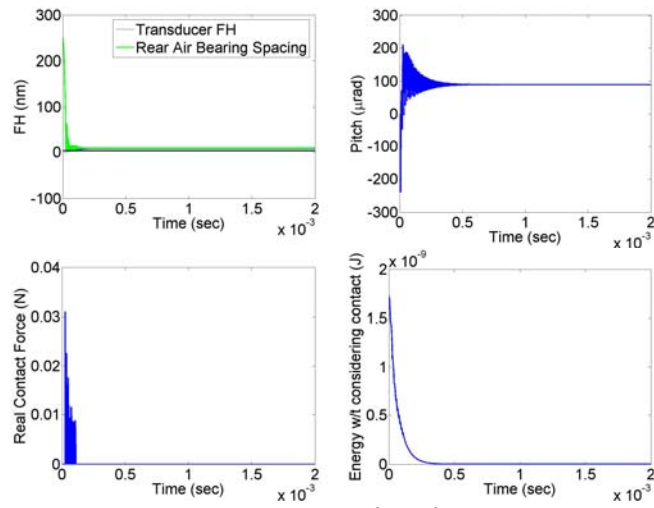


Fig.6.9. 2-DOF slider model by Ono and Yamane [1]

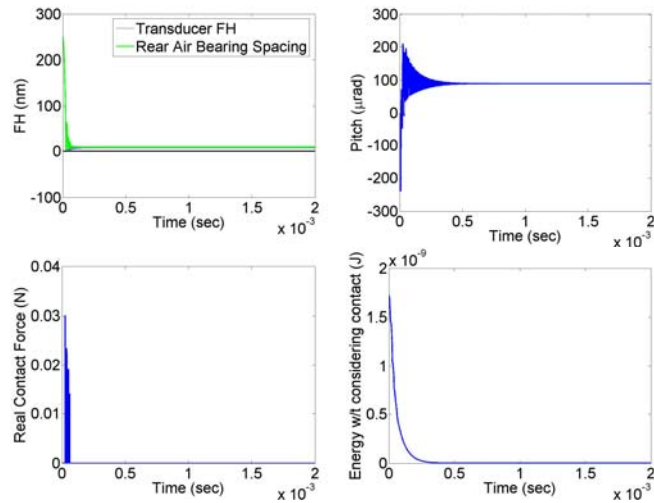


(a) $d_1 = 0.3 \text{ nm}$

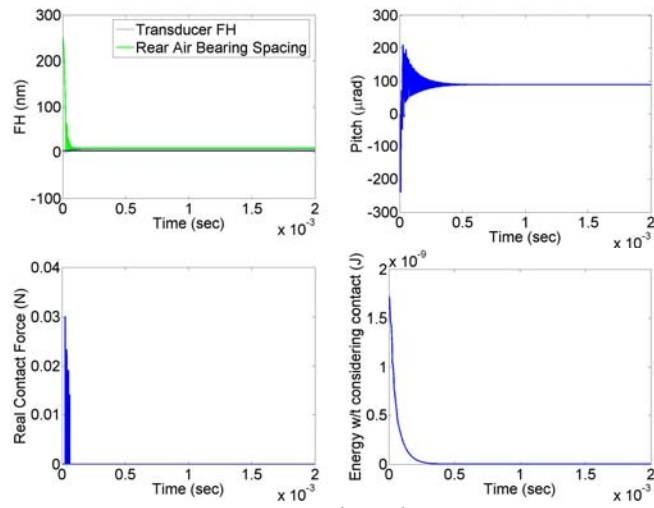


(b) $d_1 = d_s$

Fig.6.10. Time history of the 2-DOF slider model with the parameter values shown in Table 6.2

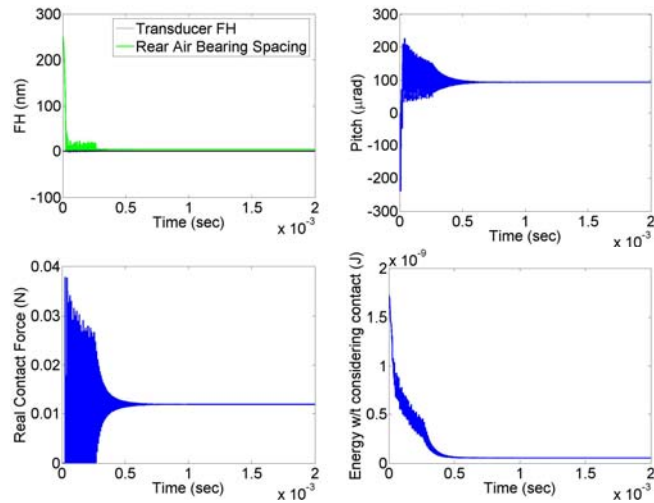


(a) $d_l = 0.3 \text{ nm}$

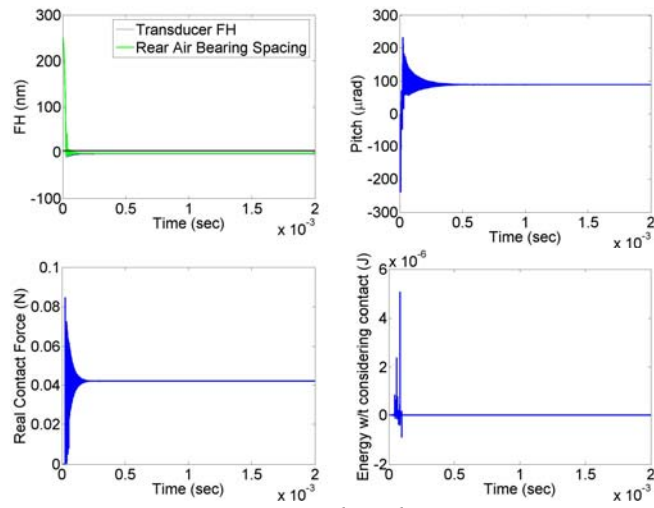


(b) $d_l = d_s$

Fig.6.11. Time history of the 2-DOF slider model with the parameter values shown in Table 6.2 except that $\mu = 2.0$

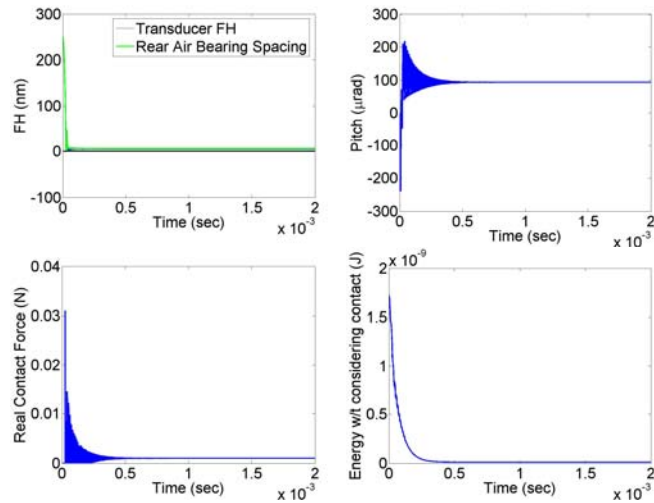


(a) $d_l = 0.3 \text{ nm}$

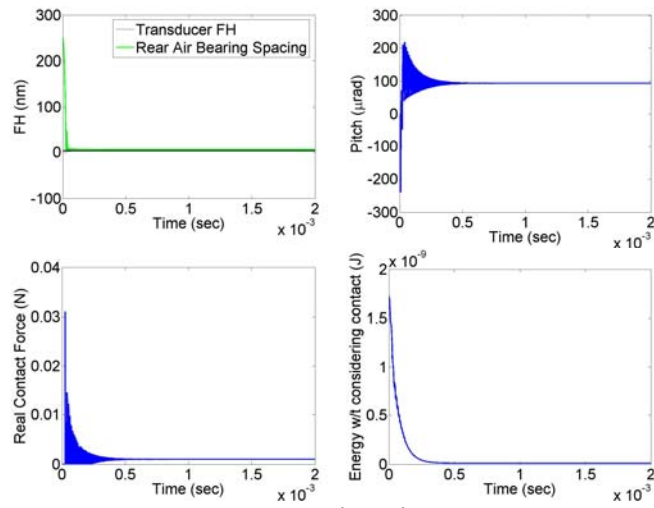


(b) $d_l = d_s$

Fig.6.12. Time history of the 2-DOF slider model with the parameter values shown in Table 6.2 except that $f_m = 50 \text{ mN}$.

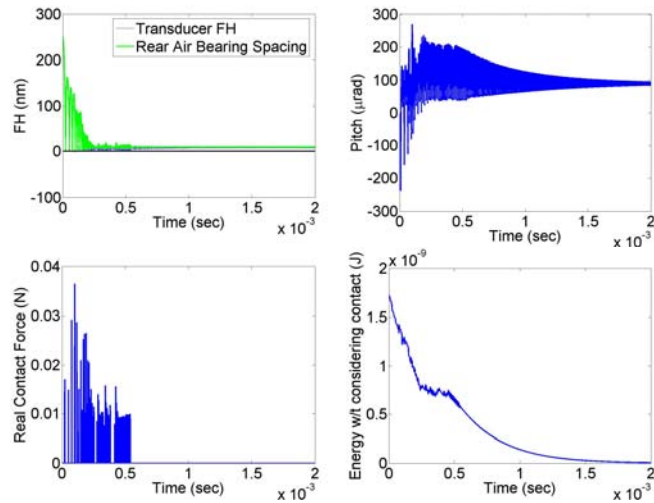


(a) $d_l = 0.3 \text{ nm}$

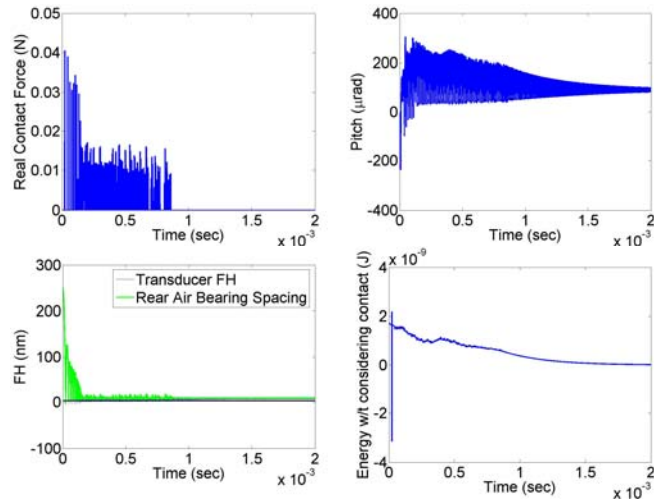


(b) $d_l = d_s$

Fig.6.13. Time history of the 2-DOF slider model with the parameter values shown in Table 6.2 except that $d_e = 8 \text{ nm}$



(a) $d_l = 0.3 \text{ nm}$



(b) $d_l = d_s$

Fig.6.14. Time history of the 2-DOF slider model with the parameter values shown in Table 6.2 except that $\zeta_f = \zeta_r = 0.002$

Chapter 7 Simulation of Static Flying Attitude with Different Heat Transfer Models for a Flying Height Control Slider with Thermal Protrusion

The air bearing cooling effect and viscous heating effect are considered in the numerical simulation of an air bearing slider with its flying height controlled by thermal protrusion, which is conventionally called thermal flying height control (TFC) or dynamic flying height (DFH). The simulation results show that the air bearing cooling is dominant compared with the viscous heating. Different models for the air bearing cooling, i.e. the heat conduction at the slider's air bearing surface (ABS), are also used and compared in the numerical simulations. It is found that all of these models, including a recent one considering the dependence of the air molecule's mean free path on the ambient temperature, give very close simulation results of the slider's static flying attitude. The difference is less than 10% of the result obtained with Chen's model [1], which is used in the current CML program.

7.1 Introduction

The thermal flying height control (TFC) - dynamic flying height (DFH) – technique, as presented in the patent by Meyer et al. [2], is widely used in current hard drives to lower the slider's flying height. This advantageous technique makes use of a resistance

heating element near the read/write transducer. When a current is applied through the heating element, it undergoes local thermal expansion and forms a localized thermal protrusion near the trailing edge center of the slider close to the read/write transducer. The thermal protrusion reduces the flying height very locally at the transducer. In this way the transducer flying height becomes adjustable. This technique provides control that can compensate for the static flying height (FH) loss and reduce the likelihood of head-disk contact for an air bearing slider. Additionally, this technique has the potential of achieving a partial-contact head disk interface (HDI). The controllable contact area created by the thermal protrusion at the transducer helps maintain a very light contact between the slider and the disk, while the rest of the air bearing surface (ABS) remains undeformed and flies at a safe distance from the disk.

For a slider with thermal protrusion, the cooling effect of the air bearing was first analyzed by Juang et al. [3]. The coupling problem between the thermal protrusion and the air bearing was numerically analyzed using a loop composed of a static Reynolds equation solver for the air bearing and a finite element analysis for the thermal protrusion. It was shown that the heat transfer from the slider to the disk through the air bearing film has a considerable effect on the flying height reduction efficiency. The work in that paper used a HDI heat transfer model developed by Chen and Bogy [1]. The viscous dissipation was neglected in that simulation, since Chen's model concluded that on the ABS the viscous dissipation is about 1-2 orders of magnitude less than the heat conduction. An independent work done by Ju [4] produced another heat transfer model with different viscous dissipation. Recently Zhou et al. [6] and Shen et al. [7] proposed two different new HDI heat transfer models. As different heat transfer models for head disk interface are proposed, however, a question arises as to how much difference is caused in the static

flying attitude with the different heat transfer models applied in the simulation. In this chapter, this question is addressed using both pico and femto air bearing slider designs. The simulation results show that the viscous dissipation does not affect the static flying attitude even when the FH is less than 2 nm. It is also found that the different models for heat conduction on the ABS give very close simulation results for the slider's static flying attitude. The relative difference is less than 10% in the static transducer flying height and less than 1% in the pitch angle, when compared with Chen's model [1].

7.2 Heat transfer models for the head-disk interface

In the numerical flying attitude analysis for a slider with thermal protrusion carried out by Juang et al. [3], the HDI heat transfer model developed by Chen and Bogy [1] is used for the heat conduction on the ABS. In fact, Chen's model originates from the HDI heat transfer model by Zhang and Bogy [5]. Zhang's model and Chen's model both use the velocity slip and temperature jump theory at the boundary of the air bearing. Both models have shown that the heat flux on the ABS has two contributions. One is the heat conduction, which transfers heat from the slider to the air bearing when the ABS has a higher temperature than the disk surface; the other is the viscous dissipation due to the air flow within the HDI. Both models have the same expression for the heat conduction, the same expression for the viscous dissipation due to the Couette flow, but different expressions for viscous dissipation contributed by the Poiseuille flow. For a simplified situation with disk velocity U in the slider length direction (i.e. x-direction) and zero disk velocity in the slider width direction (i.e. y-direction), the expression for heat flux on the ABS is,

$$q_{ABS} = q_{conduction} + q_{viscous} = q_{conduction} + q_{Couette} + q_{Poiseuille},$$

$$\text{where } q_{conduction} = -k \frac{T_s - T_d}{h + 2b\lambda} \text{ and } q_{Couette} = \frac{\mu U^2 h}{2(h + 2b\lambda)^2}.$$

Zhang's model has

$$q_{Poiseuille} = -\frac{Uh^3}{6(h + 2b\lambda)(h + 2a\lambda)} \frac{\partial p}{\partial x} + \frac{h^3}{24\mu} \left[\left(\frac{\partial p}{\partial x} \right)^2 + \left(\frac{\partial p}{\partial y} \right)^2 \right],$$

Chen's model has

$$q_{Poiseuille} = -\frac{Uh(ah\lambda + bh\lambda + 2ab\lambda^2)}{6(h + 2b\lambda)(h + 2a\lambda)} \frac{\partial p}{\partial x} + \frac{ah^2\lambda}{4\mu} \left[\left(\frac{\partial p}{\partial x} \right)^2 + \left(\frac{\partial p}{\partial y} \right)^2 \right].$$

In the above heat flux expressions, k is the thermal conductivity of air; μ is the viscosity of air; T_s and T_d are the temperatures of the slider and the disk, respectively; h is the local slider-disk gap; λ is the mean free path of air; p is the local air bearing pressure; $b = 2 \frac{(2 - \sigma_T)}{\sigma_T} \frac{\gamma}{(\gamma + 1)} \frac{1}{P_r}$, where σ_T is the thermal accommodation coefficient; P_r

is the Prandtl number of air, γ is the ratio of the specific heat; $a = \frac{2 - \alpha}{\alpha}$, where α is the momentum accommodation coefficient. In fact the first term in the expression of $q_{Poiseuille}$ represents the coupling of Poiseuille flow and Couette flow. That term is included in the heat flux contributed by the Poiseuille flow for a notation simplification in this chapter.

Zhang's model and Chen's model both show that the heat flux on the ABS is dominated by the heat conduction while viscous dissipation is only a second order effect. Because of this, only the heat conduction on the ABS, i.e. the cooling effect of the air bearing, is considered in the static flying height simulation by Juang et al. [3].

Ju [4] proposed another heat transfer model for the HDI. The heat conduction part is also based on the temperature jump theory, which makes it have a similar expression to those shown in Zhang's and Chen's models. In fact the heat flux due to conduction in Ju's model is just the corresponding term in Zhang's and Chen's models with surface thermal accommodation coefficient σ_T equal to 1. However, the viscous dissipation due to the

Couette flow in Ju's model is based on an approximate solution of the Boltzmann transport equation and the expression is different from the term in Zhang's and Chen's models. Also the viscous dissipation contributed by the Poiseuille flow is not included in Ju's model. The complete expression for heat flux on the ABS in Ju's model is,

$$q_{ABS} = q_{conduction} + q_{viscous} = -k \frac{T_s - T_d}{h + 2b\lambda} + \frac{1}{8} \rho U^2 \sqrt{\frac{8RT}{\pi}} \frac{2\lambda}{h + 2\lambda},$$

where ρ is the air density and T is the air temperature.

Based on Zhang's and Chen's models, Zhou et al. [6] took the change of the air molecule's mean free path caused by a temperature change into consideration and proposed a generalized heat transfer model. This model shows that the heat flux due to conduction varies significantly when the mean free path of the air molecules changes, giving

$$q_{ABS} = q_{conduction} + q_{viscous} = -k \frac{T_s - T_d}{h + 2b\lambda} + q_{viscous},$$

where $\lambda = \xi \left(\frac{T}{T_0}\right)^{\omega+0.5} \frac{p_0}{p} \lambda_0$ with parameters ξ and ω determined by the model used for the mean free path of air. For example, $\xi=1$ and $\omega=0.5$ for the hard sphere model; $\xi=0.8244$ and $\omega=0.75$ for the variable soft sphere model; $\xi=0.75$ and $\omega=1$ for the variable hard sphere model. Experimental data provide $\xi=0.80\sim 0.85$ and $\omega=0.75$ for an air film [6], which indicates that the variable soft sphere model is applicable to air films.

Different from these models based the velocity slip and temperature jump theory, a HDI heat transfer model based on the linearized Boltzmann equation was recently proposed by Shen and Chen [7] This model gives a heat conduction flux close to those obtained in Zhang's model, Chen's model and Ju's model, but it has different viscous dissipations. In this model the relation between the viscous heating due to the Couette

flow and the inverse Knudsen number is quite different from that in Zhang's and Chen's models, but close to that obtained from Ju's model. In both Ju's model and Shen's model the viscous dissipation due to the Couette flow asymptotically approaches a constant as the inverse Knudsen number decreases to 0.01, while in Zhang's and Chen's models the Couette-flow-caused viscous dissipation reduces almost to zero as the inverse Knudsen number goes to 0.01. Also the viscous dissipation contributed by the Poiseuille flow obtained from Shen's model and from Zhang's and Chen's models are different. Presumably Shen's model is more accurate for the heat transfer with small inverse Knudsen number, since it is directly derived from the linearized Boltzmann equation. However, the expression for heat flux given by this model has complex integrations with respect to molecule velocities. It is not applicable to the engineering simulation of the slider's flying attitude with adjustable thermal protrusion.

7.3 Simulation of air bearing sliders with thermal protrusion

This chapter is focused on the numerical analysis of the air bearing cooling effect and the viscous heating effect on the slider's static flying attitude, and numerical comparisons of different static flying attitudes obtained when different HDI heat transfer models are applied. First, Ju's model is used for analysis of the effect of viscous heating on the slider's static attitude, since the heat conduction term and the viscous heating term in Ju's model are both validated by Shen's model based on the linearized Boltzmann equation. Second, the slider's static simulation results obtained with Zhang's and Chen's models, Ju's model and Zhou's model are compared to analyze the difference caused by different heat conduction models, which are applied for the air bearing cooling.

In the numerical analysis, an INSIC pico slider [3] and a commercial femto slider are

used. The pico slider's ABS is shown in Figure 7.1 and its heating-power-off static flying attitude is shown in Table 1. The static flying height of a slider with thermal protrusion is obtained using the loop shown in [3]. This loop contains a Reynolds equation solver for the steady state of an air bearing slider and a finite element analysis program to calculate the thermal protrusion with inside heating, heat convection on non-air-bearing surfaces and complex heat transfer at the ABS. In this chapter the CML static air bearing program is used to solve the generalized Reynolds lubrication equation for the slider's static flying attitude. In the iteration the ABS with updated thermal protrusion is input into the CML program. The finite element model for a pico slider with a GMR head and a micro heater developed in [3] is used here for the protrusion calculation by an ANSYS program. The heat conduction at the ABS, i.e. air bearing cooling, can be treated as heat convection at the ABS with given convection coefficients in ANSYS. Since the boundary conditions of heat flux and convection can not be applied to the same boundary in ANSYS, the viscous dissipation flux is treated as surface heating on the ABS, which has a heat generation rate twice the viscous heating flux.

The commercial femto slider's ABS is shown in Figure 7.2. Due to the lack of an accurate ANSYS model for the read/write transducer, heater and other components in this femto slider, the structures of the read/write transducer and micro heater used in [3] are scaled down and adopted in the simulation of this femto slider. The same loop is used to obtain the femto slider's static flying attitude with different HDI heat transfer models.

7.4 Simulation results for static flying attitudes

7.4.1 Pico slider

a) Viscous heating versus air bearing cooling

Ju's model is applied in the loop to analyze the effect of viscous dissipation on the slider's static flying attitude. Table 7.2 shows the simulation results for 40 mW, 80 mW and 120 mW heating power using Ju's model with and without the consideration of viscous dissipation contributed by the Couette flow. It is obvious that the effect is negligible, even when the flying height is below 2 nm. Figure 7.3 shows the corresponding temperature and heat flux at the ABS, and it is seen that the largest difference is less than 1%. So the viscous dissipation contributed by the Couette flow has negligible effect on the slider's static flying attitude and the heat transfer on the ABS for this INSIC pico slider.

b) Heat conduction in Ju's model versus Zhang's and Chen's models

The only difference between the heat conduction part in Ju's model and that in Zhang's and Chen's models is that the surface thermal accommodation coefficient is 1.0 in Ju's model, while it is a parameter in Zhang's and Chen's models. For the slider and disk surface, the thermal accommodation coefficient is chosen as 0.9 in Zhang's and Chen's models. Here simulations are carried out with three values of heating powers, 40 mW, 80 mW and 120 mW. Table 7.2 lists the slider's static flying attitude obtained with Ju's model and with Zhang's and Chen's models. Figure 7.4 graphically shows the comparison of static flying attitudes obtained using these two types of models neglecting the viscous heating. The largest relative difference in static transducer FH and pitch angle is less than 10%. The difference in static roll angle is less than 1 μ rad and thus negligible, although the difference is large compared with 1 micron radian level roll angle. Figure 7.5 shows the temperature and heat flux on the ABS. The largest relative difference is also less than 10%. This difference is larger than the difference between the flying attitude results with and without considering the Couette-flow-caused viscous heating in

Ju's model. It indicates that the surface thermal accommodation coefficient has a larger effect than the Couette-flow-caused viscous heating in the HDI heat transfer.

c) Heat conduction in Zhou's model versus Zhang's and Chen's models

The only difference between Zhou's model and Zhang's and Chen's models is that the dependence of mean free path of the air molecules on the ambient temperature is considered in Zhou's model. Here simulations are carried out with different ambient temperatures. The air parameters used in the models, including the ratio of the specific heat, Prandtl number and thermal conductivity, change as the air temperature changes. Table 7.3 lists those parameter values for the air temperatures of 0°C, 25°C, 50°C to 75°C. Using those values in Zhou's model or Zhang's and Chen's models, the slider's static flying attitudes are obtained and listed in Table 7.4 at the ambient temperatures of 0°C, 25°C, 50°C to 75°C, when the heat power is 40 mW and 80 mW, respectively. It is obvious that as the ambient temperature increases, the air cooling effect on the slider surface, including the ABS and non-ABS, decreases if the convection and conduction coefficients do not change. This leads to an increase in the slider's temperature and thermal protrusion at the trailing edge center. Increased thermal protrusion causes more flying height loss. Figures 6 and 7 graphically show the difference between the simulation results obtained from Zhou's model and from Zhang's and Chen's models when the heating power is 40 mW and 80 mW, respectively. The largest relative differences in static transducer FH and pitch angle are less than 10%. Although the relative difference in static roll angle is larger than 10%, the absolute difference is still less than 1 μrad and is negligible.

It was shown in [6] that the mean free path of air increases as the air temperature

increases. So for the HDI a large difference in heat transfer between Zhou's model and Zhang's and Chen's models is expected to occur at high temperatures. Figure 7.8 shows the temperature and heat conduction on the ABS at the slider's static state for the cases at 75°C ambient temperature, obtained using Zhou's model and Zhang's and Chen's models, respectively. The maximum relative difference is less than 5%.

7.4.2 Femto slider

A heating power of 200 mW is used in the simulation of the commercial femto slider, whose ABS is shown in Figure 7.2. Usually its working power is less than 200 mW. Table 7.5 lists the static flying attitudes of the femto slider with different heat transfer models. It is obvious that the flying attitudes obtained with Ju's model with and without considering Couette-flow-caused viscous heating, and Zhang's and Chen's models are almost the same. At the ambient temperature of 75°C, the static flying attitudes obtained with Zhou's model and Zhang's and Chen's models are also very close. The largest difference is no more than 2% when compared with the results obtained with Zhang's and Chen's models.

7.5 Conclusions

Numerical simulations for the static flying attitudes of sliders with thermal protrusion are carried out using different head-disk-interface heat transfer models. The air bearing cooling effect is dominant at the air bearing surface compared with the viscous heating due to the Couette flow. Since the viscous heating contributed by the Poiseuille flow is no larger than the viscous dissipation contributed by the Couette flow [7], it is expected that the entire viscous dissipation has a negligible effect on the slider's static flying attitude.

The change of surface thermal accommodation coefficient from 1.0 (used in Ju's

model [4]) to 0.9 (recommended in Zhang's and Ju's models [1, 5] for the slider and disk surfaces) causes less than a 10% change in static transducer flying height and pitch angle. The consideration of the dependence of the air molecule's mean free path on ambient temperature in Zhou's model gives a relative difference less than 10% in static transducer flying height and pitch angle when compared with Zhang's and Chen's models. Considering the dynamic flying height modulation of approximately 10% of the flying height, Zhang's model (or Chen's model), which is used in the current CML program for the air bearing cooling effect, is accurate enough for the static flying attitude simulation of an air bearing slider with thermal protrusion.

Reference

- [1] L. Chen, D. B. Bogy and B. Strom, "Thermal Dependence of MR Signal on Slider Flying State," *IEEE Trans. Magn.*, vol. 36, no. 5, pp. 2486-2489, 2000.
- [2] D. W. Meyer, P. E. Kupinski and J. C. Liu, "Slider with Temperature Responsive Transducer Positioning," U. S. Patent 5991113, Nov. 23, 1999.
- [3] J. Y. Juang, D. Chen and D. B. Bogy, "Alternate Air Bearing Slider Designs for Areal Density of 1 Tbit/in²," *IEEE Trans. Magn.*, vol. 42, pp. 241-246, 2006.
- [4] Y. S. Ju, "Thermal Conduction and Viscous Heating in Microscale Couette," *J. Heat Transfer*, vol.122, pp. 817-818, 2000
- [5] S. Zhang and D. B. Bogy, "A Heat Transfer Model for Thermal Fluctuation in a Thin Air Bearing," *Int. Jour. of Heat Mass Transfer*, vol. 42, pp. 1791-1800, 1997.
- [6] W. D. Zhou, B. Liu, S. K. Yu, W. Hua and C. H. Wong, "A Generalized Heat Transfer Model for Thin Film Bearings at Head-Disk Interface," *Applied Physics letters*, vol. 92, pp. 043109, 2008

[7] S. Shen and G. Chen, "A Kinetic Theory Analysis on the Heat Transfer in Hard Drive Air Bearing," *Jour. of Applied Physics*, vol. 103, pp. 054304, 2008

Table 7.1 Specification of the suspension used in the numerical analysis and corresponding static flying attitude of the pico slider (shown in Figure 7.1) with heating power off

Suspension	Suspension load: 1.5 gf Pitch torque: -6.4 $\mu\text{N}\cdot\text{m}$ Roll torque: 0.0 $\mu\text{N}\cdot\text{m}$ Pitch static attitude: 0.0 rad Roll static attitude: 0.0 rad
Static flying attitude	Transducer FH: 14.37 nm Pitch: 154.57 μrad Roll: 0.36 μrad

Table 7.2 Static flying attitudes of the pico slider (shown in Figure 7.1) obtained with and without the viscous heating contributed by the Couette flow

		Ju's Model		Zhang's and Chen's Models
Heating power		With viscous heating	Without viscous heating	
40mW	Transducer FH (nm)	8.51	8.51	8.35
	Pitch (μrad)	149.56	149.56	149.18
	Roll(μrad)	0.0679	0.0678	0.10
80 mW	Transducer FH (nm)	4.21	4.23	4.00
	Pitch (μrad)	143.94	144.00	143.30
	Roll (μrad)	-0.327	-0.244	-0.23
120 mW	Transducer FH (nm)	1.77	1.75	1.60
	Pitch (μrad)	137.18	137.19	136.07
	Roll (μrad)	-0.80	-0.83	-0.84

Table 7.3 Air parameters at different temperatures

Temperature	ratio of the specific heat γ	Prandtl number Pr	thermal conductivity k (W/m·K)
0 °C	1.401	0.713	0.02428
25 °C	1.400	0.707	0.02624
50 °C	1.399	0.701	0.02816
75 °C	1.398	0.697	0.03003

Table 7.4 Static flying attitudes of the pico slider (shown in Figure 7.1) obtained with Zhou's model and with Zhang's and Chen's models

Heating power	Ambient temperature	Flying attitude	Zhou's model	Zhang's and Chen's models
40 mW	0°C	Transducer FH (nm)	9.47	9.20
		Pitch (μrad)	148.91	148.41
		Roll (μrad)	0.079	-0.014
	25°C	Transducer FH (nm)	8.44	8.36
		Pitch (μrad)	149.49	149.21
		Roll (μrad)	0.036	0.011
	50°C	Transducer FH (nm)	7.31	7.22
		Pitch (μrad)	149.47	149.45
		Roll (μrad)	0.096	0.066
	75°C	Transducer FH (nm)	5.87	5.87
		Pitch (μrad)	148.48	148.60
		Roll (μrad)	0.011	0.096
80 mW	0°C	Transducer FH (nm)	5.08	4.76
		Pitch (μrad)	143.35	142.39
		Roll (μrad)	-0.26	-0.34
	25°C	Transducer FH (nm)	4.16	4.01
		Pitch (μrad)	143.85	143.39
		Roll (μrad)	-0.27	-0.23
	50°C	Transducer FH (nm)	3.36	3.28
		Pitch (μrad)	144.35	144.15
		Roll (μrad)	-0.36	-0.26
	75°C	Transducer FH (nm)	2.29	2.33
		Pitch (μrad)	143.18	143.21
		Roll (μrad)	-0.43	-0.34

Table 7.5 Static flying attitudes of the femto slider (shown in Figure 7.8) obtained with different HDI heat transfer models

		Ju's Model		Zhang's and Chen's Models	Zhou's model with 75°C	Zhang's and Chen's Models with 75°C
Heating power	Flying attitude	With viscous heating	Without viscous heating	Without viscous heating	Without viscous heating	Without viscous heating
200mW	Transducer FH (nm)	9.15	9.11	8.99	7.68	7.71
	Pitch (μ rad)	103.65	103.81	103.26	103.45	103.70
	Roll(μ rad)	-25.76	-25.58	-25.71	-26.15	-26.08

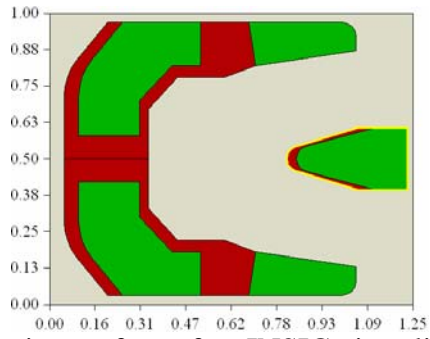


Fig.7.1. Air bearing surface of an INSIC pico slider (unit: mm).

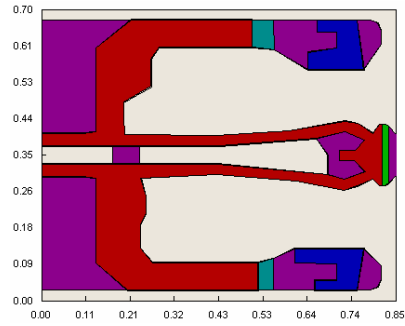
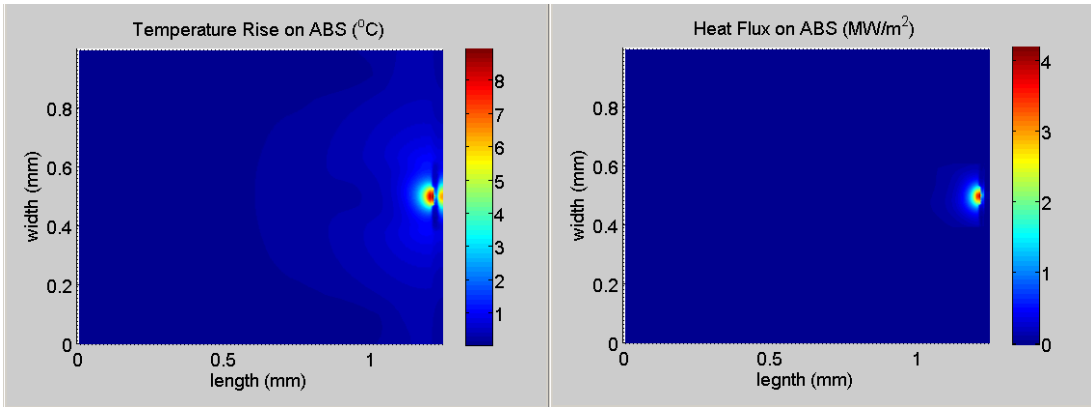
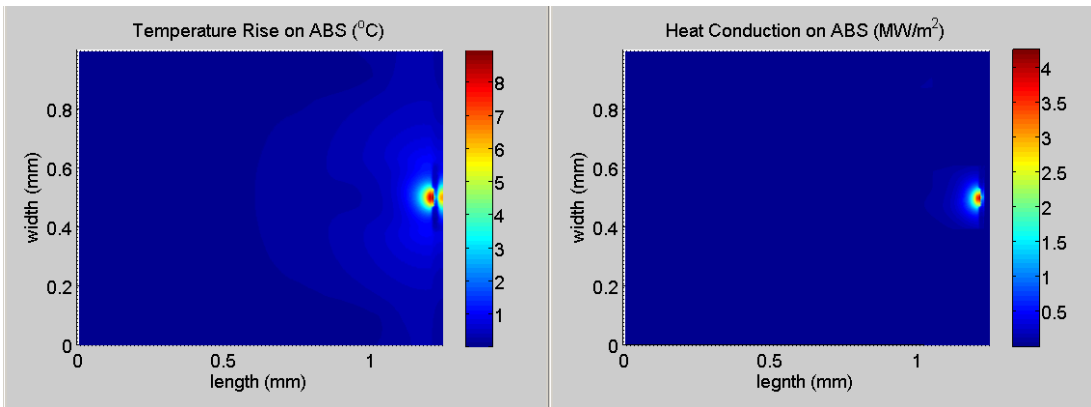


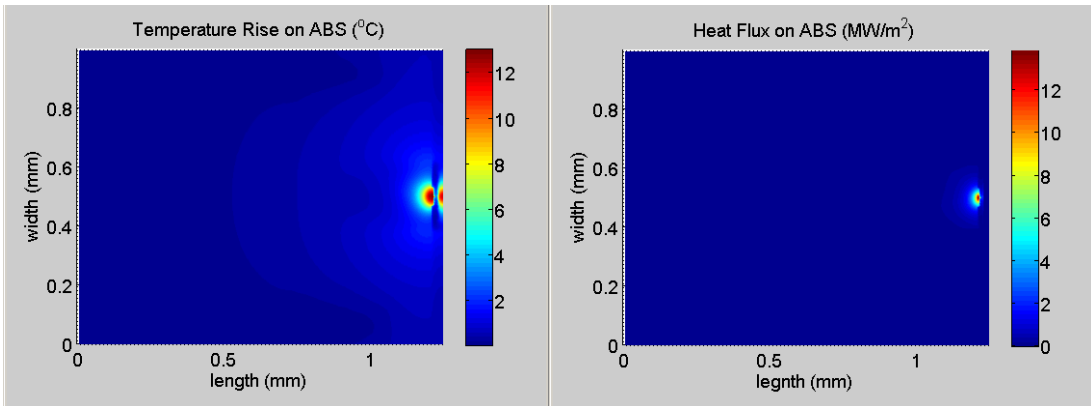
Fig.7.2. Air Bearing Surface of a commercial femto slider (unit: mm).



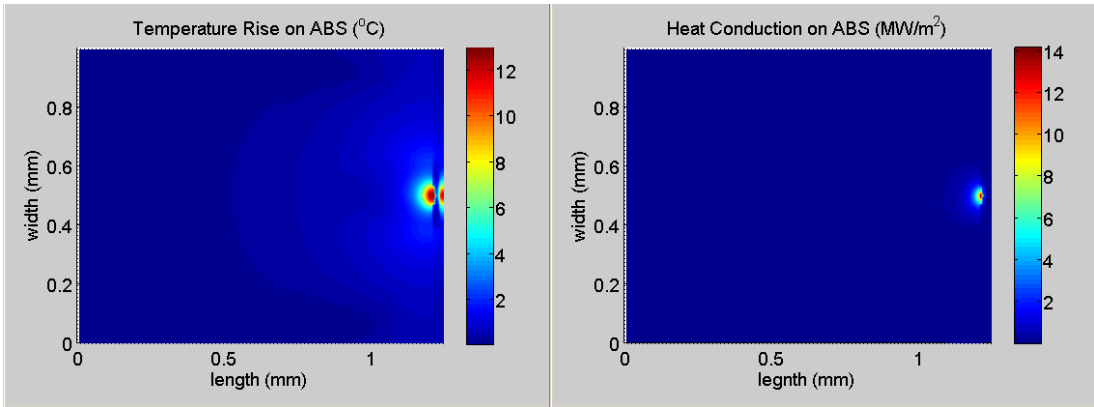
(a) 40 mW power considering the viscous heating contributed by the Couette flow



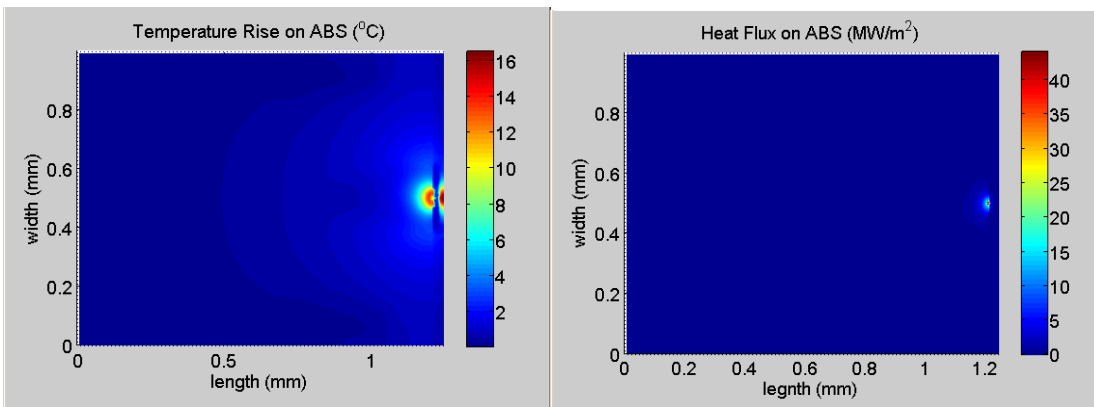
(b) 40 mW power without considering the viscous heating contributed by the Couette flow



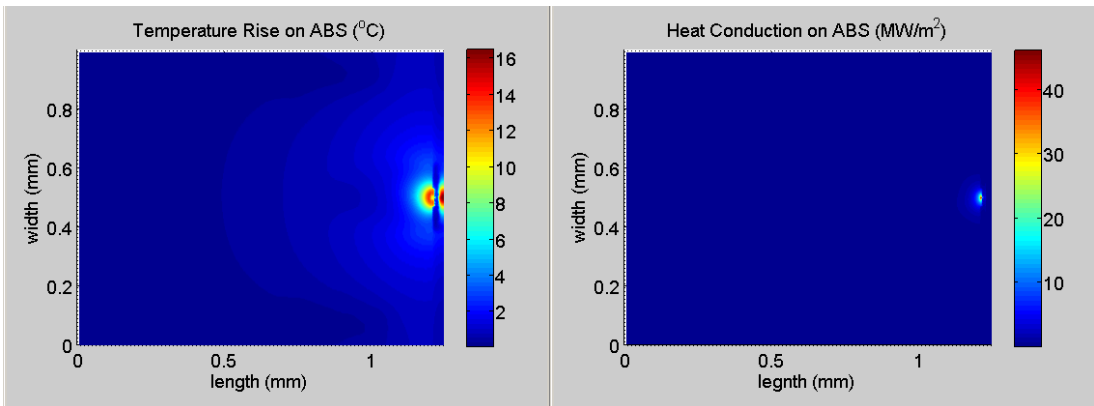
(c) 80 mW power considering the viscous heating contributed by the Couette flow



(d) 80 mW power without considering the viscous heating contributed by the Couette flow



(e) 120 mW power considering the viscous heating contributed by the Couette flow



(f) 120 mW power without considering the viscous heating contributed by the Couette flow

Fig.7.3. Temperature and heat flux on the ABS at the static state flying attitude with and without considering the viscous heating for a heating power of 40 mW, 80 mW and 120 mW.

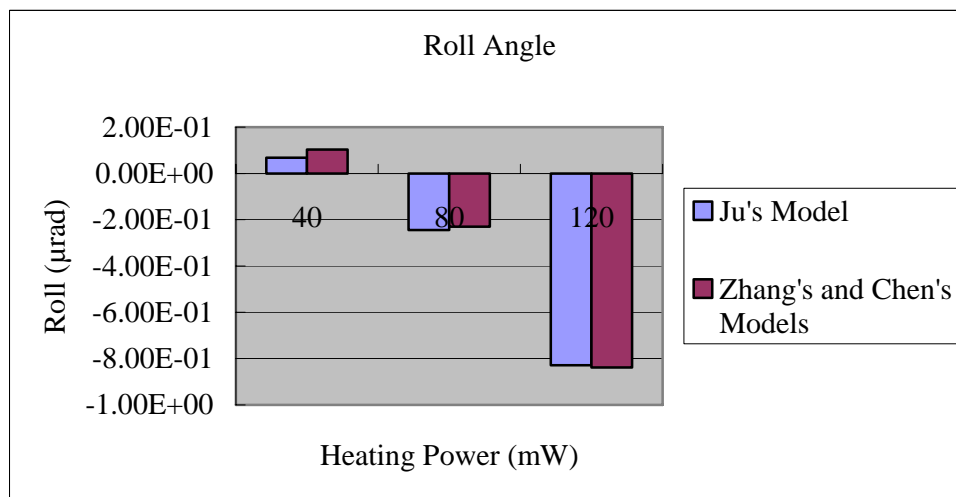
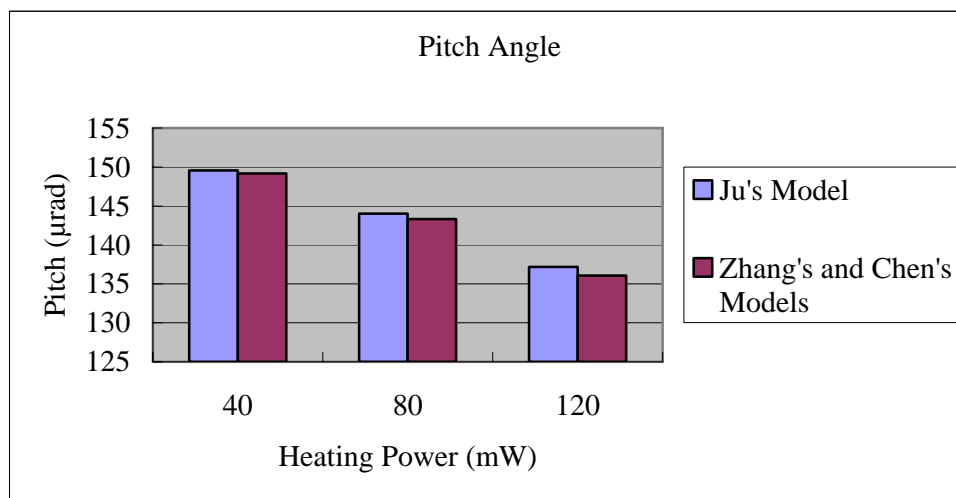
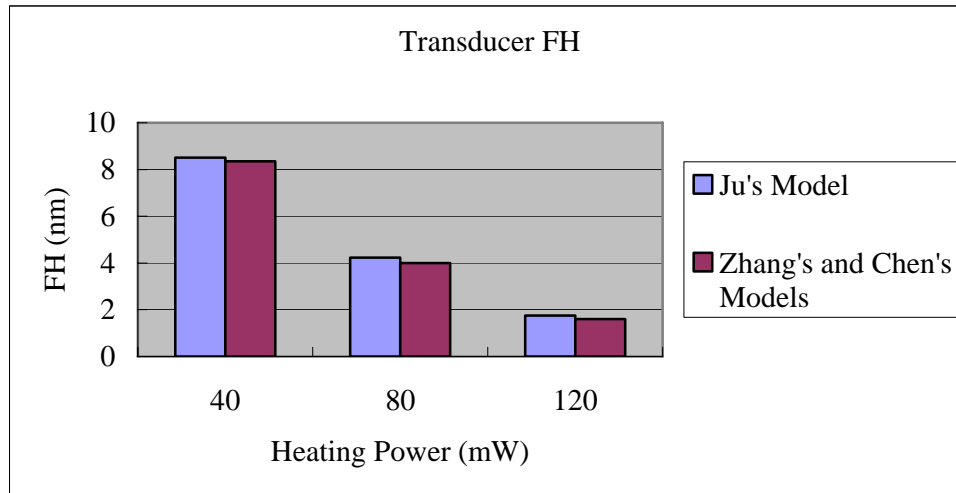
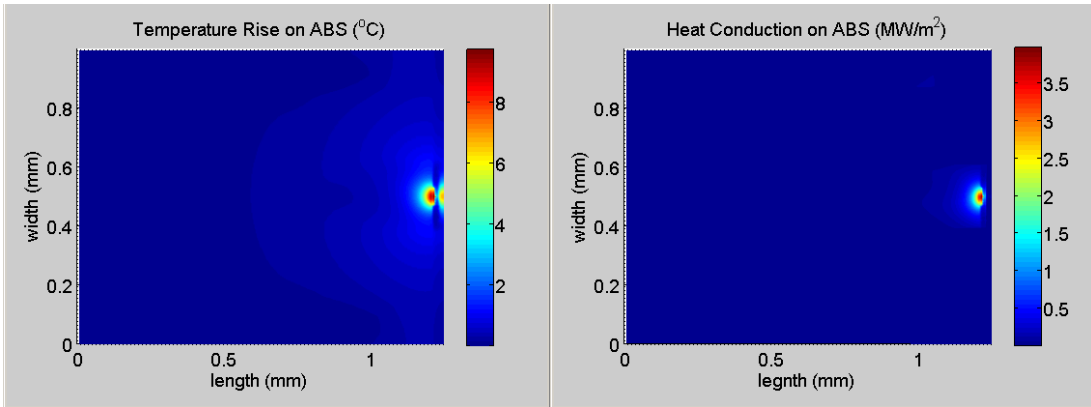
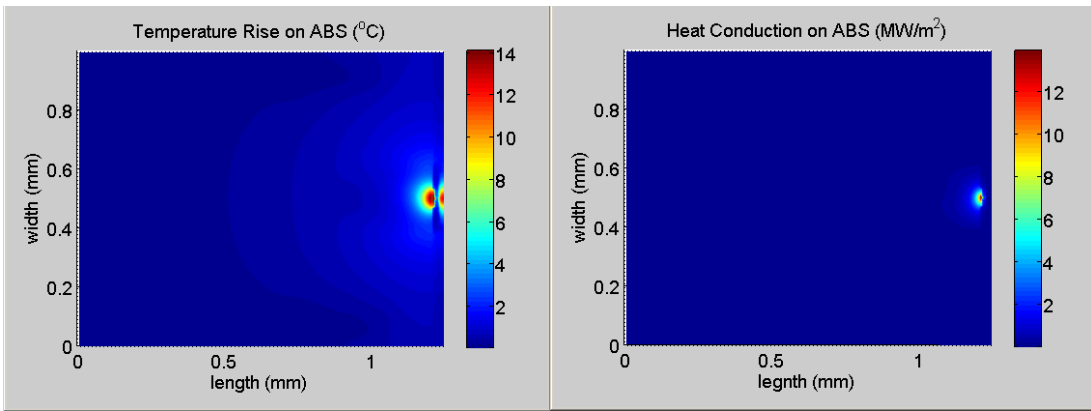


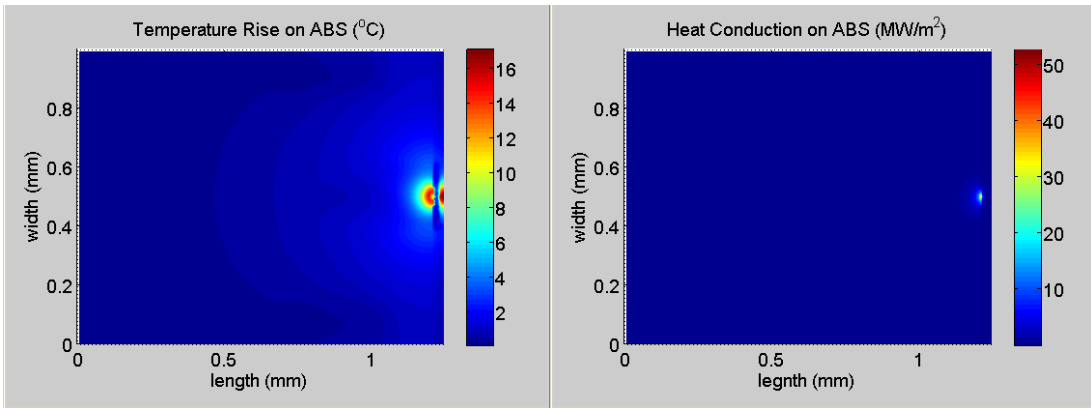
Fig.7.4. Static transducer flying height, pitch and roll angles of the slider obtained with Ju's model versus with Zhang's and Chen's models.



(b) 40 mW heating power



(c) 80mW heating power



120mW heating power

Fig.7.5. Temperature and heat conduction flux on the ABS at the static state flying attitude obtained with Zhang's and Chen's models (the viscous dissipation is neglected).

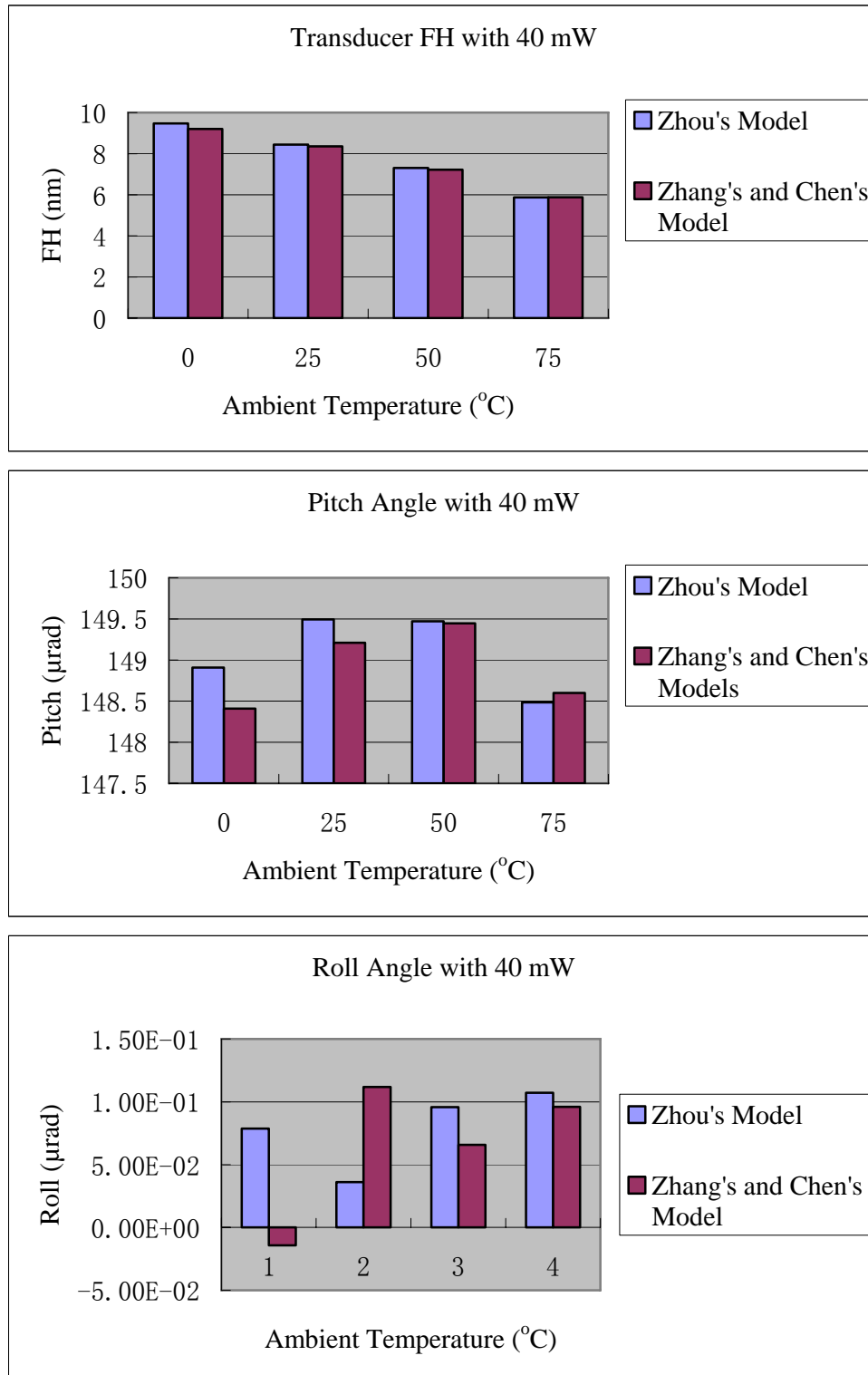


Fig.7.6. Static transducer flying height, pitch and roll angle of the slider obtained with Zhou's model versus Zhang's and Chen's models with the heating power of 40 mW.

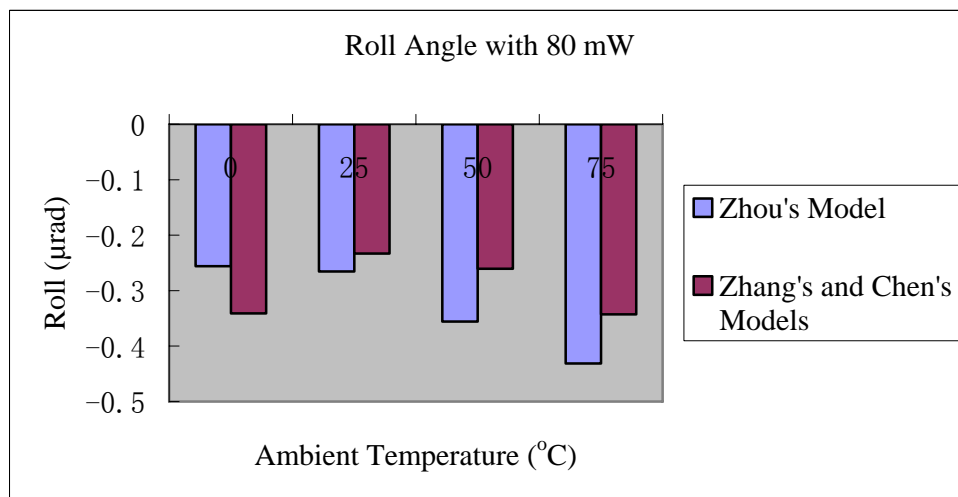
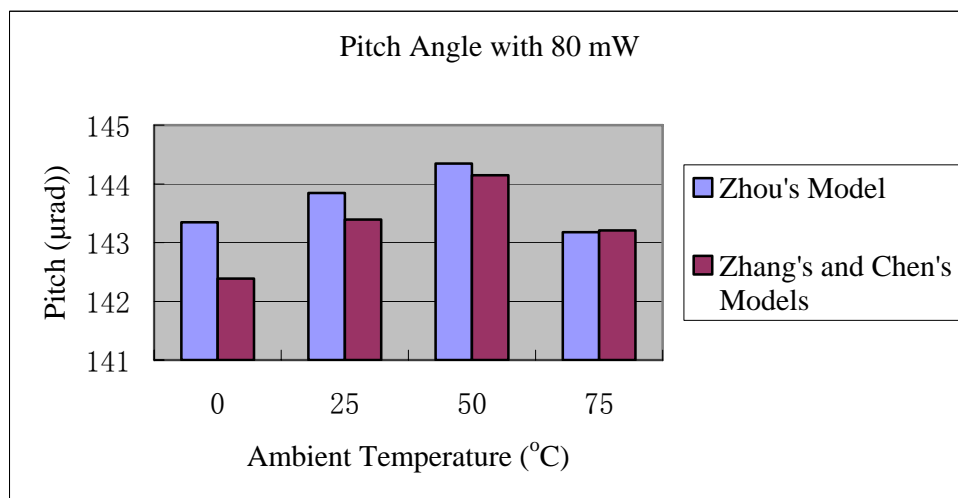
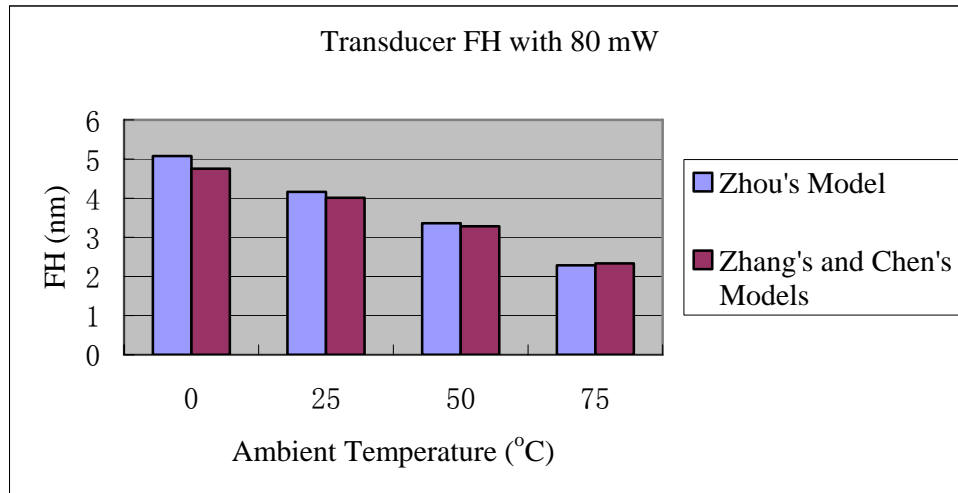
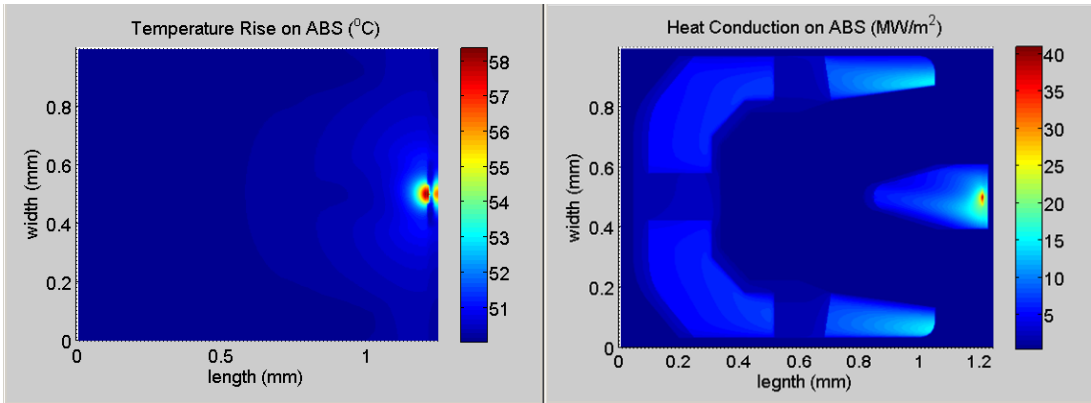
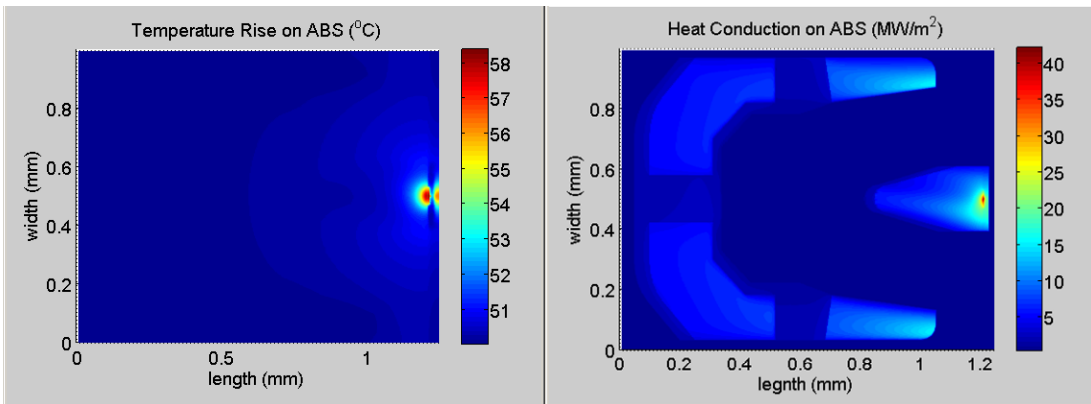


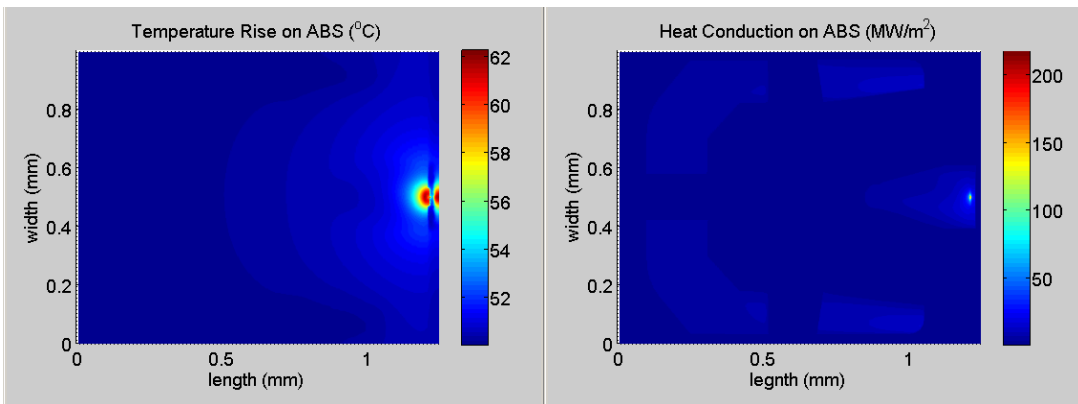
Fig.7.7. Static transducer flying height, pitch and roll angle of the slider obtained with Zhou's model versus Zhang's and Chen's models with the heating power of 80 mW.



(a) 75°C ambient temperature and 40 mW heating power with Zhou's model



(b) 75°C ambient temperature and 40 mW heating power with Zhang's and Chen's models



(c) 75°C ambient temperature and 80 mW heating power with Zhou's model

Chapter 8 Partial-Contact Head-Disk

Interface with Thermal Protrusion

A new partial-contact head disk interface (HDI) with thermal protrusion is proposed in this chapter for magnetic recording with densities of 1 Tbit/in² and above. This HDI has the advantage of maintaining light contact between the slider and the disk, so that both the bouncing vibration amplitude and the contact force are small compared with a traditional partial-contact HDI. The slider's dynamic simulations are carried out to analyze the effect of various factors within the HDI, including the friction and adhesion between the slider and the disk, the track profile morphology on the disk and the air bearing design, on the slider's dynamic performance. It is found that the bouncing vibration amplitude can be reduced to as small as the flying height modulation (FHM) of a non-contact air bearing slider without thermal protrusion.

8.1 Introduction

Reducing the read/write transducer to disk spacing and hence the slider's flying height (FH) is required to achieve higher recording densities in hard disk drives. Among those proposed interface designs with reduced FH such as wear-in and contact, a partial-contact head disk interface (HDI) is a promising way to balance the requirements of low bouncing vibrations of the slider and low wear at the head. For full contact recording with a weak air bearing or without any air bearing [1], the vibration and wear of the slider are two obstacles for practical implementation. The wear-in HDI [2 and 3] may eliminate the mechanical-tolerance-related flying height modulation (FHM),

however, damage to the read/write transducer in the wear-in process can not be eliminated and the transducer is also worn away. On the other hand, studies [4-6] on partial-contact recording indicate that a small contact area is effective in reducing friction and slider bouncing.

This chapter presents a new partial-contact HDI design to achieve a low transducer FH, low slider bouncing vibration, and a low contact force between the slider and disk. This HDI makes use of the thermal protrusion feature of a thermal FH control (i.e. dynamic FH) slider, so that only the protrusion tip, close to the protruded transducer, contacts the disk surface. This chapter is focused on the study of the factors in the HDI affecting the slider's bouncing and slider-disk contact. An air bearing surface (ABS) design concept is proposed for the partial-contact HDI with thermal protrusion.

8.2 Partial-contact HDI with thermal protrusion

The thermal flying height control (TFC) or dynamic flying height (DFH) technique is widely used in current hard drives to lower the slider's FH, which is presented in the patent by Meyer et al. [7]. This advantageous technique makes use of a resistance heating element near the read/write transducer. When a current is applied through the heating element, the Joule-heat-caused thermal expansion forms a local thermal protrusion close to the read/write transducer, which is near the trailing edge center. This local thermal protrusion reduces the flying height at the protruded transducer. In this way the transducer FH becomes adjustable. This technique not only provides control that can compensate for the static FH loss and reduce the likelihood of head-disk contacts for an air bearing slider, but also shows a potential of achieving a partial-contact HDI.

With a heating power above a critical value in a properly designed slider, the thermal

protrusion at the transducer comes into contact with the disk. The small contact area at the thermal protrusion tip, which has a radius of curvature around 20-30 mm and controlled by the input heating power, helps maintain light contact between the slider and the disk, while the rest of the ABS remains undeformed and flies at a safe distance from the disk. Based on studies of the partial-contact recording [5 and 6], a small interference area between the slider and the disk results in small friction and contact force and small bouncing vibration. So it is expected that the performance of a partial-contact slider with thermal protrusion is better than a partial-contact slider with a micro trailing pad, such as that analyzed in [6].

8.3 Dynamic Simulation of a partial-contact slider with thermal protrusion

The static simulation of an air bearing slider with thermal protrusion was first carried out by Juang, Chen and Bogy [8] with the consideration of the air bearing cooling effect. In the work of Chen and Bogy [9], HDI heat transfer models were implemented in the static simulation and the obtained static flying attitudes were compared. However, for the dynamic simulation of a partial-contact slider with thermal protrusion on the disk surface, the thermal protrusion changes dynamically due to the dynamic air bearing cooling and the dynamic slider-disk interaction, which are associated with the slider's FHM or bouncing vibration. This dynamic thermal protrusion incurs difficulties in a full dynamic simulation of a partial-contact slider with thermal protrusion.

In this chapter two approximations are adopted in the dynamic simulation. First, the thermal protrusion is taken as a constant geometry on the ABS, which only depends on the heating power for a given slider. This means that in the simulation the thermal

protrusion does not change as the flying height modulates or the slider bounces on the disk surface. In fact, a transient thermal response study shows that the response of thermal protrusion has a bandwidth of about 1 kHz [8], which is much smaller than the air bearing frequencies and bouncing frequencies. Hence, the first approximation is reasonable. Second, the friction heating and heat conduction caused by the slider-disk contact are negligible. In the slider-disk contact area, the friction heating counteracts the heat conduction from the slider to the disk. It is assumed in this chapter that the friction heating and contact-caused heat conduction cancel each other and the total effect is negligible, due to the small contact area at the tip of the thermal protrusion.

Based on these two approximations, two steps are taken for the dynamic simulation of a partial-contact slider with thermal protrusion. First, the static flying attitude with thermal protrusion on a flat disk is calculated and the thermal protrusion profile is obtained for a given input heating power. The iteration approach in [8] with a static air bearing solver and a finite element analysis of thermal deformation is used. Second, the obtained thermal protrusion profile is added to the ABS profile and the dynamic simulation of the partial-contact slider is carried out. A nonlinear dynamics model developed for a partial-contact HDI in [6] is used here for the slider dynamics. The air bearing with contact and slider-disk adhesion, contact and friction are all considered in this model. As listed in [6], numerical methods are used to calculate the contact and adhesion force and solve the time-dependent air bearing equations and 3-degree-of-freedom slider dynamic equations.

In this chapter an INSIC pico slider with thermal protrusion, which was used in [8], is employed as Slider 1 in dynamic simulation. The slider's ABS is shown in Figure 8.1. We are interested here in studying the effects of various parameters on the performance of

partial-contact sliders with thermal protrusion, and the pico form factor is suitable for that study, but we are not proposing a particular design for future use in HDDs, since the industry has already moved to the smaller femto form factor sliders. It has zero crown, camber and twist. The suspension preload is 1.5 gf and there is no load offset. The disk RPM is 7200. Another two sliders with the ABS's modified based on Slider 1 are used in the analysis of the effect of the ABS design on the slider's bouncing. A measured track profile, which is shown in Figure 8.2, is used in the dynamic simulation. Another rough disk track profile and burnished smooth track profiles are also used to analyze the effect of micro-waviness and roughness on the slider's bouncing. In the simulation the sliders are thermally actuated from 5 nm and a 1-ms dynamic simulation is carried out for the slider's response.

8.4 Simulation results and discussion of partial-contact sliders with thermal protrusion

8.4.1 FHM and bouncing vibration

The slider's transducer FH reduces as the heating power increases. Beyond a certain heating power, the slider may touch the disk surface. Figure 8.3 shows the time histories of the slider dynamics with heating powers from 0 mW, 15 mW, 20 mW to 25 mW. The slider flies above the disk surface when there is no heating. The 3-sigma of the variation of the transducer FH is 0.50 nm. When the heating power is increased to 15 mW, the slider touches the disk only at the beginning and the 3-sigma of the transducer FH is 0.57 nm. When the heating power is increased beyond 15 mW, the slider touches the disk surface and the minimum spacing becomes negative. The 3-sigma of the variation of the transducer FH increases to 1.06 nm at 20 mW and 1.04 nm at 25 mW. The bouncing

vibration amplitude of the slider in partial contact is much larger than the FHM of the slider at flying. The mean pitch angle and roll angle decrease as the heating power increase, which agrees with the static simulation results in [9]. The variations of the pitch angle increase as the slider touches the disk. The contact force between the slider and the disk remains below 0.05 gf when the slider touches down, which is much smaller than the 1.5-gf preload of the suspension force acting on the slider.

Figure 8.3 also shows the corresponding power spectrum of the FH with these values of heating powers. It is seen that the slider's peak frequencies increase as the slider flies lower with a heating power of 15 mW. This can be explained with the decreased FH and increased air bearing stiffness. When the slider touches the disk surfaces with heating powers above 20 mW, a high frequency peak around 700 kHz occurs. Similar to the high frequency peak of a partial-contact micro-trailing pad slider, this high frequency peak is related to the slider-disk contact.

8.4.2 A partial-contact slider with thermal protrusion and a partial-contact micro-trailing-pad slider

Figure 8.4 shows the time history of the dynamics of Slider 1 and the micro-trailing-pad slider in [6] on the smooth track in Figure 8.2. It is obvious that the vibration amplitudes of the transducer FH, pitch and roll of the micro-trailing-pad slider are much larger than those of Slider 1. The contact force of the micro-trailing-pad slider is also much larger than that of Slider 1. This indicates that the contact between the disk and the protrusion tip, as opposed to that of the micro trailing pad, causes a smaller interaction between the slider and the disk. The slider's bouncing vibration and the contact force can be greatly reduced simultaneously through the partial-contact with thermal protrusion.

8.4.3 Friction between the slider and the disk

As discussed in [6], the friction force between a partial-contact slider and a disk is not the direct cause of the slider's bouncing vibration, and it has only a slight effect on the bouncing amplitude. The reason is that the torque acting on the slider due to the friction force is much less than that from the contact and adhesion force, with respect to the slider's mass center. For the contact between the slider's thermal protrusion and the disk, it is expected that the effect of friction force is negligible, since the contact area and contact force is even smaller. This is verified by the dynamic simulation of Slider 1 with 25 mW heating power, as shown in Figure 8.5. Here the friction coefficient between the slider and the disk varies from 0.3, 1.0 to 2.0 and the disk track profile is that shown in Figure 8.2. The 3-sigma of transducer spacing remains approximately 1.0 nm. Also the vibrations of pitch and roll angles are almost the same as without friction considered. The contact force between the slider and the disk is also not affected by the friction coefficient. So the friction between the slider and the disk has almost no effect on the slider's bouncing vibration.

8.4.4 Adhesion between the slider and the disk

The adhesion force between the slider and the disk is proportional to the change of surface energy before and after the slider-disk contact in the modified intermolecular force model [10]. To study the effect of adhesion on the dynamics of Slider 1, the change of surface energy before and after contact is set to range from 0.08 J/m², 0.008 J/m² to 0.001 J/m². The disk track profile shown in Figure 8.2 is used and the heating power is 25 mW. The corresponding dynamic simulation results for Slider 1 are shown in Figure 8.6. As the change of surface energy varies, the vibration amplitudes of pitch and roll angles and the bouncing vibration amplitude do not change much. The 3-sigma of the transducer

spacing ranges between 1.0-1.2 nm approximately. But the mean of transducer spacing increases from 1.66 nm, 1.98 nm to 2.01 nm, as the change of surface energy decreases. Correspondingly, the peak of the contact force decreases from 0.15 gf, 0.05 gf to 0.02 gf. This indicates that the slider-disk intermolecular adhesion has a smaller effect on the bouncing vibration of Slider 1 with thermal protrusion than of a partial-contact slider with micro-trailing pad in [6]. The reason is related to the small contact area between the slider and the disk. As most parts of the ABS are farther away from the disk, the adhesion between them and the disk does not vary much. Reduced slider-disk adhesion only results in a higher transducer flying height and a smaller contact force, while the slider's bouncing vibration is almost unchanged.

8.4.5 Disk surface

a) Rough disk surface and smooth disk surface

The smooth track profile shown in Figure 8.2 has a root mean square (RMS) value of 0.2 nm. A rough track profile with RMS 0.6 nm is shown in Figure 8.7. These two track profiles were obtained from the LDV-measured disk morphologies [14]. Frequency components below 10 kHz were filtered out and the profile features less than 5 μm could not be captured. These two tracks are incorporated into the dynamic simulation of Slider 1. To exclude the effect of slider-disk adhesion, the change of surface energy before and after contact is set as zero. The time histories of the slider dynamics are shown in Figure 8.8. The 3-sigma of the transducer spacing is around 3.5 nm on the rough track, while it is only around 1.0 nm on the smooth track. The peak of the contact force is 0.24 gf on the rough track, while it is only 0.02 gf on the smooth track. The vibration amplitudes of the pitch and roll angles are smaller on the smooth track than on the rough one. It is shown that a partial-contact slider with thermal protrusion has a smaller contact force as well as

bouncing vibration amplitude on a smoother disk surface. This agrees with the conclusion in [6] that the slider's bouncing is a forced vibration due to the micro-waviness and roughness moving through the HDI as the disk rotates. A smoother track has a smaller excitation and reduces the slider's bouncing vibration and contact force.

b) Burnished Disk Surfaces

As a further analysis of the effect of the track profile on the slider's bouncing, we numerically burnish the track profile shown in Figure 8.2. Here we employ two kinds of burnishing. One is a time-domain burnishing, which approximates the burnishing process of a glide-head slider on the track; the other is a frequency-domain burnishing, which is to show the effect of high frequency components of the track on the disk surface. For the time-domain burnishing, a smoothing method called running line smoothing [11] is used to burnish local peaks. This method carries out a linear fitting between the measurement point position and the track profile height in the neighborhood of each measurement point. The linear fitting is taken as a base line at each point. The track is burnished where the track height is above the local base line. Here the neighborhood length is chosen to be 25 μm , which is approximately the length of the trailing pad of a glide-head slider. The remaining local peak height after burnishing is set as 0.1 nm, since local peaks may not be totally flattened after burnishing. The burnished track profile and power spectrum are shown in Figure 8.9(a). The frequency-domain burnishing is used to remove the components with frequencies higher than a given value from the track profile. Here that frequency is set to be 500 KHz. A low pass filter is used for this burnishing process. Figure 8.9(b) shows the burnished track profile and its power spectrum. In practice, the frequency-domain burnishing is hard to implement. The RMS values of the burnished tracks are still approximately 0.2 nm.

The time histories of Slider 1 with heating power 20 mW on the original track in Figure 8.2 and the burnished tracks in Figures 8.9(a) and (b) are plotted in Figure 8.10. The vibrations of the pitch and roll angles of Slider 1 on these three tracks are almost the same. However, the 3-sigma of the transducer FH is 1.1 nm on the original track, while it is 0.9 nm on the time-domain burnished track and 0.5 nm on the frequency-domain burnished track. However, the time history of the contact force remains almost unchanged. The removal of frequency components above 500 KHz reduces the bouncing vibration more than the removal of local peaks. As the external excitations above 500 KHz are removed, the bouncing vibration amplitude of Slider 1 can be lowered close to the FHM of Slider 1 without thermal protrusion. This is reasonable since the dominant frequencies of the slider's bouncing are around 700 kHz. This is also indicated by the power spectra of FH on these disk tracks. It is seen that the patterns of the power spectra are similar, however, the frequency peak around 700 kHz is much lower on the frequency-domain burnished track than on the unburnished or time-domain burnished track.

8.4.6 ABS designs for a Partial-Contact HDI with Thermal Protrusion

It has been shown by Thornton and Bogy [12] that the ABS design has an important effect on the slider's FHM. The ABS design with a high air pressure peak at the transducer helps reduce the slider's FHM [12]. Here we focus on the effect of the ABS design on the bouncing vibration of a partial-contact slider, which has larger amplitude than the FHM of a flying slider. Two different ABS designs are obtained through modifying the ABS of Slider 1. The sliders with these two ABS's are denoted as Slider 2 and Slider 3, respectively, and they are shown in Figure 8.10. Slider 2 has no side trailing pads and Slider 3 has a small discrete trailing pad. With adjusted preload and load offset,

the static flying attitudes of Slider 1, 2 and 3 can be very close. They are listed in Table 8.1.

The static simulations with and without heating power are carried out for these three sliders. The air bearing pressure profiles at the static state without heating power for Sliders 1, 2 and 3 are shown in Figure 8.11. It is seen from Figure 8.12 that Slider 2 has the highest air bearing peak pressure at the transducer and Slider 3 has the lowest peak pressure. The touch-down heating power is approximately 20 mW for Slider 1, 40 mW for Slider 2 and 10 mW for Slider 3. It is seen that Slider 3, which has the lowest peak air pressure at the transducer, has the smallest touch-down heating power, while Slider 2, which has the highest air bearing peak pressure at the transducer without side air bearing peaks, has the largest touch-down heating power. This agrees with the ABS design guideline for high actuation efficiency developed by Juang and Bogy [13]. The corresponding air bearing pressure profiles on touch-down are shown in Figure 8.13. Slider 2 still has the highest air bearing peak pressure. With the touch-down heating power, Slider 1 as well as Slider 2 has a dramatic increase in the air bearing peak at the transducer. However, the air bearing peak pressure at the discrete trailing pad of Slider 3 does not increase much after the heating power is on. This explains the small touch-down heating power of Slider 3.

With each touch-down heating power, the dynamic simulations of Slider 1, Slider 2 and Slider 3 are carried out, respectively. The time histories of the slider dynamics are shown in Figure 8.14. It is seen that the vibration amplitudes of the sliders are almost the same in the pitch and roll direction. However, the vertical vibration amplitudes of these sliders are different. The 3-sigma of the transducer FH is 1.0 nm for Slider 1, 0.7 nm for Slider 2 and 3.5 nm for Slider 3. The peak of the contact force is 0.5 gf for Slider 3, while it is

less than 0.05 gf for Slider 1 and Slider 2. The plot of the minimum spacing shows that Slider 2 contacts the disk surface only from time to time. This indicates that the high air bearing pressure at the trailing edge center helps keep the slider in a light contact condition with the disk so that the contact force and bouncing amplitude also remain small.

8.5 Conclusions

A new partial-contact head disk interface slider with thermal protrusion is analyzed to achieve a low transducer flying height for a high magnetic recording density. Light contact between the thermal protrusion tip, which is close to the protruded transducer, and the disk can be maintained with a certain heating power. A dynamic simulation scheme for such partial-contact sliders with thermal protrusion is presented and discussed.

The results of the dynamic simulations show that the bouncing vibration amplitude and the contact force of a partial-contact slider with thermal protrusion are much smaller than the partial-contact micro-trailing pad slider on the same smooth disk track.

The dynamic simulation results also show the effect of various factors within the HDI, including the friction and adhesion between the slider and the disk, the track profile morphology on the disk and the air bearing design, on the slider's dynamic performance with thermal protrusion. It is found that the friction between the slider and the disk has almost no effect on the slider's vibration and mean flying attitude. The slider-disk adhesion changes the mean flying height, but has little effect on the slider's vibration. The slider's bouncing vibration amplitude can be reduced to a value similar to the FHM with no contact, when the disk track is burnished or the air bearing pressure peak is

enforced at the trailing edge center. For the INSIC pico slider [8], the mean transducer flying height can be reduced below 3 nm with heating powers above 20 mW. The 3-sigma of the bouncing amplitude can be reduced from 1.1 nm to 0.5 nm, when the frequencies components above 500 Khz are removed from the track. A modified air bearing surface with a higher air bearing pressure at the transducer weakens the contact force between the protrusion tip and the disk, while the bouncing vibration amplitude is only 0.5 nm, which is comparable to the flying height modulation of the INSIC slider without thermal protrusion, and the peak of the contact force is less than 0.05 gf, which is much smaller than the suspension preload.

References

- [1] J. Itoh, Y. Sasaki, K. Higashi, H. Takami and T. Shikanai, "An Experimental Investigation for Continuous Contact Recording Technology," *IEEE Trans. Magn.*, vol. 37, no. 4, pp. 1806-1808, 2001.
- [2] B. Strom, S. Deits, C. Gerber, D. Krajnovich, D. Ohlsen and R. Turner, "Burnishing Heads In-Drive for Higher Density Recording," *IEEE Trans. Magn.*, vol. 40, no. 1, pp. 345-347, 2004.
- [3] G. P. Singh, B. E. Knigge, R. Payne, R. H. Wang, C. M. Mate, P. C. Arnett, C. Davis, V. Nayak, X. Wu, K. Schouterden and P. Baumgart, "A Novel Wear-In-Pad Approach to Minimizing Spacing at the Head/Disk Interface," *IEEE Trans. Magn.*, vol. 40, no. 4, pp. 3148-3153, 2004.
- [4] C. M. Mate, P. C. Arnett, P. Baumgart, Q. Dai, U. M. Guruz, B. E. Knigge, R. N. Payne, O. J. Ruiz, G. J. Wang and B. K. Yen, "Dynamics of Contacting Head-Disk Interfaces," *IEEE Trans. Magn.*, vol. 40, no. 4, pp. 3156-3158, 2004.

- [5] J. Xu, H. Kohira, H. Tanaka and S. Saegusa, "Partial-Contact Head-Disk Interface Approach for High-Density Recording," *IEEE Trans. Magn.*, vol. 41, no. 10, pp. 3031–3033, 2005.
- [6] D. Chen and D. B. Bogy, "Dynamics of Partial Contact Head Disk Interface," *IEEE Trans. Magn.*, vol. 43, no. 6, pp. 2220-2222, 2007
- [7] D. W. Meyer, P. E. Kupinski and J. C. Liu, "Slider with Temperature Responsive Transducer Positioning," U. S. Patent 5991113, Nov. 23, 1999.
- [8] J. Y. Juang, D. Chen and D. B. Bogy, "Alternate Air Bearing Slider Designs for Areal Density of 1 Tbit/in²," *IEEE Trans. Magn.*, vol. 42, No. 2, pp. 241-247, 2006.
- [9] D. Chen and D. B. Bogy, "Simulation of Static Flying Attitude with Different Heat Transfer Models for a Flying Height Control Slider with Thermal Protrusion," Technical Report No. 2008-03, Computer Mechanics Laboratory, Department of Mechanical Engineering, University of California, Berkeley, 2008.
- [10] D. Chen and D. B. Bogy, "Intermolecular Force and Surface Roughness Models for Air Bearing Simulations for Sub-5nm Flying Height Sliders," Technical Report No. 2006-016, Computer Mechanics Laboratory, Department of Mechanical Engineering, University of California, Berkeley, 2006.
- [11] L. Fahrmeir and G. Tutz, *Multivariate Statistical Modelling Based on General Linear Models*, second edition, Springer, 2001.
- [12] B. H. Thornton, A. Nayak and D. B. Bogy, "Flying Height Modulation due to Disk Waviness of Sub-5 nm Flying Height Air Bearing Sliders," *ASME Jour. of Tribol.*, vol. 124, No. 4, pp. 762-770, 2002.
- [13] J. Y. Juang and D. B. Bogy, "Air-bearing Effects on Actuated Thermal Pole-Dip Protrusion for Hard Disk Drives," *ASME Jour. of Tribol.*, vol. 129, No. 3, pp. 570-578,

2007.

[14] B. H. Thornton, D. B. Bogy and C. S. Bhatia, "The Effects of Disk Morphology on Flying-Height Modulation: Experiment and Simulation," *IEEE Trans. Magn.*, vol. 38, No.1, pp. 107–111, 2002.

Table 8.1 Suspension load and flying attitudes of Slider 1, 2 and 3 with heating power off

	Suspension load	Flying attitude
Slider 1	Preload: 1.5 gf X-offset: 0 nm Y-offset: 0 nm	Transducer FH: 4.60 nm Pitch: 187.31 μ rad Roll: -0.57 μ rad
Slider 2	Preload: 1.8 gf X-offset: 200 nm Y-offset: 0 nm	Transducer FH: 4.46 nm Pitch: 169.40 μ rad Roll: 1.59 μ rad
Slider 3	Preload: 1.1 gf X-offset: 50 nm Y-offset: 0 nm	Transducer FH: 4.87 nm Pitch: 179.60 μ rad Roll: -1.70 μ rad

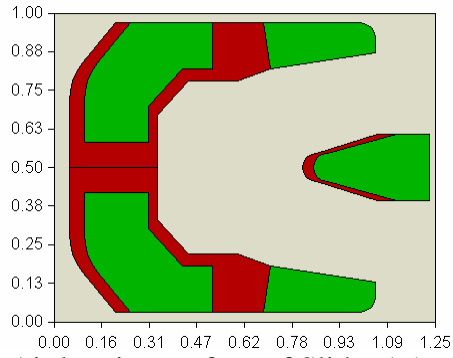


Fig.8.1. Air bearing surface of Slider 1 (unit: mm).

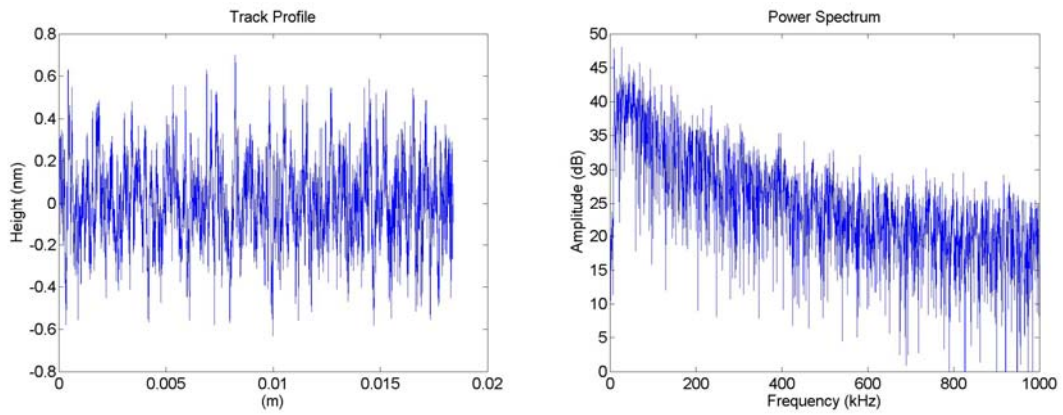


Fig.8.2. A smooth track profile and its power spectrum corresponding to a disk linear velocity of 17.34 m/s.

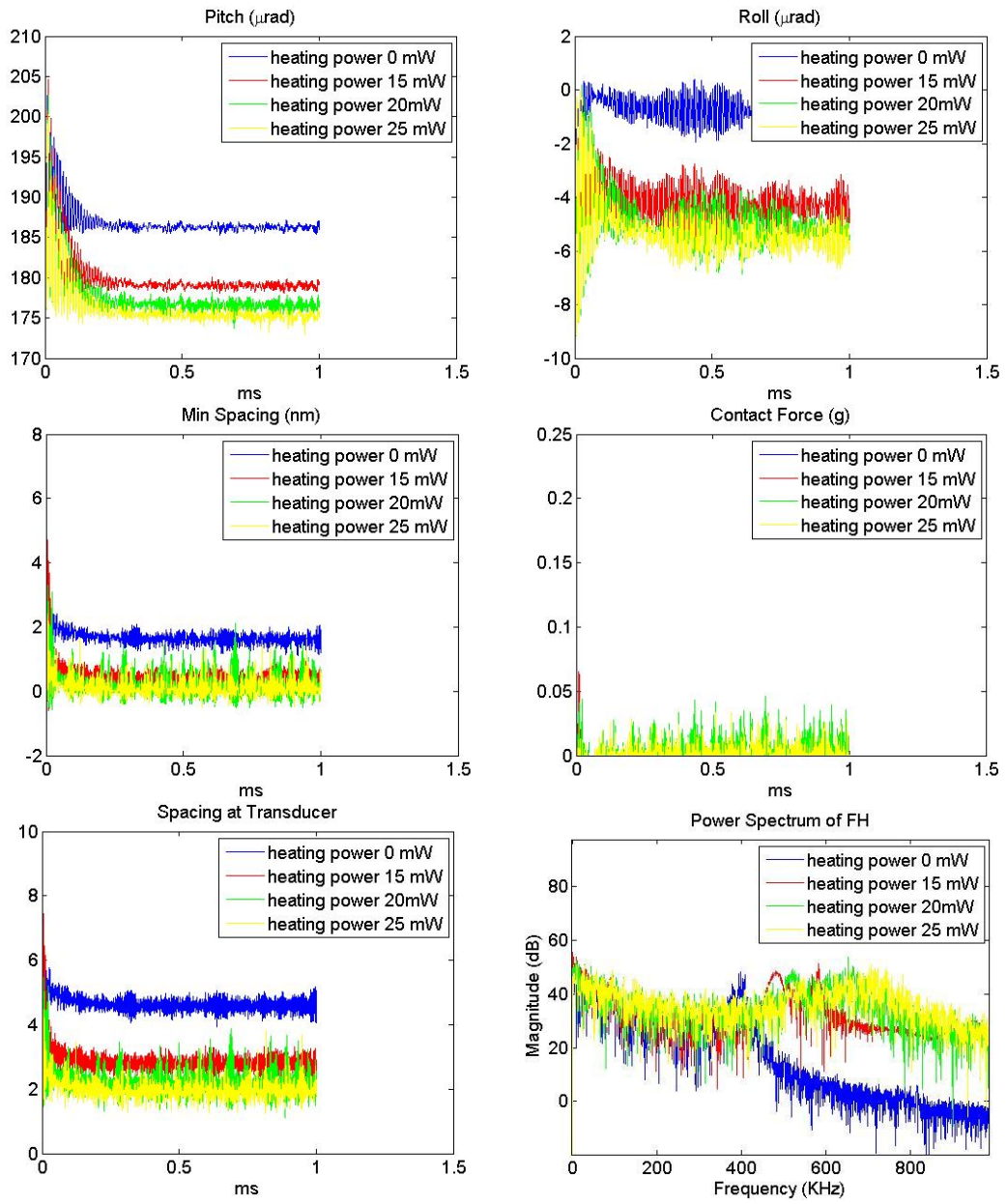


Fig.8.3. Time history of Slider 1 with heating powers of 0 mW, 15 mW, 20 mW to 25mW and the corresponding FH power spectrum.

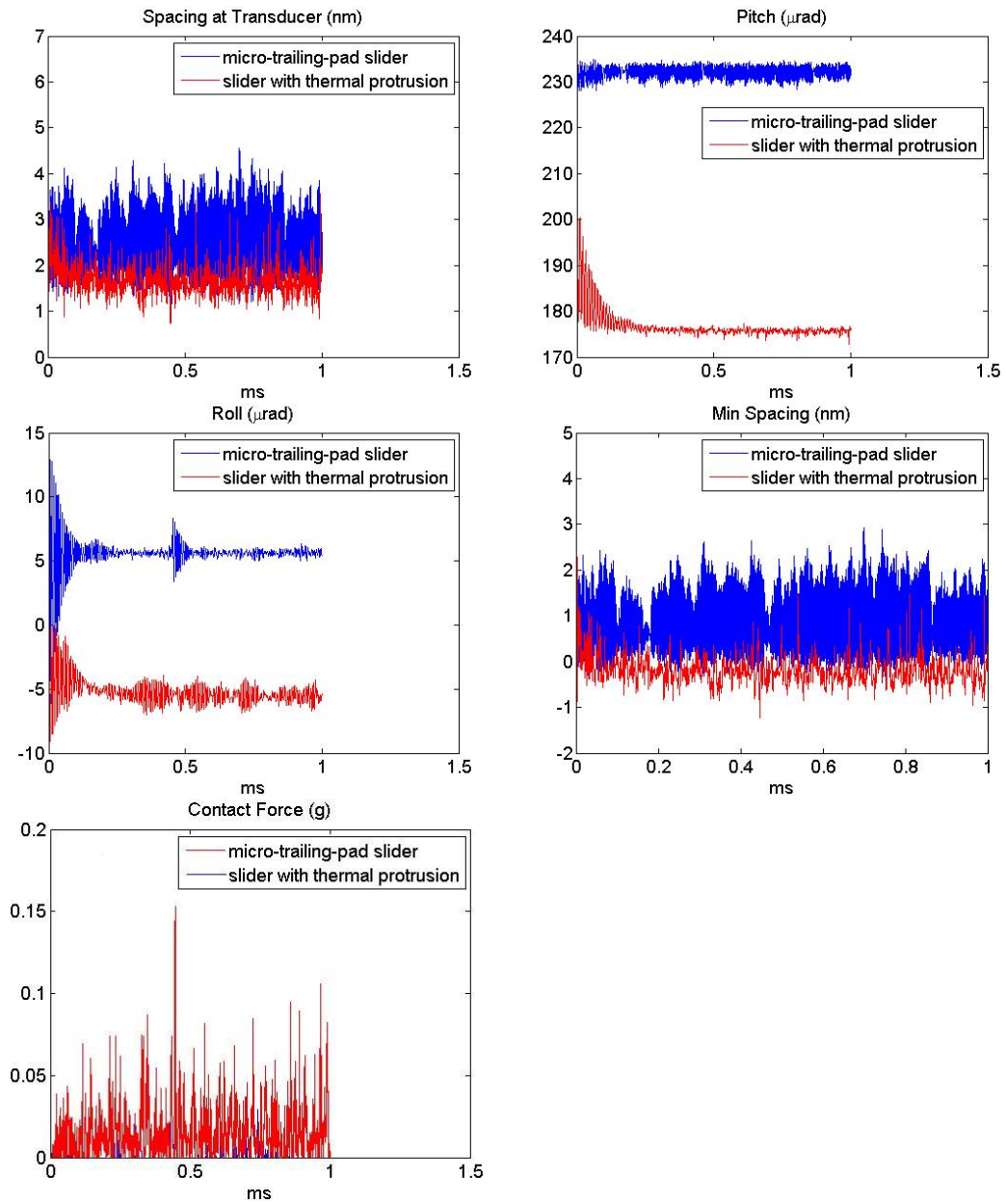


Fig.8.4. Time histories of a partial-contact slider with thermal protrusion and a partial-contact micro-trailing-pad slider on the smooth track.

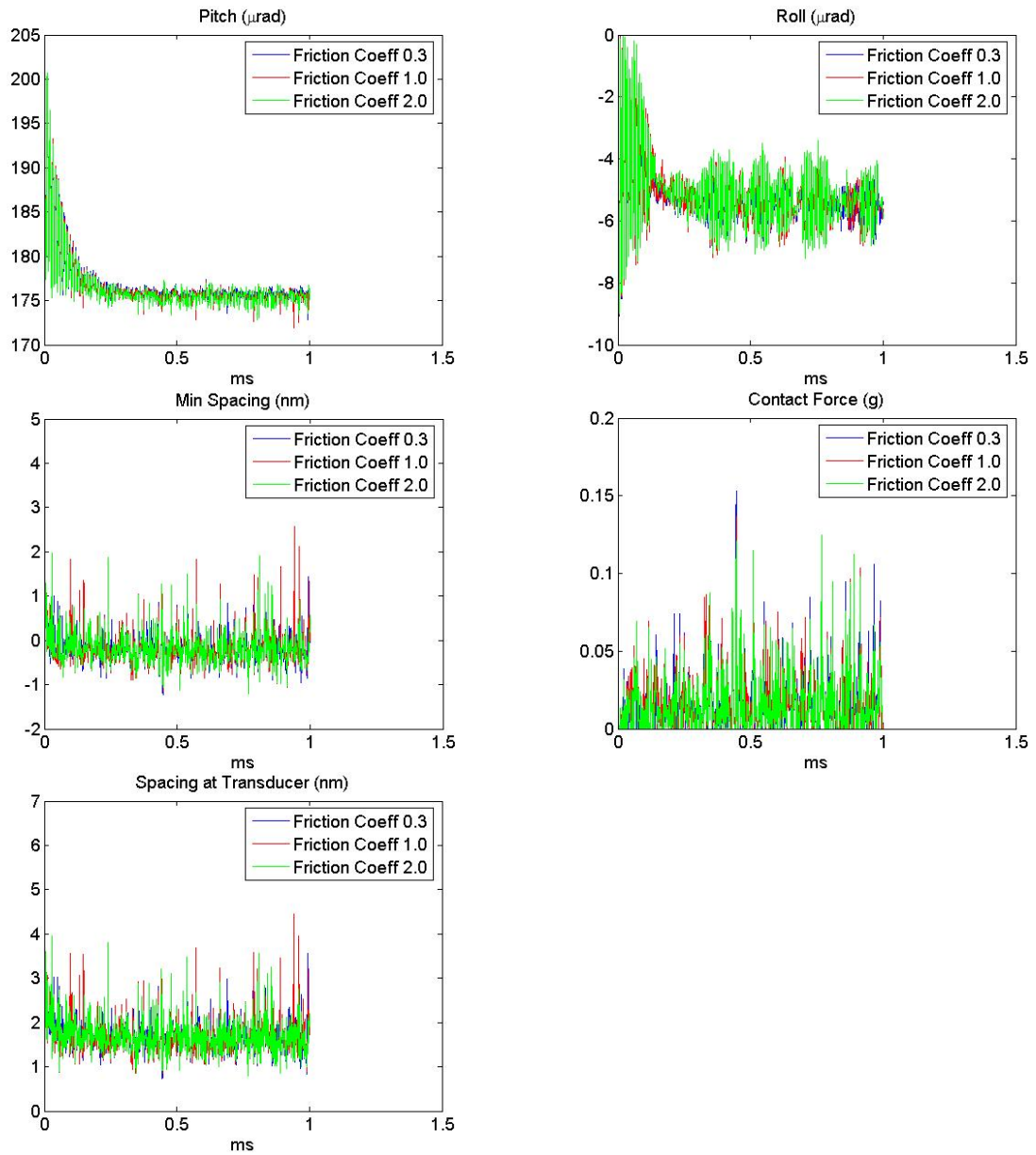


Fig.8.5. Time histories of Slider 1 with 25 mW heating power on the smooth disk track with the friction coefficient values of 0.3, 1.0 and 2.0.

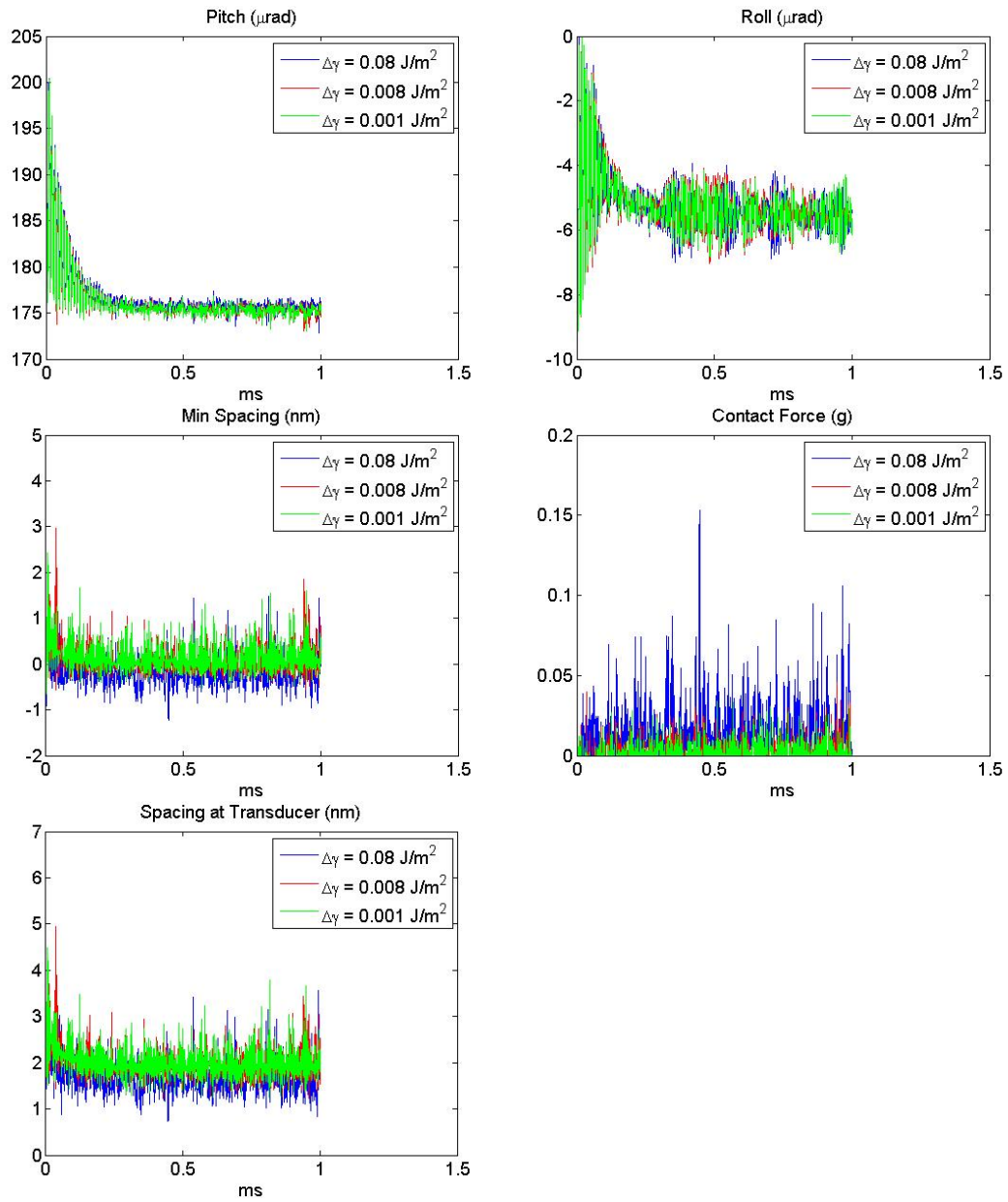


Fig.8.6. Time histories of Slider 1 on the smooth track with the change of surface energy before and after slider-disk contact ($\Delta\gamma$) for values of 0.08 J/m², 0.008 J/m² and 0.001 J/m².

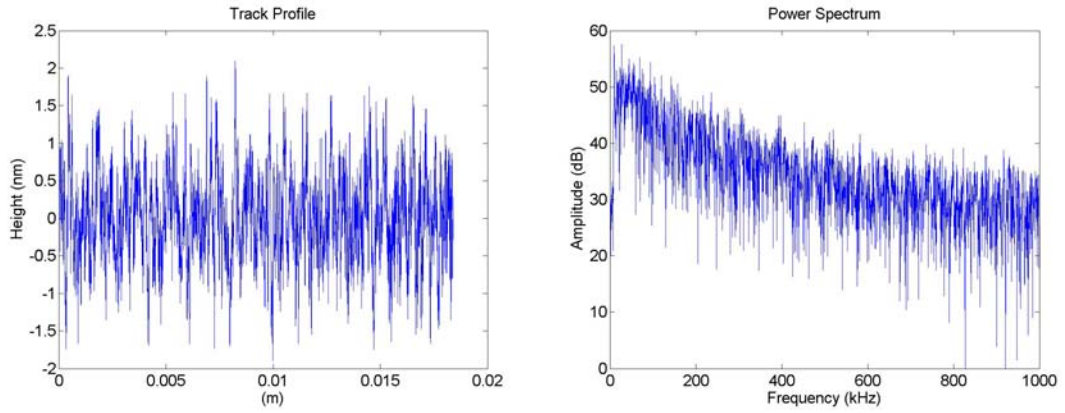
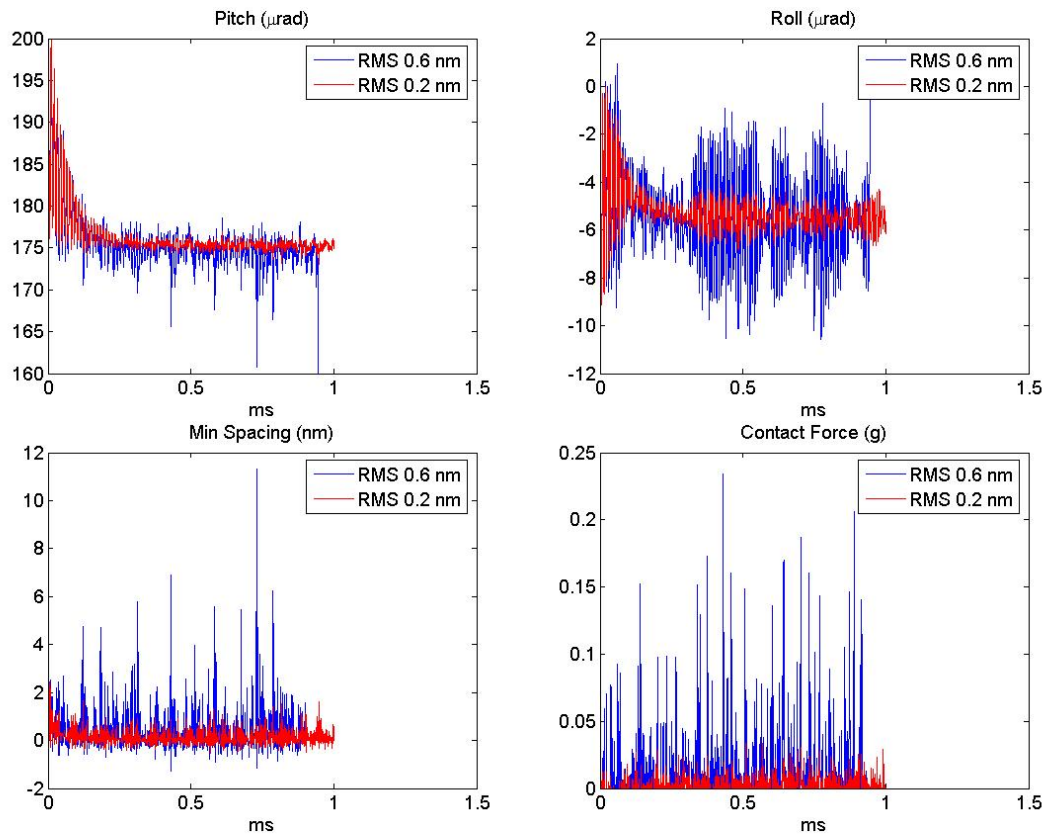


Fig.8.7. A rough disk track profile and its power spectrum corresponding to a disk linear velocity of 17.34 m/s.



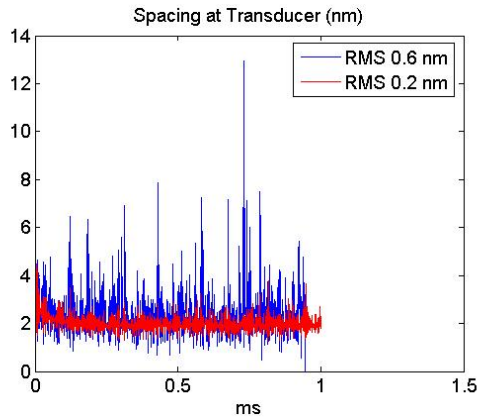
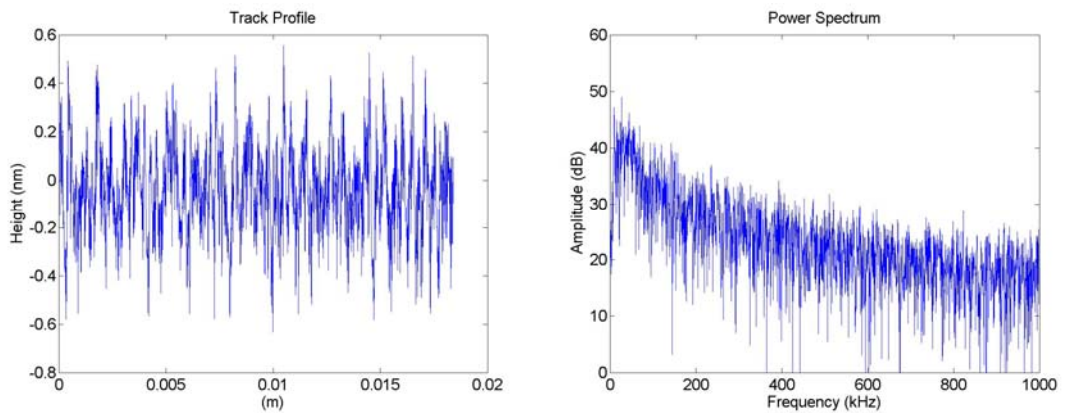
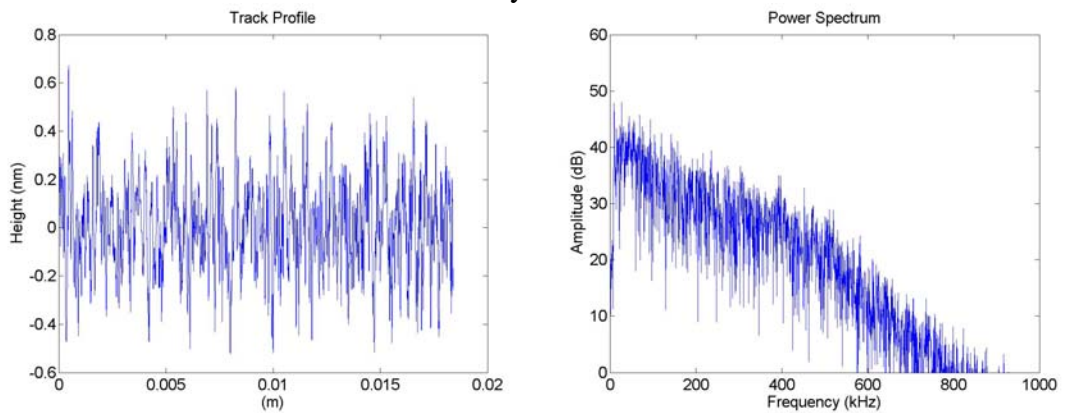


Fig.8.8. Time histories of Slider 1 with 25 mW heating power on the smooth track and the rough track.



(a) Time-domain burnished track profile and its power spectrum corresponding to a linear velocity of 17.34 m/s.



(b) Frequency-domain burnished track profile and its power spectrum corresponding to a linear velocity of 17.34 m/s.

Fig.8.9. Burnished track profiles and their power spectra corresponding to a disk linear velocity of 17.34 m/s

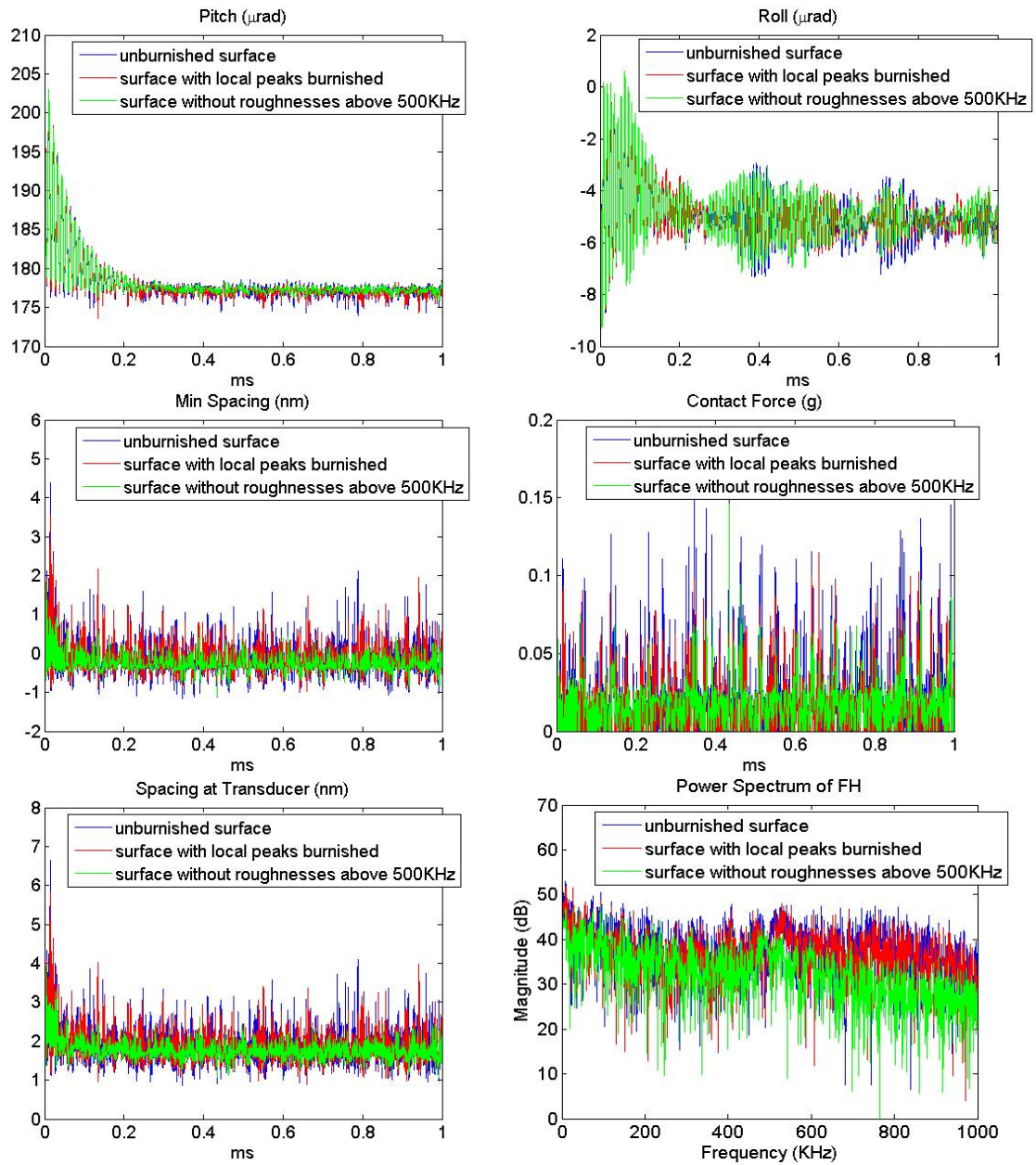
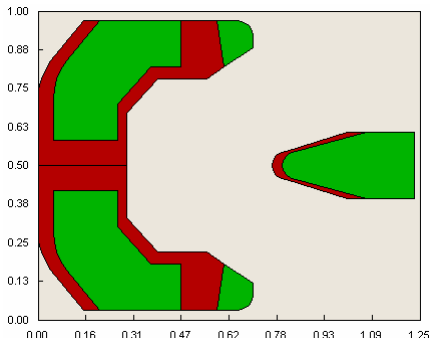
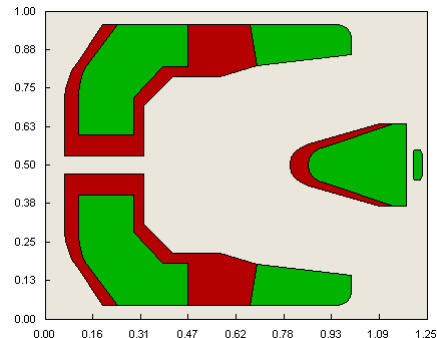


Fig.8.10. Time histories of Slider 1 on the smooth track (shown in Fig.8.2.) and burnished tracks (shown in Fig.8.9.) and the corresponding power spectra of FH.

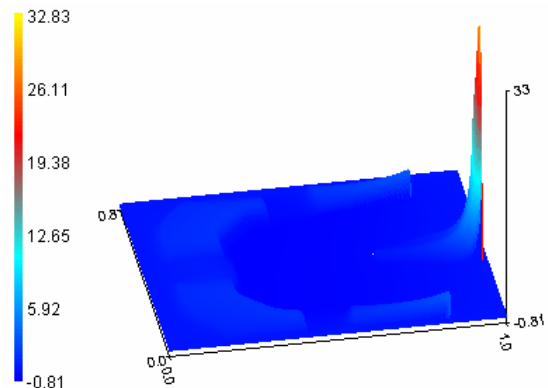


(a) Slider 2

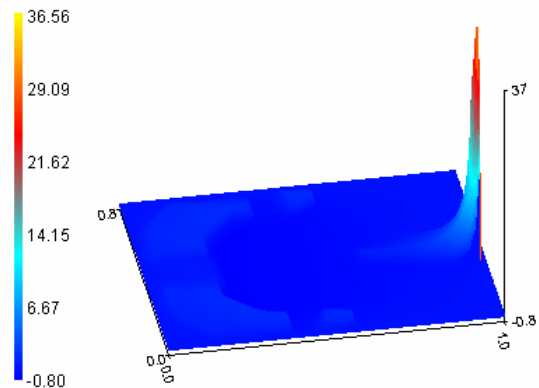


(b) Slider 3

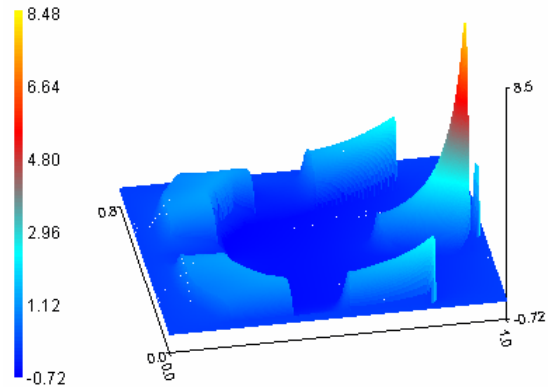
Fig.8.11. Air bearing surfaces of Slider 2 and Slider 3 (unit: mm).



(a) Slider 1



(b) Slider 2



(c) Slider 3

Fig.8.12. Air bearing pressure profiles of Slider 1, 2 and 3, respectively, at the static state with heating power off (unit: atm).

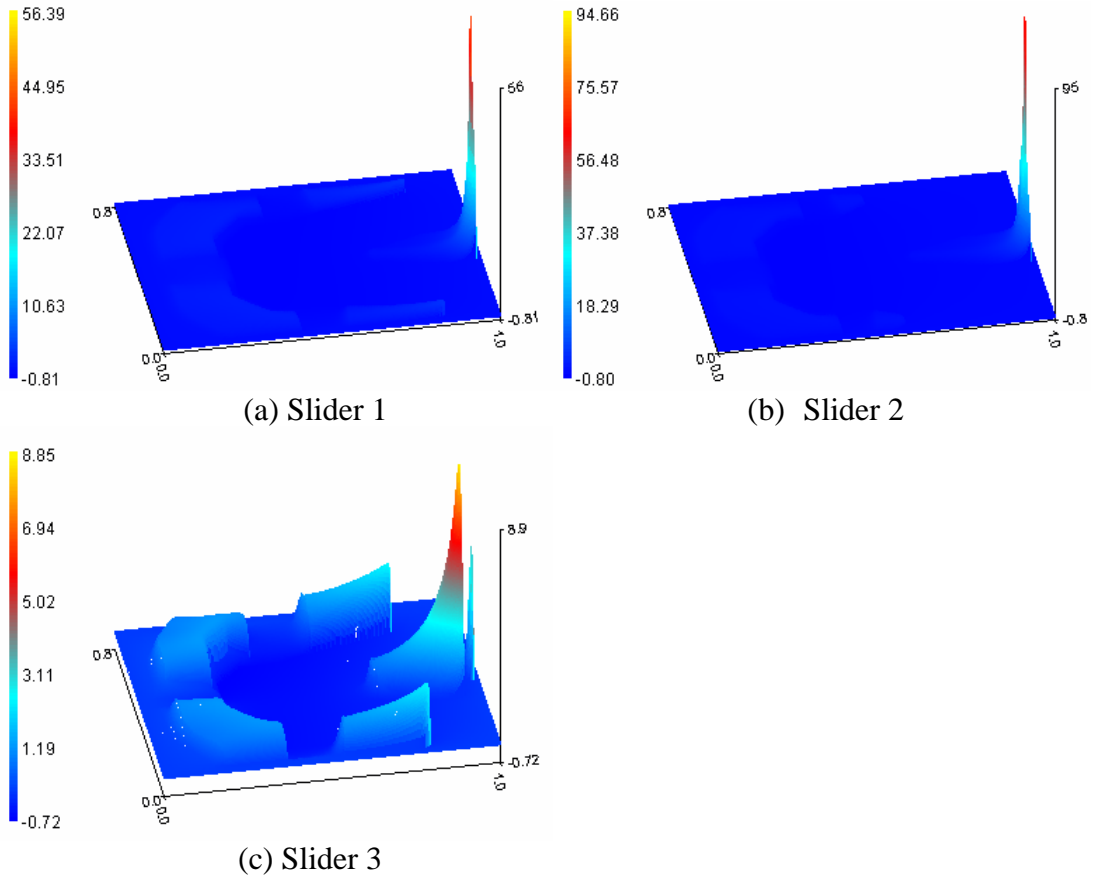


Fig.8.13. Air bearing pressure profiles of Slider 1, 2 and 3, respectively, at the static state with the touch-down heating power (unit: atm).

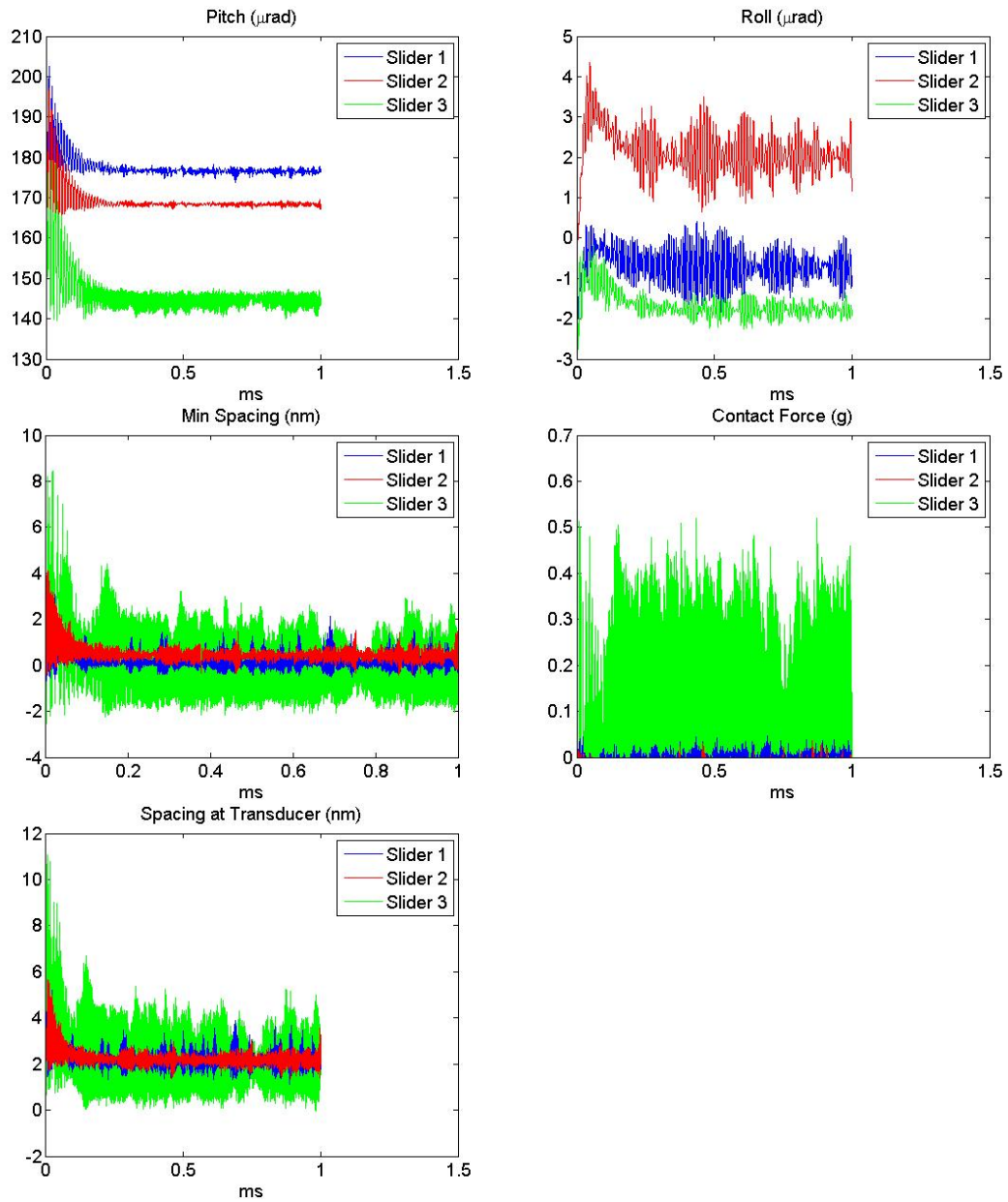


Fig.8.14. Time histories of the slider dynamics on the smooth track for Slider 1, 2 and 3.

Chapter 9 Summary and Conclusion

One of the major technological challenges for achieving an areal recording density of $1\sim 10\text{Tbit/in}^2$ in hard disk drives is to obtain a reliable and robust head disk interface with a flying height of less than 2.5 nm. This results in a transducer clearance of less than 1 nm even on a smooth disk surface with a glide height of only 1.5 nm. It is also required that the flying height variation should be less than 10% of the clearance in order to maintain a stable read/write process. With such a flow clearance, impact and contact between the slider and disk becomes unavoidable, causing a large likelihood of the slider's bouncing and the head's wearing. The bouncing and wearing will cause the instability of the head disk interface. All of these inevitable events challenge the design of the next generation of air bearing sliders.

A partial-contact head disk interface with an air bearing is proposed and analyzed in this dissertation to obtain an ultra-low clearance for $1\sim 10\text{ Tbit/in}^2$. The research focuses on the numerical simulation of the slider's performance in the partial-contact head disk interface and the feasibility of maintaining both a low bouncing amplitude and a low contact force. The effects of various important factors involved in the interface are analyzed.

Chapter 2 analyzes two types of quasi-static contact models- the asperity-based contact model and the elastic contact model based on influence coefficients. The Greenwood-Williamson model is shown to be the simplest and a sufficiently accurate asperity-based model for the slider-disk asperity contact. The disk's bulk deformation needs considering when the slider crashes onto the disk surface. In that case the elastic

contact model based on the influence coefficient is recommended. The effect of the pitch and roll angles on the contact is not negligible, so using a given contact area parallel to the disk mean surface is not an accurate approach for modeling the slider-disk contact.

Chapter 3 investigates the intermolecular adhesion between the slider and disk surfaces. A contact distance is incorporated into the widely used intermolecular adhesion force model for the slider-disk adhesion in near-contact regions. Various different asperity-based intermolecular adhesion models are chosen and compared in the modeling of the adhesion between a non-flat slider and disk surface. It is found that the classical IDMT model provides a sufficiently accurate adhesion force for the slider-disk interface. As shown by the static air bearing simulation results, the intermolecular adhesion between real slider and disk surfaces has a negligible effect on the attitude of a flying air bearing slider. When the slider touches the disk surface, the net adhesion force, i.e. the sum of the adhesion force and the contact force, does affect the partial-contact slider's attitude. As to the ultra-smooth slider and disk interfaces, the modified intermolecular adhesion force model predicts a strong adhesion.

Chapter 4 presents a nonlinear dynamics model for the partial-contact air bearing slider. The numerical simulation results using this model show that both the slider's bouncing vibration amplitude and the contact force are increased as the adhesion increases. The friction force between the slider and the disk does not affect the bouncing and contact. The disk surface roughness is the main factor in the cause of slider bouncing. Decreasing the contact pad width can significantly reduce the slider's bouncing vibration as well as the contact force. Increasing the suspension preload may suppress the slider's bouncing in a certain range without a significant increase in the contact force.

Chapter 5 focuses on the in-plane vibrations of the partial-contact slider. A

six-degree-of-freedom model of the slider's motion is implemented in the simulation of the slider's dynamics. The in-plane vibrations are found to be forced vibrations caused by the air shear and the slider-disk friction. The slider's skew angle affects the order of magnitude of the slider's off-track vibrations. For a partial-contact pico slider with a micro-trailing pad, when the contact force is less than 0.25 gf and the friction coefficient between the slider and the disk is less than 0.3, the off-track vibration peak-to-peak amplitude is on the order of 10 nm and the down-track vibration peak-to-peak amplitude is on the order of 100 nm. A reduced trailing contact pad width incurs smaller in-plane vibrations as well as a smaller bouncing vibration.

In Chapter 6, the root cause of the partial-contact slider's bouncing vibrations is obtained using three non-linear slider dynamics models. It is again found that the slider's bouncing vibration is a forced vibration caused by the moving disk waviness and roughness through the head-disk interface as the disk rotates. The friction between the slider and the disk has a negligible effect on the slider's bouncing.

In Chapter 7 we compare three different models of the heat transfer between the thermal flying control (i.e. dynamic flying height) slider and the disk. Both the pico and femto slider designs are used in the static simulation and the results indicate that the heat transfer between the slider and the disk is dominated by the heat conduction through the air bearing. The viscous heating does not affect the slider's flying attitude. The different models of the heat conduction at the air bearing surface produce a relative difference of less than 10% in the slider's flying height and pitch angle.

Chapter 8 proposes a partial-contact head disk interface with thermal protrusion for the ultra-low clearance. This interface can maintain a light contact between the protrusion tip and the disk, so that the protruded read/write transducer, close to the tip, has a stable

low flying height. The bouncing vibration amplitude and the contact force of a partial-contact slider with thermal protrusion are much smaller than those of the partial-contact micro-trailing pad slider on the same disk surface. The adhesion and friction between the slider and the disk do not affect the bouncing amplitude, while the adhesion decreases the mean flying height of the slider. The slider's bouncing vibration amplitude can be reduced to a value similar to the flying height modulation with no contact, when the disk track is burnished or the air bearing pressure peak is sufficiently localized at the trailing edge center. A modified air bearing surface with a higher air bearing pressure at the transducer weakens the contact force between the protrusion tip and the disk and suppresses the bouncing vibration amplitude.

In conclusion, the results presented in this dissertation appear to indicate that with proper designs of the slider's air bearing surface and the disk's roughness pattern it will be possible to achieve a sufficiently stable heat disk interface for the areal density goals of the next generation of hard disk drives.